Nanostructure of calcareous biominerals and osteopontin

Dimitra Athanasiadou

Faculty of Dentistry

McGill University

Montreal, Quebec, Canada

December 2018

A thesis submitted to McGill University in partial fulfillment of the requirements of the degree of Doctor of Philosophy in Craniofacial Health Sciences

I would like to dedicate my thesis to my beloved parents and sister.

TABLE OF CONTENTS

List of figures

List of movies

Movie 2.S1 Three-dimensional reconstruction from a tilt series of the upper palisade layer of avian chicken eggshell *G. gallus domesticus*.

https://mcgill-my.sharepoint.com/:v:/g/personal/dimitra_athanasiadou_mail_mcgill_ca/EfiVoa0YTP1Ir0tYOfjR_7wBZrsrDbve4qVEVRf8pR_Gig

Movie 2.S2 Three-dimensional reconstruction of nanodomains found in the upper palisade layer of the eggshell.

https://mcgill-my.sharepoint.com/:v:/g/personal/dimitra_athanasiadou_mail_mcgill_ca/ESl_qe6FT2VLjRQ690nZEg0ByYSS01i08_uqB6Pf2MdpPA

Movie 2.S3 Three-dimensional reconstruction from a tilt series of the synthetic calcite crystal grown with 5.9 μM osteopontin.

https://mcgill-my.sharepoint.com/:v:/g/personal/dimitra_athanasiadou_mail_mcgill_ca/EVK-p9ZgPGdNuNvyyPejlbMBi-we6UIgJMj84cW0oXkRrQ

Movie 2.S4 Three-dimensional reconstruction of a nanostructured region found in the synthetic calcite crystal grown with 5.9 μM osteopontin.

https://mcgill-my.sharepoint.com/:v:/g/personal/dimitra_athanasiadou_mail_mcgill_ca/EfGZqJp3sN1Np3q_PceoNCYBd09QN2dQudEqpZa9AnKx-A

Movie 3.S1 Three-dimensional reconstruction of utricular otoconia (otoconia in grey and bone in orange) from an X-ray computed tomography series.

https://mcgill-my.sharepoint.com/:v:/g/personal/dimitra_athanasiadou_mail_mcgill_ca/EVoKjSjMx6NAt2lX8Nmc13UB5x5m4IAzokbjp1QHG27bVg

Movie 3.S2 Three-dimensional reconstruction from the branch region of 8-day-old mouse utricular otoconia from a TEM tomography tilt series.

https://mcgill-my.sharepoint.com/:v:/g/personal/dimitra_athanasiadou_mail_mcgill_ca/EYqncTYElUxKnzDmTAm82KEB042O6pjPmkYP07aHwZBlXg

Movie 3.S3 Three-dimensional reconstruction of a nanostructured region found in the branch region of 8-day-old mouse utricular otoconia from a TEM tomography tilt series.

https://mcgill-my.sharepoint.com/:v:/g/personal/dimitra_athanasiadou_mail_mcgill_ca/EacaFB6mVNFJp6p3iOa_XTABL0GnYgT5utxJ5oyCEHnbbQ

List of abbreviations

AAAS	American Association for the Advancement of Science
ACC	Amorphous calcium carbonate
ACP	Amorphous calcium phosphate
AFM	Atomic force microscopy
ASARM	Acidic, serine- and aspartic acid-rich motif
Asp/D	Aspartic amino acid
BPPV	Benign paroxysmal positional vertigo
BSA	Bovine serum albumin
CIHR	Canadian Institutes of Health Research
CLS	Canadian Light Source
CNS	Central nervous system
CSB	Calcium reserve body
DMP1	Dentin matrix protein 1
EBSD	Electron backscatter diffraction
EM	Electron microscopy
FEMR	Facility for Electron Microscopy Research
FIB	Focused ion beam
Glu/E	Glutamic amino acid
HRTEM	High-resolution transmission electron microscopy
KSPGs	Keratan sulfate proteoglycans
ML	Mammillary layer or mammillae

MMP	Matrix metalloproteinase
NSERC	Natural Sciences and Engineering Research Council of Canada
OC-17	Ovocleidin-17
OC-116	Ovocleidin-116
Oc90	Otoconin 90
OCX-32	Ovocalyxin-32
OCX-36	Ovocalyxin-36
OPN	Osteopontin
Opn$^{-/-}$	*Opn*-null mice
PHEX	Phosphate-regulating gene with Homologies to Endopeptidase on the X chromosome
PL	Palisade layer or palisades
PNCs	Prenucleation clusters
PVDF	Polyvinylidene difluoride
RGD	Arginine-glycine-aspartic acid motif
SAED	Selected-area electron diffraction patterns
Sc1	Sparc-like protein 1
SD	Standard deviation
SDS	Sodium dodecyl sulphate
SDS-PAGE	SDS-polyacrylamide gel electrophoresis
SEM	Scanning electron microscopy
SIBLING	Small, Integrin-Binding LIgand N-linked Glycoprotein
Sparc	Secreted protein acidic and rich in cysteine

SXRMB	Soft X-ray Microcharacterization Beamline
TBS-T	Tris-buffered saline/Tween 20
TG2	Tissue transglutaminase 2
VCL	Vertical crystal layer
XAS	X-ray absorption spectroscopy
2D XRD	2-dimensional X-ray diffraction

Abstract

Avian eggshell and mammalian otoconia have complex structures that are hierarchically organized from nanometer to micrometer length scales. Biomineralization of calcium carbonate (calcite) nanostructure in eggshell and otoconia involves the interaction and occlusion of organic protein matrix within the mineral. One of the proteins associated with these processes during biomineralization (including in bones and teeth) is osteopontin (OPN), a secreted highly disordered glycoprotein belonging to the SIBLING (**S**mall, **I**ntegrin-**B**inding **LI**gand **N**-linked **G**lycoprotein) family of proteins. OPN is a highly acidic (negatively charged) protein containing abundant glutamic and aspartic amino acids, and phosphorylated serines, enabling OPN to bind strongly to calcium atoms of calcite crystals. Furthermore, it is well-known that the functional and mechanical properties of biominerals are strongly influenced by the hierarchical structural organization of the biomineral. The goal of this dissertation research was to investigate the structure of chicken eggshell (*Gallus gallus domesticus*) and mouse otoconia at the nanoscale.

In the eggshell, we identified a mineral nanostructure throughout the major eggshell layers that varied in size, presumably arising from the occlusion of organic matrix. OPN – an eggshell-resident inhibitory biomacromolecule – could also be incorporated within synthetic calcite crystals to create a similar nanostructure as that observed in eggshell, with higher OPN concentration leading to a smaller nanostructure size. Mechanical (hardness and elastic modulus) and functional (dissolution) properties were associated with the observed nanostructure. Decreased nanostructure was associated with increased eggshell hardness and elastic modulus, whereas in fertilized incubated eggs, fractional nanostructure dissolution appeared critical for providing calcium to the growing skeleton of the chick embryo.

Similar to chicken eggshell, a structural analysis of otoconia in C57BL/6 mice showed an external and internal calcitic nanostructure. OPN was detected at the surface of otoconia and there correlated with surface nanostructure. Other occluded proteins, possibly including OPN, likely participate in producing the internal nanostructure.

In conclusion, these findings provide details on the nanostructure and composition of chicken eggshell and mammalian otoconia, suggesting also another possible role for OPN in biomineralization processes, which in turn might guide nanocomposite materials development.

Résumé

La coquille de l'œuf aviaire et l'otoconie de mammifère sont constituées de structures complexes organisées hiérarchiquement à partir d'une échelle allant de longueur nanométrique à des longueurs micrométriques. La biominéralisation des structures nanocristallines de carbonate de calcium (calcite) dans la coquille de l'œuf et dans l'otoconie est le résultat de processus complexes d'interaction et d'occlusion de la matrice protéique organique dans le minéral. Durant cette période de biominéralisation, l'ostéopontine (OPN), une glycoprotéine de structure considérablement désordonnée faisant partie des protéines SIBLING (**S**mall, **I**ntegrin-**B**inding **LI**gand **N**-linked **G**lycoprotein) joue un rôle essentiel. L'OPN possède un caractère très acide (protéine chargée négativement) puisqu'elle contient des acides aminés glutamiques et aspartiques en abondance ainsi que des sérines phosphorylées. Ceci permet à l'OPN de se lier activement aux atomes de calcium parvenant des cristaux de calcite. De plus, les propriétés mécaniques et fonctionnelles des biominéraux sont grandement influencées par leur organisation hiérarchique structurale. À cet effet, l'objectif de ce travail de recherche est d'examiner la structure et la composition de la coquille de l'œuf de poule ainsi que celles de l'otoconie de souris à l'échelle nanoscopique afin de mieux comprendre son fonctionnement.

Dans la coquille de l'œuf, nous avons trouvé, dans les couches (strates) principales, une nanostructure minérale de taille variable provenant vraisemblablement de processus d'occlusion de la matrice organique. Une biomacromolécule résidante de la coquille avec une propriété inhibitoire de croissance minérale, l'OPN peut aussi être incorporée à l'intérieur des cristaux de calcite synthétiques, créant de nanostructures similaires à celles observées dans la coquille de l'œuf. Ainsi, une haute teneur en OPN mènera à une nanostructure avec des cristallites de plus petite taille. Les propriétés mécaniques (la dureté et le module de Young) et fonctionnelles (la

dissolution) des cristaux calciques synthétiques qui incorporent l'OPN sont en corrélation avec la nanostructure observée. Les nanostructures ayant des cristallites plus petites possèdent une dureté et un module de Young plus élevés, alors que la dissolution fractionnaire de la nanostructure des œufs fertilisés incubés semble essentielle à l'approvisionnement du squelette de l'embryon de la poule en croissance avec du calcium.

Semblable aux résultats obtenus pour la coquille d'œuf, l'analyse structurale des otoconies des souris C57BL/6 a démontré que l'otoconie est composée de nanocristaux de calcite autant à l'extérieur qu'à l'intérieur. D'autres protéines occluses, incluant éventuellement l'OPN, participent vraisemblablement au développement de la nanostructure interne.

En conclusion, ces résultats fournissent des détails sur la nanostructure et la composition de la coquille d'œuf d'une poule et celle de l'otoconie de mammifère, suggérant un autre rôle pour l'OPN dans les processus de biominéralisation qui pourrait éventuellement contribuer au développement de biomatériaux nanocomposites.

Acknowledgements

First and foremost, I would like to express my sincere gratitude to my supervisor Dr. Marc D. McKee for his continuous and invaluable guidance and support throughout my doctoral training. I am forever grateful for giving me the opportunity to continue my postgraduate studies in his scientific group, for his encouragement and the advice he provided me over these past years.

I would like to thank all the past and current members of the McKee lab: Ms. Lydia Malynowsky, Ms. Aisha Mousa, Dr. Betty Hoac and Dr. Valentin Nelea for their help and insightful discussions in and out of the laboratory, and Dr. Wenge Jiang for his contributions to the work. I would also like to thank all past and current staff at the Facility for Electron Microscopy Research (FEMR), Ms. Line Mongeon, Dr. S. Kelly Sears, Dr. Kaustuv Basu, Dr. David Liu, Dr. Ken Wu and Ms. Weawkamol Leelapornpisit, for their technical and teaching support. Thank you also to the staff of the Soft X-ray Microcharacterization Beamline (SXRMB) 06B1-1, Dr. Yongfeng Hu, Dr. Qunfeng Xiao and Ms. Aimee MacLennan at Canadian Light Source (CLS) for their technical support.

I wish to thank the members of my supervisory committee: Dr. Marta Cerruti, Dr. Jake E. Barralet and Dr. Francois Barthelat, for their insightful comments and reinforcement of my research. Furthermore, I want to thank the Canadian Institutes of Health Research (CIHR) and the Natural Sciences and Engineering Research Council of Canada (NSERC) for the financial support of this research and the Canadian Light Source (CLS) for financial travel support. Moreover, I would like to thank all the collaborators and their lab members with whom I had the privilege to work with during my doctoral training. I am also thankful to Dr. Jeanne Paquette for all the intuitive scientific discussions and Dr. Athanasios Godelitsas for his advice and moral support

throughout this journey. A special thanks to Dr. Valentin Nelea and Miss Rand Addasi for their help with the French translation of the abstract.

Finally, I would like to express my deepest gratitude to my parents, Mr. Savvas Athanasiadis and Mrs. Angeliki Kourmentza, along with my sister, Dr. Ioanna Athanasiadou for their unconditional love, sacrifices, continuous support and encouragement throughout these years. Thank you for always being there for me and for everything you have done.

Preface

In Nature, biological organisms generate mineralized tissues such as bones, teeth and shells for multiple functional purposes. Biomineralization is an interdisciplinary scientific field referring to the processes by which organisms produce minerals (biominerals). The study of these inorganic-organic hybrid materials has received much attention in recent years in order to advance our understanding of their biomineralization processes, and to advance the development of biomimetic materials and possibly new therapeutic treatments for human diseases and tissue repair. Therefore, greater insights for all of this should be gained through studies on structure and self-organization at the nanometer length scale, and through examining molecular interactions between the inorganic mineral and organic matrix molecules.

This dissertation presents the research conducted during my doctoral studies in the field of Biomineralization. It includes two manuscripts of original research data focusing on avian eggshell and mammalian otoconia, one published in a peer-reviewed journal and the other one is in preparation for submission. Moreover, during my doctoral training, I have co-authored three other papers in the same field either published, in review or in preparation. The aim of this dissertation is to improve our knowledge on the structure of the domestic chicken eggshell *G. gallus domesticus* and mouse otoconia at the nanoscale, and to understand how OPN interacts with calcite, all of which should lead to a better understanding of the calcium carbonate biomineralization processes.

Contribution to original knowledge

The aim of this dissertation is to improve our knowledge on the structure of two calcitic biomineralized assemblies − the domestic chicken eggshell (*G. gallus domesticus*) and mouse otoconia. Using advanced sample-preparation and analytical methods to examine ultrastructure in hierarchically organized, hard mineralized assemblies, we have investigated down to the nanoscale the detailed structure of eggshell and otoconia. We have also studied how a mineral-binding protein called osteopontin (OPN) occludes into calcite to affect the growth and assembly of this inorganic mineral phase. The findings from these investigations have led to a better understanding of calcium carbonate biomineralization processes. The list below summarizes the novel findings presented in this dissertation.

- The eggshell of the domestic chicken (*G. gallus domesticus*) has a subunit nanostructure throughout its thickness, varying in size depending upon its location within the shell.
- The smallest nanostructure is observed in the outermost eggshell layers – the Vertical Crystal Layer (VCL) and the upper Palisade Layer (PL), being ~30 nm in Feret diameter. Within the upper PL region, an even smaller nanostructure subunit structure was observed (5-7 nm in diameter).
- In these eggshell layers with the smallest subunit structure, the highest hardness and elastic modulus values were observed, correlating with the highest OPN content.
- Variations in OPN concentration were demonstrated across the eggshell thickness, generally decreasing towards the shell interior.

- OPN occluded into synthetic calcite crystals and induced a nanostructure similar to that observed in chicken eggshell, with higher OPN concentrations generating smaller nanostructure.
- The nanostructure dimensions of the innermost eggshell layer, the Mammillary Layer (ML), decreased substantially in fertilized incubated eggs having undergone dissolution for chick embryo skeletal growth.
- Mouse otoconia have an internal nanostructure size of approximately 50 nm in Feret diameter as measured from AFM images, and nanodomains having even smaller dimensions of ~10 nm as observed by TEM.
- OPN was identified at the surface of the otoconia which could be associated with the external nanogranular texture of otoconia.

Contribution of authors

This doctoral dissertation consists of two research manuscripts prepared by the candidate as first author. The contributions of the candidate and all the co-authors for each manuscript are summarized below.

Chapter 2

Title: Nanostructure, osteopontin, and mechanical properties of calcitic avian eggshell

Published in Science Advances (2018) 4(3):eaar3219

Authors: Dimitra Athanasiadou, Wenge Jiang, Dina Goldbaum, Aroba Saleem, Kaustuv Basu, Michael S. Pacella, Corinna F. Böhm, Richard R. Chromik, Maxwell T. Hincke, Alejandro B. Rodríguez-Navarro, Hojatollah Vali, Stephan E. Wolf, Jeffrey J. Gray, Khanh Huy Bui, Marc D. McKee

Contributions: D. Athanasiadou participated in the study design, performed the in vitro experiments, Raman spectroscopy and the Western blot analysis, prepared the samples for FIB sectioning, EM imaging and nanoindentation analysis, performed SEM and TEM imaging, performed the nanostructure measurements and the statistical analysis, analysed and interpreted the results, and prepared the manuscript. **W. Jiang** participated in the study design, performed the AFM analysis, participated in the interpretation of results and reviewed the final manuscript. **D. Goldbaum** performed the nanoindentation experiments on chicken eggshell, participated in the interpretation and analysis of nanoindentation data, and reviewed the final manuscript. **A. Saleem** performed the nanoindentation experiments on synthetic calcite crystals, participated in the

interpretation and analysis of data, and reviewed the final manuscript. **K. Basu** performed the TEM/tomography and reviewed the final manuscript. **M. S. Pacella** and **Jeffrey J. Gray** performed the computational simulations and reviewed the final manuscript. **C. F. Böhm** prepared the polished chicken eggshell wedge and reviewed the final manuscript. **R. R. Chromik** interpreted and analysed the nanoindentation data and reviewed the final manuscript. **M. T. Hincke** participated in the biochemical analysis for OPN, in the analysis and interpretation of data and reviewed the final manuscript. **A. B. Rodríguez-Navarro** participated in the EBSD and 2D XRD analysis, contributed to the analysis and interpretation of data and reviewed the final manuscript. **H. Vali** participated in the analysis and interpretation of TEM and electron tomography data and reviewed the final manuscript. **S. E. Wolf** participated in the analysis and interpretation of data and reviewed the final manuscript. **K. H. Bui** participated in the TEM/tomography and reviewed the final manuscript. **M. D. McKee** participated in the study design, provided the OPN immunogold labeled section, participated in the interpretation and analysis of the data, participated in the manuscript preparation, and reviewed the final manuscript.

Chapter 3

Title: Nanostructure of mammalian otoconia

Manuscript in preparation

Authors: **Dimitra Athanasiadou**, Wenge Jiang, Natalie Reznikov, Alejandro B. Rodríguez-Navarro, Valentin Nelea, Yongfeng Hu, Marc D. McKee

Contributions: D. Athanasiadou participated in the study design, performed the in vitro experiments, Raman and XAS spectroscopy, prepared the samples for FIB sectioning, performed SEM and TEM imaging, performed the nanostructure measurements and the statistical analysis, analysed and interpreted the results, and prepared the manuscript. **W. Jiang** performed the AFM analysis. **N. Reznikov** participated in the acquisition and analysis of the X-ray computed tomography 3D imaging data. **A. B. Rodríguez-Navarro** participated in the 2D XRD analysis, contributed to the data analysis and interpretation. **V. Nelea** performed the XRD experiments. **Y. Hu** participated in the analysis and interpretation of XAS data. **M. D. McKee** participated in the study design, in the interpretation and analysis of the data, and in the manuscript preparation.

In addition to the manuscripts included in this dissertation, during my doctoral training, I have also co-authored the following publications:

1. Wenge Jiang, Michael S. Pacella, **Dimitra Athanasiadou**, Valentin Nelea, Hojatollah Vali, Robert M. Hazen, Jeffrey J. Gray & Marc D. McKee, Chiral acidic amino acids induce chiral hierarchical structure in calcium carbonate. *Nature Communications* 13(8):15066

2. Wenge Jiang, **Dimitra Athanasiadou**, Shaodong Zhang, Valentin Nelea, Marc D. McKee, Homochirality in biomineral suprastructures induced by assembly of single-enantiomer amino acids from a nonracemic mixture. (in revision in *Nature Communications*)

3. Alejandro B. Rodríguez-Navarro, Nazaret Dominguez-Gasca, **Dimitra Athanasiadou**, Nathalie Le Roy, Alicia González-Segura, Maxwell T. Hincke, Marc D. McKee, Yves Nys, Joel Gautron, Intracrystalline organic matter controls Guinea fowl eggshell structural organization from the micro to the atomic scale. (in preparation for submission)

Introduction

Living organisms produce a wide variety of biominerals through biomineralization processes typically regulated by secreted proteins. Biominerals form complex, hierarchically organized mineralized structures with unique mechanical properties. Therefore, understanding the factors that orchestrate their formation is important to gaining new insights into not only biomineralization processes themselves, but also into rational fabrication of novel bio-inspired synthetic materials. Among calcareous biominerals, avian eggshell and otoconia have attracted the interest of the scientists because of their remarkable properties and function; however, additional investigation needs to be performed to understand their structure and function. The main inorganic phase of these biominerals is calcite ($CaCO_3$), one of the most abundant biominerals in Nature. A protein often associated with biomineralization in many organisms and in different mineralized structures is called osteopontin (OPN), the name reflecting its initial discovery in bone. OPN is a highly acidic and phosphorylated mineral-binding glycoprotein found in many tissues including vertebrate bones and teeth, avian eggshell and mammalian otoconia, as well as in biological fluids and in pathological conditions where it serves multifunctional roles. Here, I present my findings on two calcitic biomineralizing systems, and the effect of OPN on calcitic biomineralization.

Rationale and objectives

Chapter 2: Nanostructure, osteopontin, and mechanical properties of calcitic avian eggshell

Hypothesis: Avian eggshell has a variable nanostructure across its thickness whose dimensions are influenced by the concentration of the mineral-binding protein OPN, whose actions lead to enhanced mechanical properties of the shell.

Rationale: In recent years, there has been extensive structural characterization of biominerals identifying nanogranular features (*1*). This nanogranularity denotes a nonclassical crystallization pathway and is commonly associated with advanced functional and mechanical properties of biominerals (*2, 3*). This study aims to explore chicken eggshell structure at the nanoscale throughout its layers, and to correlate this with the mechanical and functional properties of eggshell. Additionally, we aimed to describe the role of OPN, a well-characterized inhibitor protein of mineralization found in chicken eggshell, on inducing eggshell nanostructure.

Chapter 3: Nanostructure of mammalian otoconia

Hypothesis: Mammalian otoconia, the only calcium carbonate (calcite) biomineral existing in humans under normal physiologic conditions, possesses a nanostructure similar to other calcitic biominerals found in Nature.

Rationale: Based on our findings for chicken eggshell, we posited that a similar nanoscale structure might exist in another calcitic biomineral, the mammalian (in this case mouse) otoconia, where these structures of the inner ear are responsible for maintaining balance and for detecting linear acceleration. The aim of this study was to describe in detail the nanostructure observed in mouse otoconia as well as the localization of OPN (*4*). This work characterizes the nanostructure

of mouse otoconia using advanced 3D imaging techniques that could enhance our knowledge on otoconial degeneration leading to benign paroxysmal positional vertigo (BPPV), the main cause of vertigo in humans.

Chapter 1 - Literature review

Biominerals are hybrid materials composed of an inorganic phase (mineral) and an organic phase (mainly proteins). Until now, more than 60 different types of biominerals have been identified in Nature. Many biological organisms have developed remarkable strategies for guiding the growth of the inorganic components of their mineralized tissues to serve a diversity of functions based on their structure and mechanical properties. This has resulted in complex hierarchical mineralized structures constructed under ambient conditions having diverse shapes and sizes. These sophisticated structures built by different living organisms play significant functional roles where they have advanced mechanical properties compared to their brittle geological counterparts.

Common biominerals are calcium carbonates in invertebrates and vertebrates, calcium phosphates in vertebrates, and silicates in diatoms and algae found in an amorphous and/or crystalline state. Calcium-containing minerals predominate probably due to the widespread use of abundant available of calcium ions by the organisms since the beginning of the evolution of life. Avian eggshells and mammalian otoconia of the inner ear are calcium carbonate biominerals. These biominerals have important roles including for such diverse functions as protection, support and balance. Unraveling the factors that control their structure is essential for understanding their formation processes and functions, and at the same time allows us to mimic such features to develop new synthetic materials with similar advanced properties.

1.1 Calcium carbonate biominerals

Calcium carbonate ($CaCO_3$) is one of the most abundant biominerals in Nature, and is used extensively by Industry (e.g. filler, pigment, paper and scale formation) (*5, 6*). Terrestrial and marine organisms including seashells, snail shells and eggshells, use $CaCO_3$ polymorphs in the presence of an abundant organic matrix for building their functionalized biomineralized structures with unique mechanical properties (*5, 7*). These characteristics facilitate biomineral formation to offer structural support and protection (*5*), display photonic structures (*8*), and functions in maintaining balance (*9*), and serve as ion reservoirs (*10*), as well as optical and sensing tools for orientation purposes (*11, 12*).

Calcium carbonate exist as three anhydrous polymorphs with typical morphologies: calcite (rhombohedral), aragonite (needle-like) and vaterite (spherical), in two hydrated crystalline forms: a monohydrate (monohydrocalcite – $CaCO_3 \cdot H_2O$) and a hexahydrate (ikaite – $CaCO_3 \cdot 6H_2O$) $CaCO_3$ phase, and several amorphous phases (ACC) having different short range order and different degrees of hydration (*13-16*). Monohydrocalcite can be detected in shark otoconia whereas for hexahydrate, there is no evidence relating this mineral phase to biomineralization (*5, 17*).

At ambient conditions, calcite is the most thermodynamically stable $CaCO_3$ polymorph and the least water-soluble in contrast to vaterite, which is the least stable $CaCO_3$ polymorph with the highest water solubility (*5, 18*). At ambient temperature and pressure, aragonite is slightly more unstable than calcite (*5*). Nevertheless, aragonite is the only preserved $CaCO_3$ polymorph precipitated from supersaturated aqueous solutions including magnesium ions at a molar Mg:Ca ratio higher than 4 which is comparable with seawater composition while vaterite can also precipitate from highly supersaturated solutions (*13*). Aragonite and calcite are possible to be

transformed from vaterite at 0-30°C and 60-80°C, respectively (*19, 20*). Additionally, in Nature, transformation of aragonite to calcite is likely to occur in temperatures higher than 380°C (*21*). Vaterite, as a metastable $CaCO_3$ phase, is possible to appear as a transient intermediate between ACC and the most stable $CaCO_3$ phases, calcite or aragonite (*22*).

Calcite is crystallized in the trigonal crystallographic system with unit cell dimensions a = b = 4.990 Å, angles α = β = 90°, γ = 120° and space group R-3c (*23*). Aragonite belongs to the orthorhombic crystallographic system with a = 4.9598 Å, b = 7.9641 Å, and c = 5.7379 Å and α = β = γ = 90° (*24*) and space group Pmcn (*13, 23*). Experimental evidence and isoenergetic methods have indicated that different structures with hexagonal, monoclinic and triclinic symmetries coexist in vaterite crystals (*25-27*). Calcite and aragonite share alike structures having their inter-planar carbonate ions organized in a tottered array related to each other (*18*). In calcite, each calcium ion is placed in an octahedral coordination environment of six carbonate ions whereas in aragonite, calcium ion has a ninefold coordination (*13, 28*) (Fig. 1.1).

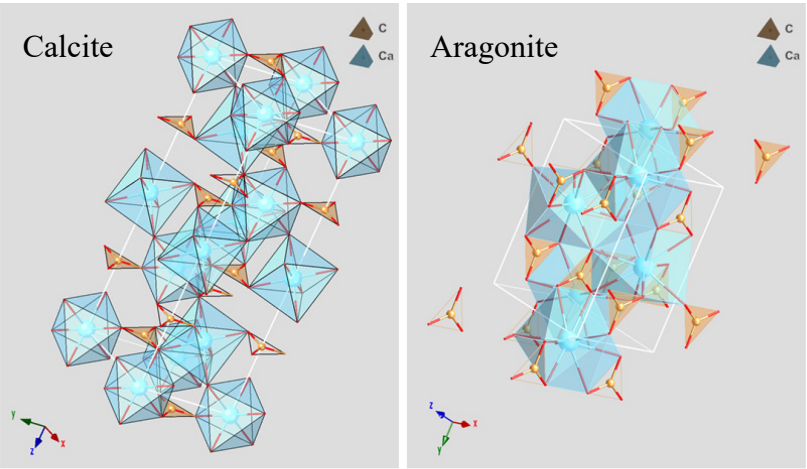

Fig. 1.1 Crystal structure of calcite and aragonite (created by CrystalMaker 10.1 software). The crystal structure of calcite is trigonal, with space group R-3c. In calcite, calcium (light blue) has a six-fold coordination by oxygen, whereas in aragonite calcium has a nine-fold coordination by oxygen.

Organisms induce $CaCO_3$ precipitation, having complete control over polymorph selection, with calcite and aragonite being the most common biologically induced $CaCO_3$ polymorphs in numerous organisms compared to metastable vaterite (*5*). Vaterite has been observed as a constituent in turtle eggshells (*29*), otoliths of Coho salmon fish (*30*), freshwater lackluster pearls (*31*) and as repair tissue in mollusk shells after injury (*32*). In addition, ascidian *Herdmania momus* is an example of an organism where vaterite occurs as the only mineral phase in its endoskeleton (*33*).

Biominerals are generally composed only of one mineral polymorph, but in some cases two or even three polymorphs are found in a single shell, distinctly separated within compartments (*5, 34*). For example, in *Pterioida* bivalves, the nacre develops on an outer assembled arrangement of prismatic calcite crystals aligned perpendicular to the surface of the shell, while the gastropod *Haliotis tuberculata* possesses a three-layered structure, this being a prismatic calcitic layer between two aragonitic layers (*35, 36*). In vitro experiments on calcium carbonate crystal growth in the presence of extracted acidic proteins – rich in glutamic and/or aspartic amino acids – from either calcitic or aragonitic layers are responsible for polymorph selectivity (*37, 38*). In addition, the interaction with macromolecules controls the shape and texture of these crystals whereas ACC, which is extremely unstable under ambient conditions and rapidly is transformed to a crystalline phase, can be stabilized in the presence of acidic proteins (*38-40*). In the case of biogenic calcite, C – O bonds are elongated up to 0.7%, demonstrating calcite modification by the attachment of organic macromolecules with negatively charged residues to calcium sites of the crystal (*41*). Elevated mechanical properties of biominerals are attributed also to the organic occlusion into the mineral (*42-44*). Experimental observations on occlusion of different substances at the level of

intracrystalline proteins have led to the synthesis of crystals with mechanical properties similar to natural biominerals (*45, 46*).

1.2 Crystallization pathways in biomineralization

Biominerals provide a vital source of inspiration for materials design and synthesis with superior properties (*47*). These advanced properties are usually the result of a complex hierarchical structural organization from the nano- to macro- length scale in relation to the organic composite. Therefore, understanding the crystallization and self-organization mechanisms of biominerals has a huge impact on various research fields. Namely, this has occurred for the development of new ceramics for bone replacement (*48*) and treatments for pathological biomineralization (e.g. vascular calcification and nephrolithiasis) (*49*), collectively having a major influence in medical and clinical research. Moreover, in geology and climate sciences, calcifying species abundance and distribution have essential implications for explaining environmental phenomena from earlier years. Fossils function as climate records giving evidence for paleoclimatology events and thus, information for the evolution of climate on Earth (*50, 51*).

In recent years, advances in high-resolution imaging methods, such as atomic force microscopy and transmission electron microscopy, have been used to show that many biominerals of different taxa and phyla consist of nanosized, space-filled crystalline 50-100 nm diameter building blocks, separated by intergranular organics (*1, 2, 52-57*). This nanogranular structure behaves surprisingly as a single crystal and together with all the other levels of hierarchical organization contributes to the mechanical properties of any given biomineral (*58*). Examples include the sea urchin shell and the spines of the *Echinometridae* family (*40, 59*), the calcitic

prisms in the *Pinna nobilis* bivalve (*57*), the nacre of the *Pinctada fucata* pearl oyster *(60)* and the red coral *Corallium rubrum* skeleton *(61, 62).*

Organics in biominerals have been observed to be present as a halo around individual nanogranules (*63, 64*). It is worth mentioning that calcareous biominerals are not the only biominerals acquiring nanogranularity. For instance, hexactinellid sponge genus *Euplectella* and demosponges like *Thethya aurantia* are built by tightly fused silica nanogranules coated by an organic matrix (*65-67*). Fossils have also been discovered to preserve a nanogranular structure (*56, 68*). However, despite the huge number of nanostructured biominerals, there are also examples, such as coccoliths (e.g. *Coccolithus pelagilus*), that do not exhibit nanogranular features (*69, 70*). Materials that diffract as single crystals and at the same time exhibit a nanogranular structure are often called mesocrystals due to their mesoscopic structure (*71-73*). However, mesocrystallinity does not characterize all the biominerals with a nanogranular structure. Several examples of a low crystallographic arrangement (*1*) and complex crystallographic textures of crystalline domains such as tilting along crystal axes have been reported (*63, 74*).

Experimental evidence reveals that biominerals, as well as their biomimetic counterparts, frequently demonstrate a nanostructure formed via amorphous precursor phases showing that they do not follow a classical crystallization pathway (*3, 75*). According to classical crystallization theory, crystallization originates with the clustering of monomers (ions or molecules) leading to the nucleation of a critical cluster size which continues to grow via monomer-by-monomer addition at the kink sites (*3, 76*). These ionic interactions into the crystal lattice determine a final crystal morphology having essentially smooth stable crystal faces at the atomic level (*69*), which is often not what is seen in biomineralized structures. Therefore, there is evidence for a nonclassical crystallization process forming biominerals (*73, 75, 77*).

The nonclassical crystallization process occurs via an aggregation-growth method with liquid or solid, amorphous or crystalline precursor nanoparticles being the main building blocks – in contrast to the monomers (ions and/or molecules) of the classical crystallization theory – presenting a nanogranular texture (*3, 75*). Nonclassical nucleation involves initial ACC nucleation by the formation of stable prenucleation clusters (PNCs) giving rise to liquid or solid ACC precursors mainly after aggregation (*3, 78*). Most of the calcium carbonate biominerals are formed via ACC precursors (*16, 79, 80*), while in vertebrate bone and tooth, carbonated hydroxyapatite and anhydrous guanine crystals in fish skin form via amorphous calcium phosphate (ACP) and amorphous guanine, respectively (*81-84*). However, a combination of solution-mediated ion-by-ion and a particle-mediated process can be involved during crystal growth in biological systems (*69*). The presence of water determines the balance between these two processes since it is the driving force of transformation from an amorphous to a crystalline phase (*85*). When there is a decreased water activity, nanosphere dissolution is reduced with nanospheres enduring as a disordered phase on the surface of the crystal during growth, where they will crystallize on a well-ordered substrate (*69*). An example of these combined processes is the barnacle shell with calcite crystals retaining both a typical rhombohedral and nanoscale morphology (*69*).

ACC nanoparticles, stabilized by organic (e.g. proteins and amino acids) or inorganic additives (e.g. phosphate ions), could attach onto calcite faces and subsequently fuse within the crystalline structure to provide a nanogranular texture (*69*). In the absence of ACC-stabilized organic additives, faceted calcite crystals, exhibit initially nanogranular rough surfaces but smooth surfaces would be observed after dissolution-recrystallization events and aging, meaning that preservation of a nanostructure is achieved by the accumulation of macromolecules at the ACC nanoparticle surface (*76*). In addition, observations of ACC-containing vesicles in epithelial cells

in sea urchins (*86*), in bivalves (*87*) and in calcifying corals (*88*) are aligned more with the notion that the above-mentioned nanostructured biominerals form through a nonclassical crystal growth process.

1.3 Bioceramic model 1: Avian eggshell

1.3.1 Mineralization and structure

In vertebrate biology, calcified tissues are biphasic composites containing both noncollagenous and collagenous substances in contact with the inorganic (mineral) phase (*89*). In avian eggshell, these organic and inorganic components are present with the mineralized layers deposited onto the eggshell membranes in the shell gland of the laying hen. The avian eggshell is a complex bioceramic having a highly hierarchical and porous calcitic structure acting as a protection barrier for the growing embryo from physical damage and from microorganism contamination while also regulating gas and water exchange and temperature fluctuations from the external environment, and it also acts as a source of calcium for the embryonic chick skeleton (*90-92*). The shell develops at body temperature in a cell-free environment from the uterine secretion of its inorganic and organic constituents (*91, 93*).

Briefly, the egg consists of a central yolk enclosed by the albumen (the egg white), the eggshell membranes, the calcified eggshell and at the outermost surface of the shell, the cuticle (*91*) (Fig. 1.2). The egg formation process is similar among birds, and is especially well documented for the domestic chicken *G. gallus domesticus*. During its formation, avian egg develops all its layers as it passes through different regions of the oviduct (Fig. 1.3). In particular, following ovulation, as yolk moves through the oviduct the outer vitelline membrane and the albumen are deposited in the infundibulum and magnum region, respectively (*91*). After that, the

yolk and albumen composite travels to the white isthmus where the eggshell membrane components are secreted, with assembly taking place in about one hour (*91*). This resulting fibre meshwork is organized into a thin inner and a thick outer membrane sheet that surround the albumen (*91, 94, 95*). From this meshwork, the outer membrane sheets are mineralized at distinct sites, with the inner membranes remaining uncalcified (*92, 96*). Eggshell mineralization is initiated in the next oviduct region where the forming egg enters the red isthmus (tubular shell gland) region (*91*). Later, the forming egg enters the uterus (shell gland pouch) where the crystal nucleation sites on the outer membrane fibers become apparent (*91*).

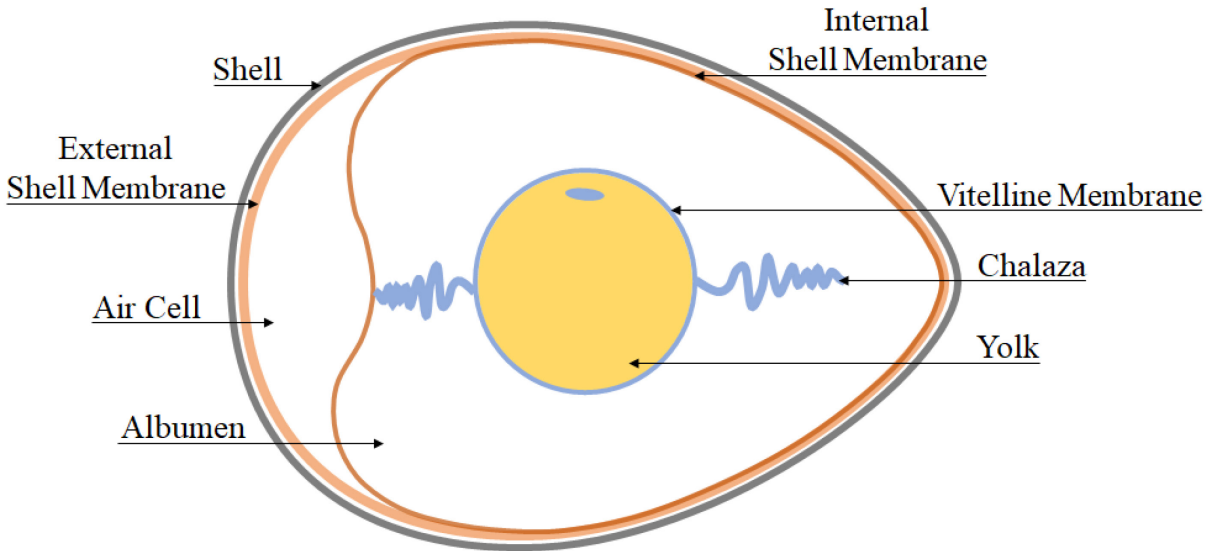

Fig. 1.2 Longitudinal section of a chicken egg showing its interior contents.

Avian eggshell calcification is characterized by the controlled precipitation of calcium carbonate in the form of calcite, and this occurs in the extracellular space between the eggshell membranes and the tubular wall of the oviduct (*91, 97*). During this mineralization process, the incomplete forming egg is immersed in a uterine fluid having concentrations 6 to 10 mM of calcium and approximately 70 mM of bicarbonate ions, which are 80-120 times larger than

calcite's solubility product (*91, 97, 98*). The mineralized eggshell consists of 96% (by weight) of calcite and ca. 4% of organic matrix including water and trace elements (*91*).

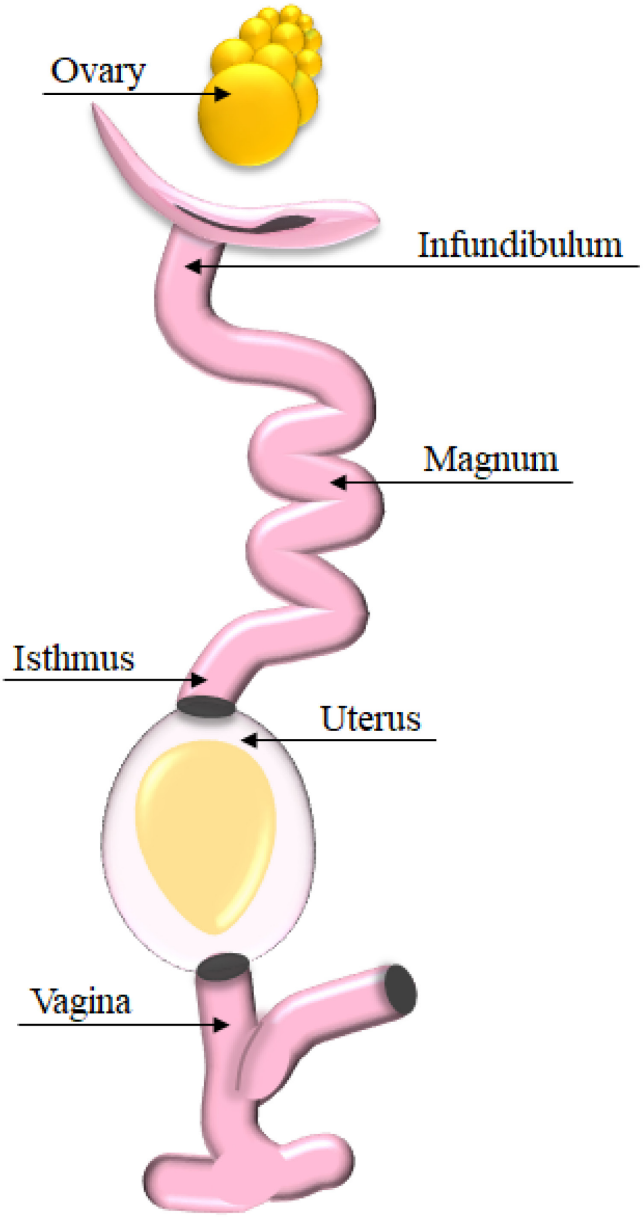

Fig. 1.3 The reproductive system of the hen showing the different regions of the oviduct [adapted from (*91*)].

Eggshell formation is known to be one of the fastest calcifying processes in biology. The total mineralization process lasts about 17 hours and it occurs in three stages (*91, 97*). After completion of mineralization, a well-structured avian eggshell has been formed as is described below from the inside (eggshell membranes) to its outside external surface: (i) the mammillae (or mammillary layer/ML), (ii) the palisades (or palisade layer/PL), (iii) the vertical crystal layer (VCL) and (iv) the cuticle (Fig. 1.4).

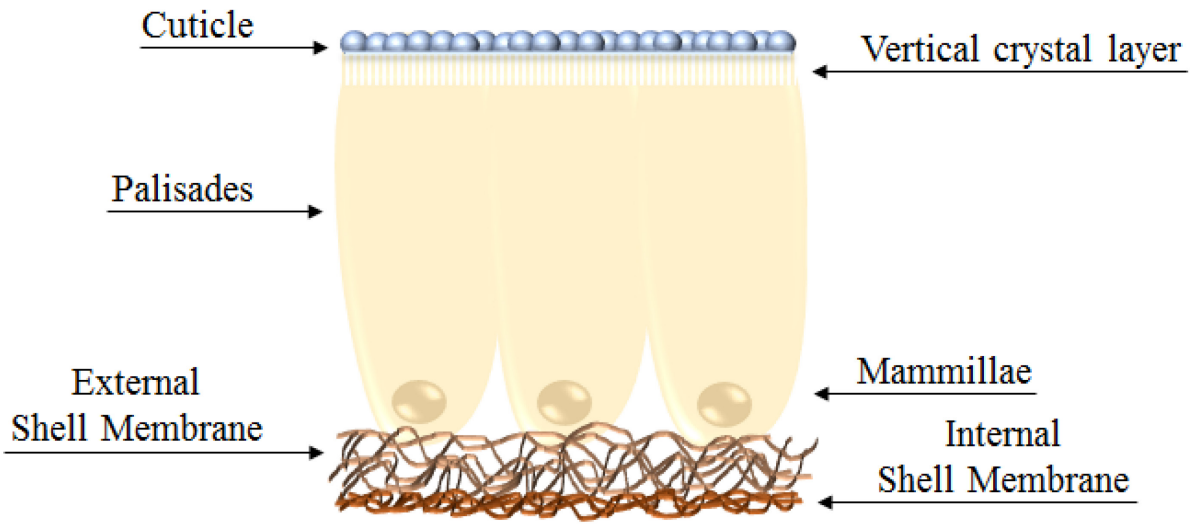

Fig. 1.4 Cross-sectional view of chicken eggshell showing its main compartments.

The first stage of eggshell mineralization lasts about 5 h and commences with the initiation of mineralization where the first calcite crystals are formed on the surface of the outer eggshell membranes (*97*). More specifically, before 5 h post-oviposition, mammillary cores are present on the outer shell membranes, whereas at 5 h post-oviposition, flat disk-shaped ACC particles accumulate over these cores. Progressively, these particles aggregate and transform into large calcite crystals, preserving a nanogranular structure (*99*). These nucleation sites become the origin of the ML, a solid arrangement of cones or knobs, which as they grow outwards, form the base of

the PL (*91*). Each mammillary cone consists of an assembled base plate, which is rich in organics and attaches to the outer portion of the eggshell membranes where mineralized individual fibres are incorporated (*100*). The base plate is capped by a calcium reserve body (CRB), the main calcium source for the chick embryo skeleton, encompassing a centrally positioned CRB sac, containing 200-300 nm spherical granules (*90, 100, 101*). The margin of CRB sac is covered by a membrane-like protein layer which is connected outwards with fibres and sheets of matrix (*90*). Above CRB is located a CRB cover and then, a CRB crown, where the palisades development initiates (*90, 101*). The space between the mammillae are fluid- or air- filled, and it is possible a protein layer exists at the surface of each mammillary cone to prevent their merging during eggshell mineralization (*90*).

Outwards from the mammillary layer extends the PL. This layer is comprised of aligned calcitic columns being perpendicular to the eggshell surface (*90, 91*). Palisades grow rapidly during the second stage of eggshell mineralization with a linear deposition of 0.33 g of calcium carbonate per hour for about 12 h (*97*). The PL comprises approximately 80% (~200 μm thick) of the shell with a regular array of pores found at specific sites among the columnar junctions permitting gas exchange (*90*). In the PL, microcrystal size increases gradually with elongation towards the eggshell surface along the crystallographic *c* axis of calcite (*91*). Full decalcification of fixed eggshell, or partial acid-etching, has revealed in the palisades an extensive organic matrix including sheets of matrix parallel to each other and often to the eggshell surface (*90*). In addition, prominent vesicular structures have been observed throughout the PL ranging from 200-500 nm in size (*90, 102*).

Just above the PL lies the VCL, referred to also as the vertical matrix layer (*101*). Intact and decalcified cross-sections of this layer have shown that mineral and matrix components have

either a parallel or an acute angle orientation close to the shell surface in the PL or almost a perpendicular orientation at the outer eggshell surface (*90*). Acid and bleaching methods have revealed an extensive fibrous matrix and mineral components vertically oriented (*90*). Like the palisade layer, spherical voids have been also observed in the VCL, but they are fewer in number (*90*). Eggshell structural organization at different levels influences its mechanical properties. Crystal size and shape, and crystallographic orientation, all affect an eggshell's mechanical properties, where increasing preferential orientation of the crystals lead to a decrease in eggshell strength in the case of young hen eggs (*103*). In addition, stiffness (or elastic modulus E) maps obtained by nanoindentation, from the egg equator and both, sharp and large ends, denoted a random E distribution in the PL and ML, showing that local chemical or crystal orientation variations affect mechanical properties of eggshells (*104*).

The third and final stage where eggshell mineralization is terminated, lasts about 1.5 h and is related to cuticle formation (*96*). The cuticle coats the VCL and is characterized by a variable thickness over the shell surface, and which in some cases can be completely absent (*90*). A typical cuticle thickness has been reported to range from 5 to 10 μm (*105*). Cuticle deposition provides the first defence barrier against the penetration of pathogenic microorganisms into the egg contents (*106*). The cuticle thickness becomes greater near the pores (for exchange of gases) where cuticular material spans and fills the upper pore space and thus limits the passage of pathogens through the eggshell (*97, 107*). It is also believed to play a role in water exchange by limiting water loss, and restricting microbial colonization of the shell surface (*97*). The cuticle is divided into an inner zone containing spherical hydroxyapatite crystals, whereas the outer zone is mostly organic (*91, 101*). Although it is not yet well understood, it is believed that the calcification is inhibited by phosphorylated proteins since $CaCO_3$ precipitation is inhibited in vitro by molecular components

present in the uterine fluid during the terminal phase (*108*). Likewise, phosphorus ions have been detected at the chicken eggshell exterior (*109*) which are also known to inhibit $CaCO_3$ precipitation (*110*).

1.3.2 Organic constituents of uterine fluid and avian eggshell

In avian eggshell, the insoluble organic components are essential for supporting initiation of crystal nucleation at distinct sites. On the other hand, the soluble organic matrix participates in polymorph selection, modifies crystal morphology and orientation and incorporates also within the mineral phase, regulating its macroscopic and mechanical properties (*91, 93*).

Proteomic analysis of the uterine fluid during egg mineralization suggest specific roles for different organic components over the three calcification stages (initial, growth and terminal) (*97, 108, 111*). Experimental observations using whole uterine fluid have shown modifications in the precipitation kinetics of calcium carbonate favouring calcite polymorph development and altering the morphology and size of synthetic calcite crystals grown in vitro *(112, 113)*. Harvested uterine fluid during the initial stage of eggshell mineralization promotes crystal nucleation whereas collected uterine fluid during the calcification growth phase improves $CaCO_3$ precipitation kinetics (*91*). On the contrary, the collected uterine fluid from the terminal calcification stage inhibits calcite precipitation (*114*). These observations indicate that purified eggshell matrix proteins that inhibit $CaCO_3$ precipitation lead to modified morphologies of the typical rhombohedral shape of calcite crystals grown in vitro *(115)*.

1.3.2.1 Eggshell membranes

The albumen (or egg white) is enveloped by a fibre meshwork, the inner and outer eggshell membranes, which allow for gas and water exchange. The eggshell membranes are deposited when the forming egg passes through the white isthmus region of the oviduct (*97*). Eggshell membrane fibres consist of 10% collagens of types I, V and X as well as of 70-75 % of other proteins and glycoproteins including lysine-derived cross-links (*95, 116-118*). Only the outer eggshell membranes provide the nucleation sites for mineralization giving rise to the mammillary cones (*92, 96*). The secretion of keratan sulphate proteoglycan by the red isthmus gland cells (*119*) coincides with the first mineral nucleation sites and calcium removal supplying the chick embryo (*118*). Even though the mechanism that prevents the calcification of inner membranes is not well understood, it is believed that collagen type X prevents this calcification event (*92, 120*). Inhibition of fibre formation or modifications of lysine-derived cross-linking by aminopropionitrile or by copper deficiency alters the eggshell membranes, consequently affecting eggshell formation and decreases its mechanical properties (*120, 121*).

1.3.2.2 Eggshell matrix proteins

Proteomic approaches have identified more than 500 eggshell proteins (*122, 123*). Eggshell matrix proteins compose an organic matrix of insoluble and soluble proteins, and include phosphoproteins, glycoproteins, and proteoglycans (*91*).

The eggshell-specific proteins are unique to the eggshell mineralization process and are secreted by cells in specific oviduct regions (*97*). These matrix proteins are termed the ovocleidins (*ovo*, Latin – egg; *kleidoun*, Greek – to lock in) and ovocalyxins (*ovo*, Latin – egg; *calyx*, Latin – shell) (*91, 97*). Ovocleidins and ovocalyxins, highly expressed in the red isthmus and uterus, are

thought to be involved in eggshell mineralization regulation, and anti-microbial protection (*97, 124-127*). Ovocleidin-17 (OC-17) is an abundant phosphoglycoprotein eggshell-specific protein (40 μg/g shell) which is secreted by the tubular gland cells of the shell gland and is concentrated in the mammillary cones (*126, 128*). OC-17 can create twinned calcite crystals as grown in vitro (10-100 μg/ml) or crystal aggregations in a concentration-dependent manner (50-200 μg/ml) (*129, 130*). In addition, computational studies have predicted that OC-17 can activate ACC transformation into calcite (*131*). Ovocleidin-116 (OC-116) is a 116-kDa eggshell matrix phosphoprotein, estimated to be 80 μg/g of shell, and found in the uterine fluid during the active shell calcification stage (*125, 132*). It is secreted by the granular cells of the uterine epithelium and is distributed throughout the palisade layer (*125*). OC-116 is also present in chicken embryonic osteoblasts and osteoclasts, chick cortical bone, the medullary bone of laying hens, and the hypertrophic zone of the cartilaginous growth plate (*133, 134*), thus indicating that it is not an eggshell-specific protein.

Ovocalyxin-32 (OCX-32) has been identified as a 32-kDa phosphorylated protein, secreted into the uterine fluid from the isthmus regions of the oviduct (*124*). OCX-32 is abundant during the terminal stage of shell calcification where it has been found to co-precipitate with $CaCO_3$ in vitro from fresh uterine fluid (*108, 112, 135*). In the calcified shell, OCX-32 is localized to the outer portion of the PL, the VCL and the cuticle (*124*). Ovocalyxin-36 (OCX-36) is a uterine fluid 36-kDa protein, detected in the isthmus and uterus regions of the oviduct during the active stage of shell mineralization (*136*). OCX-36 is abundant in the shell membranes and it is localized primarily to the inner part of the calcified shell (*91, 127*).

Egg white proteins including ovotransferrin, lysozyme and ovalbumin are also present in the uterine fluid and are mainly localized to the shell membranes and the mammillary cones (*94,*

137-139). In vitro calcite crystal growth experiments with ovotransferrin used at a concentration of 0.5 mg/ml have shown the precipitation of smaller and elongated crystals (*138*). Experiments with high concentration of lysozyme (>10 mg/ml) leads to the growth inhibition of calcite {110} crystallographic faces (*94, 140, 141*). Ovalbumin has been found to stabilize amorphous calcium carbonate at an early mineralization phase (*142-144*).

Finally, OPN, a protein observed also in many tissue fluids and tissues, has been detected both in chicken bone and eggshell, but differs there in its post-translational modifications (*102*). Strong OPN gene expression by cells has been detected in the shell gland portion of the oviduct (*145*) which is associated with eggshell mineralization, and OPN has been directly detected as an eggshell constituent (*90, 102*).

1.4 Bioceramic model 2: Otoconia

1.4.1 Vestibular system of the inner ear

All living organisms detect the features of their environment in respect to spatial orientation and the directional forces of gravity. The inner ear performs all the functions for maintaining the equilibrium of the organisms. It contains two labyrinths, a membranous labyrinth within a bony labyrinth. Both membranous and bony labyrinths are filled with a different ionic composition fluid called endolymph and perilymph, respectively (*146*). The bony labyrinth of the inner ear is divided into the semicircular canals, the vestibule, and the cochlea. Semicircular canals and vestibule comprise the vestibular system of the inner ear involved in body balance (*146, 147*). The vestibular apparatus functions as a sensory system detecting head motions at any horizontal, vertical or torsional direction for achieving body balance. There are three fluid-filled semicircular canals responding to rotational acceleration and two membranous sacs inside the vestibule, the utricle

and the saccule, responding to linear acceleration and gravity (*146, 147*) (Fig. 1.5). The utricle and saccule (and lagena in non-mammalian vertebrates) are also referred as otolithic organs due to the fact they contain $CaCO_3$ biocrystals called otoconia (or otoliths in fish) (*9, 148*).

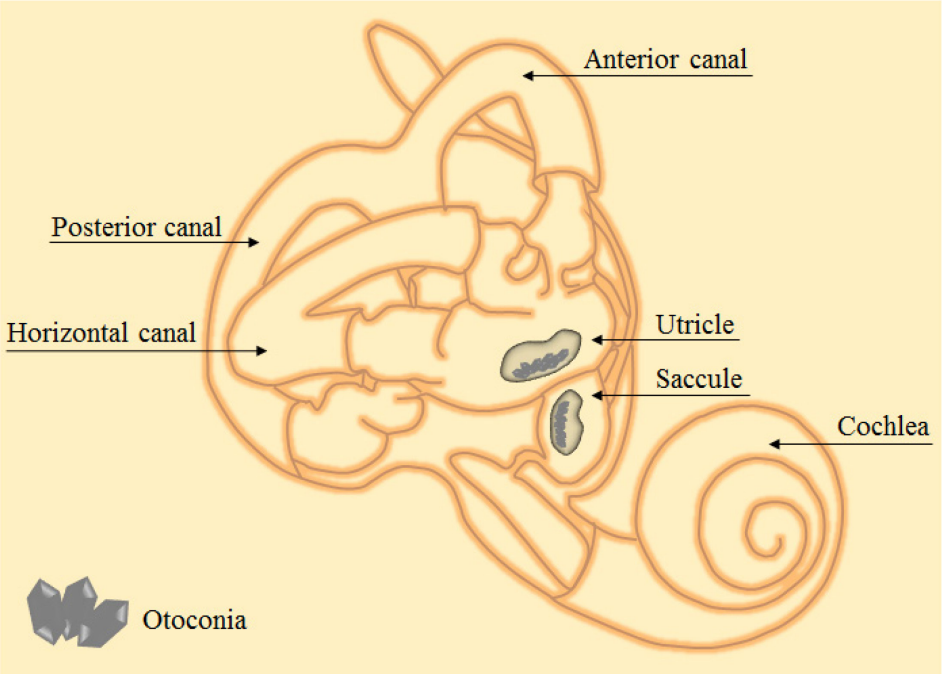

Fig. 1.5 The vestibular system of the inner ear and its main compartments. The semicircular canals and the two membranous sacs, the utricle and saccule, are balance sensory organs, while the cochlea is the auditory sensory organ.

1.4.2 Otoconia

Otoconia are $CaCO_3$ crystals containing proteins, partially embedded in the otoconial membrane, a gelatinous matrix layer playing a vital role in mechanotransduction processes where mechanical stimulus is converted by sensory cells to electrochemical signals (*9, 148, 149*). Otoconia, along with the otoconial membrane, are anchored to the hair cell kinocilia and stereocilia in the utricular and saccular sensory epithelium, named the macula (*9, 150*). Head movement

displaces this otoconial complex, producing hair-bundle motions that subsequently modify the sensory hair cells (*151*). This mechanical induction is converted to electrical signals by the hair cells and conveyed to the central nervous system (CNS) via the afferent vestibular nerve. Afterwards, in the CNS, combination of these electrical signals with other proprioceptive inputs, initiates neuronal responses for maintaining the balance of the body. The correct size and density of otoconia is critical for the vestibular function and CNS provocation (*152-154*).

1.4.2.1 Inorganic phase of otoconia

In mammals, as well as in birds, the main inorganic component of normal otoconia is exclusively calcite (*155-157*). Other $CaCO_3$ crystalline polymorphs such as aragonite and vaterite are evident throughout different animals and sometimes under pathological conditions in human inner ears (*158, 159*). Reptilian otoconia have been reported to be mainly calcite (*160*). Amphibian otoconia are aragonitic (*148*) except for some species (e.g. *Rana esculenta*) containing calcitic otoconia (*161, 162*). Fish otoliths have been described as aragonitic with some primitive fish otoliths having apatite (calcium phosphate) (*155*) and *Chondrostean* fish have otoliths of vaterite (*163*). Fish otoliths are formed initially at 18 to 20 h after fertilization, adhere to the immature hair cells called tether cells, and by 24 h are mineralized as aragonite (*164*). In otoliths, incremental growth layers are added daily during the life of the fish, diverging in thickness and composition depending on the living environment (*165*). Mammalian otoconia develop at late embryonic stages, become mature soon after birth, and likely require some degree of maintenance (*149, 166*). The formation of otoconia starts in the endolymphatic space away from the cells after secretion and assembly of the required components (*164*).

1.4.2.2 Organic components in otoconia and otoconial membrane

Otoconial $CaCO_3$ crystalline structure and morphology are controlled by a ubiquitous organic matrix consisting of proteins and proteoglycans (*167, 168*). Otoconial proteins are commonly denoted as otoconins and are essential for $CaCO_3$ crystallization as they bind calcium ions from the low-calcium endolymph (*163, 169, 170*). Until now, the following otoconins have been identified: Otoconin-90 (Oc90) (*171, 172*), which is considered the predominant otoconial protein and minor otoconins such as otolin-1 (or otolin) (*167, 168*), fetuin-A (*173*), OPN (*174, 175*), Sparc-like protein 1 (Sc1) (*173, 176*), Secreted protein acidic and rich in cysteine (Sparc), dentin matrix protein 1 (DMP1) (*176, 177*) and α-tectorin (*176*). Oc90 is the most abundant otoconin, extremely acidic glycoprotein rich in cysteines which enables calcium ion or $CaCO_3$ binding (*178*). It is required for the formation of otoconial matrix by recruiting specific components (*168*). Both in vivo and in vitro studies have shown that Oc90 enables $CaCO_3$ nucleation and growth (*178*) while changes in its expression occur simultaneously with the timing of otoconial development (*179*). In the absence of Oc90, no otoconia or few giant otoconia susceptible to dissolution are formed with Sc1 protein levels being greatly increased (*180*). Even though Sc1 and Oc90 sequences have no similarity, they share some common features. Sc1 is also an acidic glycoprotein rich in cysteines, and is able to bind calcium similar to Oc90 (*176*). Thus, these similar characteristics with Oc90 allow Sc1 to compensate for the absence of Oc90. Otolin is a collagenous inner-ear specific glycoprotein, present in both otoconia and fibrous membranes (*167*). Specific domains of otolin interact with Oc90 to develop the otoconial matrix and segregate calcium for otoconial formation (*181*). In in vitro experiments, the presence of otolin is necessary for Oc90 to generate calcite crystals with a morphology similar to otoconia (*182*). Otoconins, such as fetuin-A, Sparc, OPN and DMP1 have negligible or no effect on otoconial formation and

vestibular function (*168, 175, 176*). However, in other mineralized tissues, such as in bone, OPN and fetuin-A have important roles in the calcification of bone matrix (*168, 183*). Other candidates for mediating otoconial mineralization are the keratan sulfate proteoglycans (KSPGs) (*176*), having strong negative charges for attracting calcium ions and they appear to interact with Oc90 and otolin (*9*), but a detailed analysis of their role on otoconial formation has not yet been performed.

Proteins found in the otoconial membrane are crucial for the normal development of otoconia. The otoconial membrane consists of both collagenous (otolin) and noncollagenous glycoproteins such as otogelin, otogelin-like, a-tectorin, b-tectorin, and otoancorin, and KSPGs proteoglycans (*9, 177*). Otogelin is present in the acellular (tectorial and basilar) membranes in the cochlea of the inner ear (*184*), is expressed in the supporting cells and in the vestibule during the adulthood (*185*) and is critical for otoconial membrane adhesion to the sensory epithelia (*9*). The *Otogelin* mouse has deficits in its acellular membranes (*186*) and, the mice are deaf due to abnormalities of the fibrillar network organization in the tectorial membrane (*9, 154*). Otogelin-like gene is expressed in otoconial, tectorial and basilar acellular membranes and the cochlear and saccular hair cells, with its expression levels being again high during embryonic development that decrease towards the adulthood (*9*). Alpha- and β- tectorin are found in the mammalian otoconial and tectorial membranes (*176, 187*). Mice with deletion of α-tectorin protein reveal degraded otoconial membrane and only a small number of dispersed massive otoconia (*188*). Null mice of β-tectorin display a low frequency hearing loss due to structural defects of the tectorial membrane (*189*). Finally, otoancorin is an anchored-protein, expressed on the surface of the utricular and saccular supporting cells, possibly facilitating otoconial membrane adhesion to the sensory epithelia after interaction with otogelin and tectorins (*190*).

1.4.2.3 Otoconial disorders

Balance disorders related to otoconia formation and dislocation are common. Multiple causes such as aging, head trauma, ototoxic drugs and genetic mutations can cause otoconial malformations leading to a higher risk of a falling, that could cause severe injuries (*9*). Utriculolithiasis describes the pathological condition where otoconia exist in larger numbers other than at the active surface area of the utricular cells (*191*). Canalolithiasis refers to otoconial detachment and entrapment within the semicircular canals (*191, 192*). These pathological states could be responsible for the development of benign paroxysmal position vertigo (BPPV), the most frequent cause of dizziness in humans (*193*). In contrast, cupulolithiasis, the attachment of otoconial debris to the cupula, a gelatinous protein-polysaccharide structure at the end of each semicircular canal (*191, 192*), cannot be considered alone as a cause of BPPV (*192*).

Women are more likely to experience BPPV than men (*194, 195*), while in elderly people, this seems to be a significant factor for increasing injury and mortality rates due to falls (*196*). Alterations in calcium metabolism during aging or during a pathological process such as osteoporosis (loss of bone mass) can also be the cause of BPPV (*197-199*).

1.5 Osteopontin

OPN is a secreted, highly acidic mineral-binding phosphorylated glycoprotein, and a member of the SIBLING (**S**mall **I**ntegrin-**B**inding **LI**gand, **N**-linked **G**lycoprotein) protein family whose genes are clustered on human chromosome 4 (*200*). OPN is associated with mineralization under both physiologic and pathologic conditions (*201*). In physiologic conditions, OPN has been localized to bones, teeth and mammalian otoconia (*174, 202*), whereas in pathologic conditions, OPN expression has been observed in kidney stone formation and vascular calcification (*203, 204*), as well as on luminal surfaces of epithelial cells of specific organs, such as gastrointestinal and reproductive tracts, gall bladder, pancreas, breast, lung and salivary glands (*205*). Although OPN is incorporated into the matrix of mineralized connective tissues, it appears also in biological fluids having high levels of calcium, such as in milk, urine and blood (*206-208*). OPN is implicated in cell adhesion, cell signalling, cell migration, chemotaxis and mineral-binding, justifying its role as a multifunctional protein (*209*). Integrin-binding and mineral-binding functional motifs have been identified in a full-length OPN; however, post-translational modifications regulate its various tissue-specific function (Fig. 1.6).

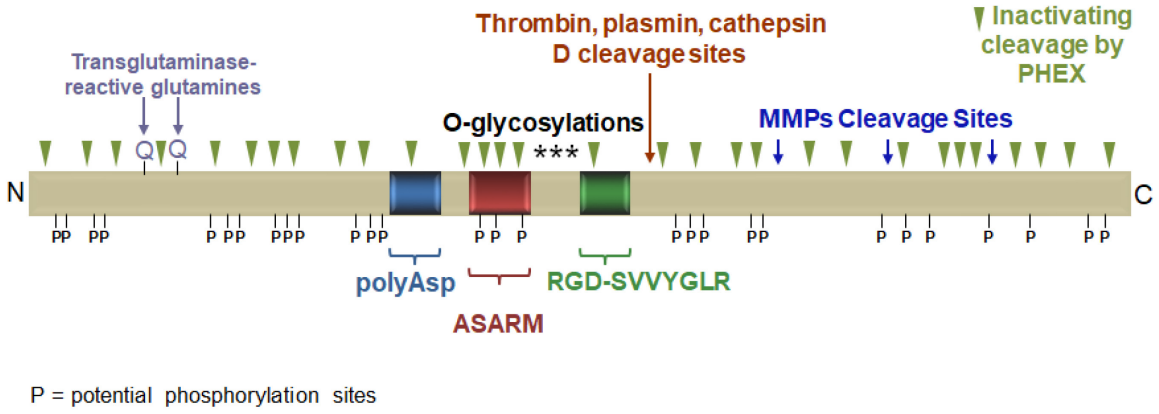

Fig. 1.6 Post-translational regions and functional motifs on full-length OPN sequence.

1.5.1 Functions of OPN

OPN has proven to be a multifunctional protein present in most tissues and body fluids and implicated in numerous biological processes including cell migration and survival, regulation of immune cell function, tumor control and inhibition/regulation of mineralization (*210-213*). Loss of OPN has important consequences such as in bone remodelling, renal injury, bacterial infection, tumor development, and in increased mineralization (*214-217*). The function of OPN is mainly regulated through proteolytic processing and phosphorylation.

In diverse cells, OPN mediates cell attachment, cell migration, chemotaxis and intracellular signalling through interactions with integrin receptors. The $\alpha_v\beta_6$, $\alpha_v\beta_3$, $\alpha_v\beta_5$, $\alpha_5\beta_1$, $\alpha_v\beta_1$, and $\alpha_8\beta_1$ integrins bind OPN through its arginine-glycine-aspartic acid (RGD) motif (*218-224*). OPN provokes signals among the same or different cells by several heterodimeric combinations of integrin chains (*209*). Thrombin cleavage of OPN generates binding sites for $\alpha_9\beta_1$ and $\alpha_4\beta_1$ integrins and a non-RGD binding motif referred as Ser-Val-Val-Tyr-Gly-Leu-Arg (SVVYGLR) (*225-227*). Moreover, cleaved-OPN by members of the matrix metalloproteinase (MMP) family, plasmin and cathepsin D, result in N-terminal OPN fragments that interact with both RGD and SVVYGLR motifs (*228, 229*). Thrombin, MMPs, plasmin, but not cathepsin D, cleaved OPN promotes cell adhesion and migration compared to the full-length OPN protein (*228, 229*). OPN fragment, retains RGD motif and increasing OPN attachment as well as its migration and adhesion properties (*230*). Consistent with the OPN proteolytic process that enables binding to integrin motifs, conformational modifications by tissue transglutaminase 2 (TG2) enzyme also have an influence on integrin binding. Polymerized OPN, observed in bone and in vascular calcified tissue, improves cell-adhesion and provokes chemotaxis of neutrophils (*231, 232*). PHEX enzyme,

produced by cells in bone and tooth (*233, 234*), hydrolyze OPN throughout its full-length (Fig. 1.6), inactivating its inhibitory influence on bone mineralization (*235*).

OPN is also a ligand for the CD44 family of receptors and its variants (*236, 237*). CD44 is a transmembrane glycoprotein expressed in highly invasive human cancers regulating metastasis (*238*). CD44 binds to OPN via its RGD motif inducing cell migration out of the blood circulation to inflammation sites (*238*). Previous studies indicate that chemotaxis, motility and cell spreading can be promoted by CD44 variants that together with β1-containing integrins, bind to OPN independently of RGD sequences (*237*).

In addition to its anionic charge disclosed by the several aspartic (Asp/D) and glutamic (Glu/E) acids found on its sequence, post-translational modifications such as phosphorylation play an essential role for increasing the mineral-binding ability of OPN (*239-241*). Human OPN with a protein sequence of 314 amino acids includes 36 potential phosphorylation sites (*242*), while mouse OPN is a 294 amino-acid sequence with 27 phosphorylation sites (*243*). Bovine OPN consisted of 278 amino acids with 28 phosphorylation sites (*244*) and chicken OPN with a 264 amino acid-length sequence is reported to include phosphorylated peptides concentrated at the N-terminal end and towards the C-terminal end (*245*). The phosphorylation levels vary significantly between different tissues and tissue fluids reflecting its specific role at these sites (*244*).

Post-translational modifications increase the tendency of OPN to disorder, something that is also has relevance to its mineral-binding ability since the open structure facilitates the interactions with mineral (*200*). In chicken, partially purified eggshell-extracted OPN acts as a strong inhibitor of calcium carbonate precipitation in a phosphorylation-dependent manner (*246*). OPN has also been shown to bind preferentially to calcite {104} crystal faces (*90*). Similar to these observations with calcium carbonate, phosphorylated-dependent interactions are also evident in

other biominerals. OPN has an inhibitory effect on hydroxyapatite growth with phosphorylated OPN peptides be more potent inhibitors than the nonphosphorylated ones (*247*). OPN also has two highly conserved acidic and phosphorylated mineral-binding motifs, a poly-aspartic rich region (e.g. ^{86}DDLDDDDD^{93} in bone OPN or ^{99}DDDDDDDND^{107} in chicken eggshell OPN) and an acidic, serine- and aspartic acid-rich (^{115}DDpSHQpSDEpSHHpSDEpSDEL^{132}/ASARM) region (*209, 248, 249*). Phosphorylated OPN ASARM inhibits mineralization of the extracellular matrix in an osteoblast culture model, like full-length OPN, in a phosphorylation-dependent manner (*250*). Dephosphorylation of OPN and blocking of acidic carboxylate groups reduce its inhibitory role on hydroxyapatite crystal growth (*251*). Likewise, addition of OPN to MC3T3-E1 osteoblast cell cultures reduces mineral formation whereas OPN dephosphorylation or ASARM peptides with only 3 phosphorylation sites had no longer a mineral inhibitory effect (*239, 250*). Furthermore, in the urinary system, OPN and its derived-peptides inhibit calcium oxalate monohydrate crystal growth by binding preferentially to specific crystal faces followed by their incorporation within these crystals (*252-258*). Given the intriguing interplay between proteins and biominerals, this thesis examines two calcitic biominerals, the avian eggshell of *G. gallus domesticus* and mouse otoconia at the nanoscale.

Chapter 2 - Nanostructure, osteopontin and mechanical properties of calcitic avian eggshell

D. Athanasiadou,[1] W. Jiang,[1] D. Goldbaum,[2] A. Saleem,[2] K. Basu,[3] M. S. Pacella,[4] C. F. Böhm,[5] R. R. Chromik,[2] M. T. Hincke,[6] A. B. Rodríguez-Navarro,[7] H. Vali,[3,8] S. E. Wolf,[5,9] J. J. Gray,[10] K. H. Bui,[8] M. D. McKee[1,8*]

[1]Faculty of Dentistry, McGill University, Montreal, QC H3A 0C7, Canada.

[2]Department of Mining and Materials Engineering, McGill University, Montreal, QC H3A 0C5, Canada.

[3]Facility for Electron Microscopy Research, McGill University, Montreal, QC H3A 0C7, Canada.

[4]Department of Biomedical Engineering, Johns Hopkins University, Baltimore, MD 21218, USA.

[5]Department of Materials Science and Engineering, Institute of Glass and Ceramics, Friedrich-Alexander-University Erlangen-Nürnberg, Erlangen 91058, Germany.

[6]Department of Cellular and Molecular Medicine and Department of Innovation in Medical Education, University of Ottawa, Ottawa, ON K1H 8M5, Canada.

[7]Departamento de Mineralogía y Petrología, Universidad de Granada, Granada 18002, Spain.

[8]Department of Anatomy and Cell Biology, McGill University, Montreal, QC H3A 0C7, Canada.

[9]Interdisciplinary Center for Functional Particle Systems (FPS), Friedrich-Alexander University Erlangen-Nürnberg (FAU), Haberstrasse 9a, Erlangen 91058, Germany.

[10]Department of Chemical and Biomolecular Engineering, Johns Hopkins University, Baltimore, MD 21218, USA.

This study was originally published in Science Advances

Vol. 4, no. 3, eaar3219

DOI: 10.1126/sciadv.aar3219

2.1 Abstract

Avian (and formerly dinosaur) eggshells form a hard, protective biomineralized chamber for embryonic growth—an evolutionary strategy that has existed for hundreds of millions of years. We show in the calcitic chicken eggshell how the mineral and organic phases organize hierarchically across different length scales and how variation in nanostructure across the shell thickness modifies its hardness, elastic modulus, and dissolution properties. We also show that the nanostructure changes during egg incubation, weakening the shell for chick hatching. Nanostructure and increased hardness were reproduced in synthetic calcite crystals grown in the presence of the prominent eggshell protein osteopontin. These results demonstrate the contribution of nanostructure to avian eggshell formation, mechanical properties, and dissolution.

2.2 Introduction

The avian (and formerly dinosaur) eggshell is a thin, mineralized (calcite) layer that adequately protects the egg content and allows for the extra-uterine development of the chick embryo. Besides its protective function, its partial dissolution and thinning from the inside out during fertilized egg incubation serves as a source of calcium required for calcium-phosphate mineralization of the growing embryonic chick skeleton. This partial dissolution of the inner aspect of the shell also facilitates chick hatching/pipping. We hypothesized that these diverse functions of the remarkably designed and evolutionarily persistent avian eggshell likely result from regional differences in nanostructure; basic eggshell structure has been conserved over hundreds of millions of years of evolution.

The eggshell of the domestic chicken (*G. gallus domesticus*) is about 95% (by weight) calcium-carbonate mineral in the form of calcite and about 3.5% (by weight) organic material/matrix (including water) (*93*). Among hundreds of proteins identified by proteomics and various other means in the eggshell organic matrix (*90, 122, 126, 259*), osteopontin (OPN, the name deriving from its initial discovery in bone) is a major shell matrix protein (*145*), and a member of a group of mineral-binding proteins (*200*) thought to be prominent in guiding mineralization processes because of their particularly high negative charge and open flexible structure (*200, 260*). These proteins are intrinsically disordered (*260*) and are thought to have arisen from ancestral gene-duplication events. Their high negative charge (involved in calcium binding and mineral binding) partly derives from an abundance of acidic amino acids (Asp and Glu). In addition, many Ser residues are phosphorylated (this is particularly so for OPN), which imparts additional negative charge to bind ionic calcium and crystal lattice calcium (*261*).

Living organisms produce a wide variety of biominerals for a variety of purposes. Biominerals form hardened structures that often have complex architectures that are hierarchically organized, such as the human skeleton where calcium-phosphate mineral prevails, with nanocrystals forming within an extensive, fibrillar organic macromolecular assembly known as the extracellular matrix. On the other hand, terrestrial and marine organisms typically use calcium-carbonate mineral polymorphs to build functionalized biomineralized structures such as seashells, snail shells, and eggshells. These rigid structures are hybrid composite materials where organic-inorganic (protein-mineral) interactions largely improve mechanical properties, such as hardness and toughness, to adequately provide supportive and/or protective functions to the organism in which they are assembled (*5*).

In recent years, there has been much work focusing on the structural analysis of various calcareous biominerals at the nanometer length scale. In many cases, closely packed nanosized subunits that are essentially perfectly aligned have been observed to form through nonclassical crystallization pathways (*262*). These alternative pathways may give rise to crystalline material having a nanogranular structure that produces a single-crystal diffraction pattern as would be obtained for a single, "monolithic" crystal otherwise not having nanosubstructure. Mollusk shells, fish otoliths, coral skeletons, and brachiopods all have been described as having an internal nanogranular structure (*2*). Although in vitro experiments have evaluated the influence of organic material on calcium-carbonate polymorph selection (*37*), little is actually known about the mechanisms through which biomolecules affect nanogranular structure in living organisms.

Here, we have investigated, at the nanoscale, the structure of the eggshell from chicken (*G. gallus domesticus*), and OPN incorporation and have identified the existence of nanogranular structure in this shell. We have additionally correlated this nanostructure with functional properties

(hardness, elastic modulus and dissolution). These findings extend our knowledge of how incorporated organic constituents can substantially enhance mechanical properties and controlled solubility in biostructures (*58*), observations that align with alloy fabrication studies showing that dual-phase nanostructuring can nearly attain theoretical ("ideal") strength in synthesized materials (*263*). Here, we correlate nanostructure with hardness and elastic modulus in the chicken eggshell. We also describe changes in shells from eggs that have been partially naturally dissolved after physiologic fertilization and incubation, two processes required for chick embryo development. Finally, we report that occluded OPN (an abundant protein in eggshell) can induce nanostructure in synthetic (nonbiogenic) calcite, much like what we have observed in the chicken eggshell.

2.3 Materials and methods

2.3.1 Eggshells

The total number of White Leghorn domestic chicken (*G. gallus domesticus*) eggs studied for these results was 30 (this includes unfertilized and fertilized incubated eggs). For each data set collected, at least two to six shell fragments from different eggs were examined by the respective methodologies; all results were reproducible, and we will show typical examples. Eggshells were prepared according to the method described by Chien *et al*. (*90, 264*). Briefly, eggshells were washed with physiologic saline (150 mM sodium chloride solution) and double-distilled water, and air-dried at room temperature. A portion of the air-dried or fixed (and sometimes demineralized) shell fragments, removed from the equatorial region of the eggshell, were embedded in LR white acrylic resin (London Resin Company) for microtome sectioning and microscopy analyses. In addition, shell cross sections of approximately 100 μm in thickness were cut using a diamond saw rotating disc (model VC-50 Precision Diamond Saw, LECO).

2.3.2 Chemicals and OPN

For crystallization experiments, anhydrous calcium chloride ($CaCl_2$) was purchased from Thermo Fisher Scientific, and ammonium carbonate [$(NH_4)_2CO_3$] was purchased from Sigma-Aldrich. Bovine phosphorylated milk OPN (with approximately 24 phosphorylations per molecule) was provided by Arla Foods and was prepared according to the method described by Sørensen and Petersen (*265*).

2.3.3 Atomic force microscopy

AFM was conducted on eggshell fragments that were cut with a diamond saw and polished across a series of water stones from rough 1,000 grit to fine 13,000 grit (Lee Valley Company), followed by ultrasonication and washing. Height and amplitude images were taken using a Nanoscope IIIa (Veeco) operating in tapping mode at room temperature in air, using a vertical-engage E scanner and NanoScope version 5.30 software (Veeco/Bruker-AXS Inc.). V-shaped tapping mode probes (typical tip apex radius of approximately 7 nm) with Si cantilevers having a spring constant $k = 42$ N/m (Bruker-AXS Inc.) were used. To reduce imaging artifacts, the tip force exerted on the surface was optimized by the amplitude set point being as high as possible. The Feret diameters and area measurements of the units comprising the nanostructure observed by AFM were calculated using ImageJ software. At least 100 Feret diameters and 100 area measurements of the nanostructure of each eggshell layer from fertilized incubated and nonincubated eggs, as well as from each synthetic calcite crystal grown in the presence of OPN (0.9 and 5.9 μM), were calculated from AFM images (obtained using amplitude mode) after performing high-pass processing to enhance boundaries.

2.3.4 Scanning electron microscopy

Examination of the external morphology of synthetic calcite crystals grown with or without OPN was performed using a FEI Inspect F-50 FE-SEM (FEI Company) operating in high-vacuum mode at 5 kV. For eggshell nanostructure observations, samples were sputter-coated with an approximately 2-nm Cr layer using an EMS150T Turbo-Pumped Sputter Coater.

2.3.5 FIB sectioning for TEM

Approximately 80-nm-thick sections (lamellae) were prepared using a dual-beam FIB microscope (FEI Helios 600 NanoLab, FEI) equipped with a gallium ion source. Samples were mounted on flat aluminium SEM stubs and coated with a 2-nm platinum layer. For the ion-beam preparation, a rectangular section (2 µm thick) of a Pt protection layer was deposited on the area of interest, after which an eggshell slab with a thickness of 2 µm was milled by the ion beam, and the section was transferred for the final thinning onto a copper TEM half-grid using an EasyLift nanomanipulator. The lift-out section was further milled at 30 kV and 9.4 nA, and final thinning was carried out at 30 kV and 0.77 nA to reach a thickness of 80 to 100 nm.

2.3.6 Wedge polishing for TEM

Electron-transparent wedge-shaped thin sections of eggshells were prepared on a MultiPrep precision polishing system (Allied High Tech) using a waning series of micrometer-sized diamond polishing films (from 30 mm down to 0.1 mm; Allied High Tech) while obeying the rule of the "trinity of damage" [see the study of Hovden *et al*. (*35*)]. A nonaqueous lubricant (DP-Lubricant Brown) was used to prevent mineral dissolution. Samples were fixed onto a Pyrex-polishing stub (Allied High Tech) with Loctite super glue (Henkel AG & Co. KGaA), allowing gentle removal

later by means of an acetone bath. The convex side of the eggshell was polished at an angle of 10° until all of the different mineral layers were visible at the sample's edges. The sample was then carefully removed from the stub, flipped upside down, and again polished under an angle of 2° using a waning series of lapping films. As soon as the tip of the wedge-shaped sample showed fringes, the sample was carefully removed from the stub and mounted to an annular molybdenum TEM grid (Plano GmbH) with M-Bond 610 epoxy (VPG).

2.3.7 Transmission electron microscopy

HRTEM was performed to examine crystal lattice fringes on thin (~80 nm) FIB sections of eggshell and of synthetic calcite crystals grown in vitro with (or without) OPN. TEM images using the bright-field mode, as well as SAED patterns, were acquired using a FEI Tecnai G^2 F20 microscope operating at 200 kV equipped with a Gatan UltraScan 4000 charge-coupled device (CCD) camera model 895 and an aperture of either 1 or 270 nm. Images were recorded under a Scherzer defocus condition of ~67 nm.

2.3.8 Optical microscopy

To analyze the eggshell microstructure using a polarized light microscope (Nikon LZM 1000), thin eggshell cross sections were prepared by embedding eggshells in epoxy resin (Buehler Epothin), cutting them with a low-speed diamond saw, mounting them on a flat glass slide, and polishing them down to less than 30 µm.

2.3.9 Electron backscatter diffraction

High-resolution EBSD maps of the chicken eggshell microstructure were obtained from thin, polished eggshell cross sections coated with carbon. The EBSD maps were collected over 20

hours using an Auriga Zeiss scanning electron microscope and a 0.3-µm-step size resolution. All EBSD data were collected and analyzed with the AZtec 2.1 software (Oxford Instruments).

2.3.10 2D X-ray diffraction

The microstructure of the eggshell was analyzed on polished eggshell cross sections (0.4 mm thick) with a Bruker D8 VENTURE x-ray single crystal diffractometer equipped with a photon area detector using a molybdenum microsource. The eggshell cross sections were analyzed in transmission mode, with the sample oriented perpendicular to the x-ray beam. A series of frames were registered while rotating the sample in φ angle within the 3° to 10° angular range using 0.3° steps.

2.3.11 Electron tomography

FIB-cut sections approximately 80 nm thick from eggshell and synthetic calcite crystals grown with 5.9 µM OPN were collected on a copper grid. A series of single-axis tilt images was collected with a Tecnai G^2 F20 cryo-S/TEM (FEI) operated at an accelerating voltage of 200 kV equipped with a Gatan UltraScan 4000 4k × 4k digital CCD camera system (model 895). Images were captured at a magnification of 62,000 over a tilt range of from –40° to +60° for the eggshell samples and –50° to +50° for the synthetic calcite crystals (2° increments in both low tilts and high tilts on the 80-nm-thick sections). The resulting images had pixel sizes of 0.19 nm. The images from the tilt series were aligned, filtered and reconstructed into a tomogram using the IMOD software package (*266*). The movies for the raw tilt series and reconstruction were carried out using IMOD, whereas the movies with 3D volume with solid and surface rendering were generated using UCSF Chimera (version 1.10.1).

2.3.12 Nanoindentation hardness testing

Nanoindentation testing was carried out using a Hysitron Ubi III system with 1D transducer mounted to a piezoelectric scanner capable of surface imaging similar to AFM. A Berkovich diamond tip of 50-nm defect radius was used for indentation and surface imaging. Nanoindentation was performed across the eggshell thickness using a matrix consisting of five rows of 83 indents spaced at 50 μm in the lateral direction and 6 μm in the vertical direction. The peak load was 5 mN and the loading/unloading function consisted of 5-s loading, 2-s hold time and 5-s unloading. All indentation tests were carried out in triplicate on three sections from the same eggshell. For nanoindentation tests on the synthetic crystals, cold polymerizing epoxy resin was poured over glass coverslips having attached calcite crystals grown in the absence (control) and presence of OPN (5.9 μM). The glass coverslips were removed after resin hardening, leaving behind a flat surface with exposed, resin-embedded calcite crystals. The crystal surface was prescanned, and images (10 μm x 10 μm area) were acquired, which allowed for the identification of the desired location for indentation. The indentation test was carried out using several partial-unloading steps starting at 0.3 mN peak load, followed by 0.6, 1, 2, and 3 mN to a maximum peak load of 5 mN. A total number of six loading/unloading cycles were used to nanoindent 10 synthetic calcite crystals for each condition. After each indentation test, an image was acquired to determine where the indent was placed and indentation features. A correction for the compliance of the resin was applied using Matlab software, which was based on techniques similar to those carried out by Buchheit and Vogler (*267*) and Leggoe (*268*). Analysis of the load-depth curves obtained from indentation was carried out using the Oliver and Pharr method (*269*). Figure 2.S10 shows typical nanoindentation displacement curves for eggshell and synthetic calcite crystals grown in OPN (5.9 μM).

2.3.13 Immunodetection of OPN in eggshell

Eggshell powder (100 g) was demineralized in 1 M HCl and partially purified by sequential chromatography on CM Sephadex and DEAE-Sephadex resins (*126*). Samples containing total extracted OPN [lane 1, soluble acid extract; lane 2, void volume not retained by CM Sephadex in 0.3 M NaCl and 25 mM Na acetate (pH 4.0)] were separated by SDS- polyacrylamide gel electrophoresis (PAGE) on a 10% gel and transferred to nitrocellulose membrane for immunoblotting, as previously described (*126*), with a rabbit antiserum raised to chicken OPN residues 1 to 11.

For light microscopy immunohistochemistry, eggshells demineralized in EDTA containing 0.1% glutaraldehyde were embedded in paraffin, and 5-μm-thick sections were immunostained for OPN using a rabbit anti-chicken OPN polyclonal antibody (antibody courtesy of L. C. Gerstenfeld, Boston University). Deparaffinized sections were treated with 1% bovine testicular hyaluronidase (Sigma-Aldrich) for 30 min at 37ºC, followed by incubation with anti-OPN antibody diluted 1:200 in 5% normal goat serum/0.2% bovine serum albumin (BSA) in tris-buffered saline (TBS) with 0.01% Tween 20 (TBS-T) [50 mM tris-HCl, 150 mM NaCl, and 0.01% Tween 20 (pH 7.6)]. Sections were washed and incubated with secondary biotinylated goat anti-rabbit immunoglobulin G (Caltag Laboratories, Invitrogen), and then the VECTASTAIN ABC-AP kit (Vector Laboratories) was applied. Optical micrographs were obtained using a Leitz DMRBE (Leica) and a DXC-950 3-CCD camera (Sony). ImageJ software and line scans across the eggshell thickness after immunostaining were used to compare OPN staining intensity in the different shell layers. More specifically, seven staining-intensity profiles, linear plot views from OPN-immunostained eggshell sections that include all eggshell layers (VCL, PL and ML) were used. Each linear plot

shows the local staining intensity along a line drawn perpendicular to the eggshell surface. Profile plots were normalized to the background noise level and averaged.

For immunogold labeling of OPN at the ultrastructural level, eggshell fragments demineralized in EDTA containing 0.1% glutaraldehyde were embedded in LR white resin and sectioned at 80 nm using an ultramicrotome, and grid-mounted sections were incubated with anti-chicken OPN antibody, as described previously (*90*). Immunolabeling reactions were visualized by incubation with the protein A-colloidal gold complex (14-nm gold particles; G. Posthuma, University of Utrecht) followed by conventional staining with uranyl acetate and lead citrate. TEM of these sections was performed as described above.

2.3.14 Synthetic calcite growth in the presence of OPN

Calcite crystals were synthesized by ammonium carbonate diffusion into a 10 mM $CaCl_2$ solution with (or without) added OPN (0.9 and 5.9 μM). Calcite crystallization took place over 2 hours on glass coverslips in small wells contained within a well sealed desiccator previously charged with 1 g of $(NH_4)_2CO_3$ powder. At the end of each experiment, the glass coverslips were removed from solution, gently rinsed with distilled water and ethanol, and air-dried for further characterization. All experiments were performed at least in triplicate.

To assess OPN occlusion within the calcite crystals, the OPN-grown calcite crystals were dissolved in 5% acetic acid for 10 min after removing any surface-bound protein using 1 M NaOH. SDS-PAGE was performed on a 10% gel, and protein/peptide bands were transferred to a polyvinylidene difluoride (PVDF) membrane and blocked using a 5% BSA solution in TBS-T. The PVDF membrane was probed with a rabbit anti-bovine OPN in 5% BSA/TBS-T, followed by visualization using enhanced chemiluminescence reagent.

For microtoming to reveal the interior structure by AFM of the crystals grown with or without OPN, glass coverslips with adherent crystals were embedded in epoxy resin (Epon, Electron Microscopy Sciences) blocks, the glass coverslips were fractured off, and the crystals were sectioned using an ultramicrotome (Leica).

2.3.15 Raman spectroscopy

To investigate the incorporation of OPN inside the calcite crystals, we performed micro-Raman spectroscopy with a Renishaw inVia Raman microscope (Renishaw) equipped with a holographic spectrometer and a Leica DM2500 M optical microscope (Leica Microsystems GmbH). The excitation source was a 514.5-nm argon laser with a laser spot size of approximately 2 μm and an excitation power of 25 mW. The laser was focused through a 50× objective having a numerical aperture of 0.75 on single crystals, as grown on a glass coverslip. Each Raman spectrum was typically acquired for 10 s, and 10 scans were accumulated for each measurement to minimize noise effects. Several spot analyses were taken from each selected area to confirm the spectral reproducibility. For the detection of incorporated OPN into the calcite, all crystals were washed with 1 M NaOH for 2 min to remove surface-bound OPN. The spectra were acquired at room temperature with a spectral resolution of 1 cm^{-1}. Calibration was performed using the 520.5-cm^{-1} band of a silicon wafer as a standard. Renishaw WiRE 3.4 (Windows-based Raman Environment) software was used for Raman data acquisition.

2.3.16 Computational simulation

To predict the binding energies and geometries of the polyaspartate domain of chicken OPN on the obtuse and acute steps of the calcite (104) surface, we used the RosettaSurface algorithm (*270*). The standard algorithm was modified to account for the asymmetry introduced

by step edges and to model a flexible peptide, as outlined in Pacella *et al*. (*270*). We constructed an extended nine-amino acid chicken OPN peptide having the sequence ^{99}DDDDDDDND^{107} using ideal bond lengths and angles (*271*). We constructed a calcite (104) slab using unit cell coordinates from Graf (*272*), and obtuse and acute step edges were created by removing a layer of atoms along the appropriate edge directions. We calculated adsorption energies on both the acute and obtuse step edges using the Talari-2013 energy function (*273*), which includes a linear combination of terms for van der Waals energies, hydrogen bonds, electrostatics, and solvation via an implicit-solvent Gaussian exclusion model. We used energy function parameters from Raiteri *et al*. (*274*) for the atoms of the calcite step edges. For both the acute and obtuse step edges, we generated 20,000 candidate structures and selected the lowest-scoring structures for energetic analysis.

2.3.17 Statistical analysis

Statistical analysis of the samples was performed using a two-tailed Student's *t*-test. Measurements were considered statistically significant when the *P* value was less than 0.05.

2.4 Results and discussion

2.4.1 Nanostructure of avian eggshell (chicken, *G. gallus domesticus*)

Here, systematic atomic force microscopy (AFM) analysis of each eggshell region [shown broadly for orientation purposes at low magnification by scanning electron microscopy (SEM) in Fig. 2.1A] revealed that the outermost vertical crystal layer (VCL), the central palisade layer (PL), and the innermost mammillary layer (ML) all have a fine nanostructure varying in size depending on the layer in which it was observed (Fig. 2.1, B to F). Topographic imaging by AFM operated in the amplitude mode demonstrated an average (±SD) nanostructure size (Feret

diameter) of 30 ± 10 nm in the VCL, 33 ± 10 nm in the upper PL, 59 ± 27nm in the middle PL, 74 ± 36 nm in the lower PL, and 68 ± 26 nm in the ML (Fig. 2.1G). Figure 2.S1 shows the distribution of measured nanostructure size of the eggshell layers as determined from the AFM images from eggs that were not incubated and after 15 days of egg incubation. In addition, Fig. 2.S2 provides the average nanostructure area for all eggshell layers after 15 days of egg incubation. Changes in both nanostructure Feret diameter and area measurements were consistent in their variation between layers. SEM imaging performed on the same layers confirmed the variation in nanostructure size across the eggshell thickness (Fig. 2.1). Within the three sublayers of the PL that we sampled (upper, middle, and lower PL), average nanostructure size (by Feret diameter) continuously increased toward the interior of the shell in this layer, which is the region that forms the main bulk of the shell. In other bird species, previous AFM examination of all layers in the guinea fowl (*Numida meleagris*) and goose (*Anser anser*) eggshell showed a structuring described as "rounded nanogranules" (*275*) such observations in these species are consistent with our findings in the chicken eggshell. In that previous study, nanogranular size was in the range of 50 to 100 nm, values close to the range of sizes that we have measured in the chicken shell layers and similar to those observed in other calcium-carbonate biominerals (*35, 40*). More recently, Rodríguez-Navarro *et al*. (*99*) provided evidence for early nanogranular structuring at the first phase of chicken eggshell deposition where transient, flat, and disk-shaped amorphous calcium carbonate (ACC) forms on the eggshell membranes. However, there has been no detailed description of complete, intact, fully formed chicken eggshell at the nanoscale level to date.

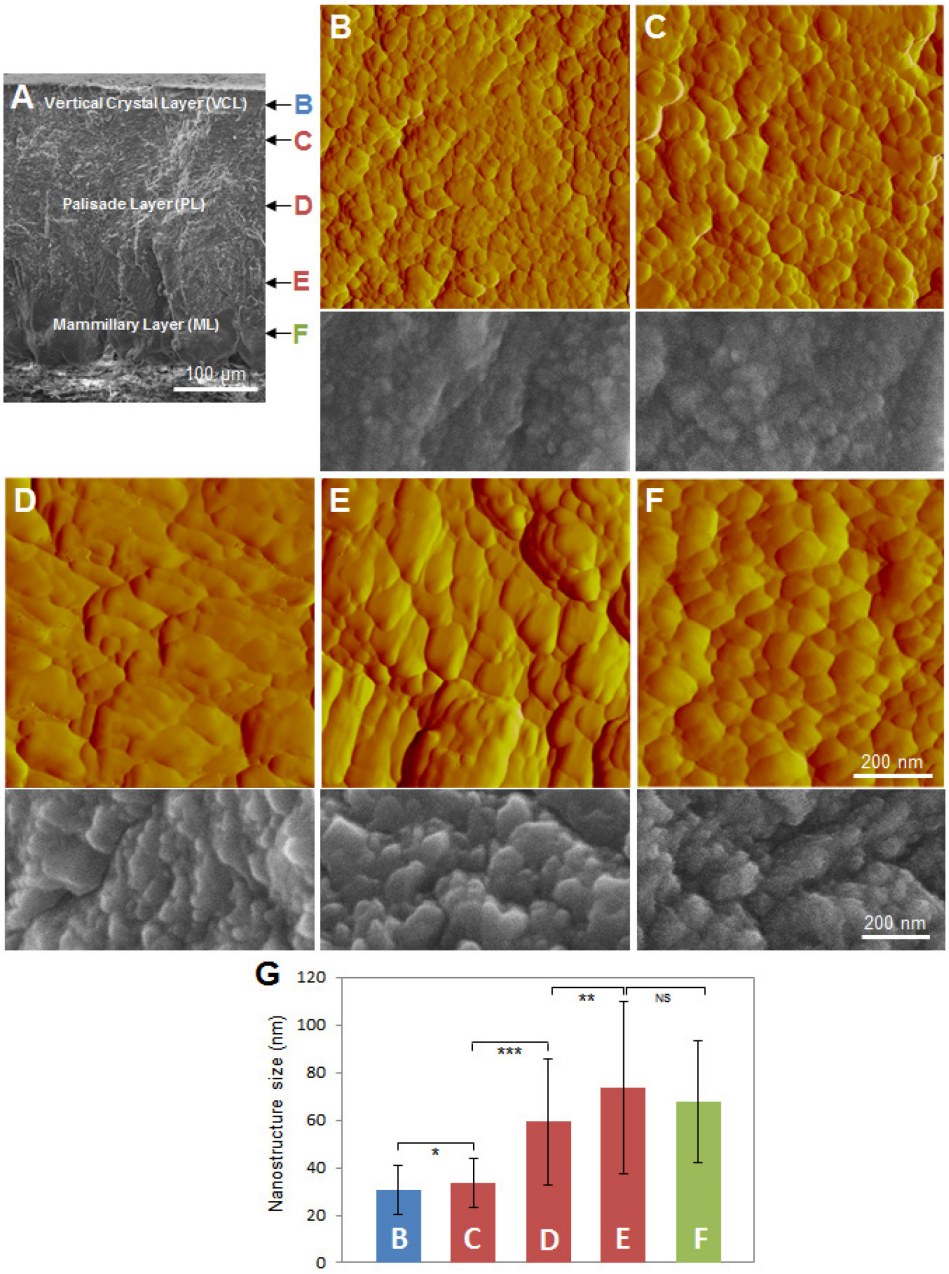

Fig. 2.1 The nanostructure of chicken eggshell (*G. gallus domesticus*). (**A**) SEM microstructure at low magnification, and regional nomenclature, of avian eggshell. (**B** to **F**) AFM (upper panels, with scanning area 800 nm x 800 nm) and SEM (lower panels) images of eggshell nanostructure as observed from the regions indicated in (**A**). (**G**) Histogram of nanostructure size distribution (Feret diameter) in the VCL (**B**), upper PL (**C**), middle PL (**D**), lower PL (**E**) and ML (**F**) layers. Significant difference indicated by brackets (*$P < 0.05$, **$P < 0.01$ and ***$P < 0.001$). No significant difference (NS) ($P > 0.05$) between bars E and F. Values were compared by a two-tailed Student's *t* test.

Crystallographic features of the chicken eggshell include notable internal misalignments observed at the nanoscale in the columnar calcitic crystal units. These internal misalignments presumably occurred, at least in part, from the nonhomogeneous occlusion of abundant organic material (Fig. 2.2A). This was identified broadly by optical microscopy under cross-polarized light, where different degrees of light elimination occur from different microscale regions (Fig. 2.2B). This was further examined with greater resolution by electron backscatter diffraction (EBSD), where diffraction deviations within the calcitic columnar units (here pseudocolored, with deviations appearing as slight color shade differences) reflect the presence of substantial internal misalignments, generated at specific points and extending and propagating during calcite column growth (Fig. 2.2, C to E). Moreover, the 001 pole figure of a columnar calcite unit showed the orientation of *c* axis deviations to be in the range of several degrees (up to 3° and even higher) (Fig. 2.S3A; whereas for a perfect single crystal, all the points in the pole figure would be concentrated in a single spot). EBSD data also show that there is an increase in internal misalignment with increasing column widths (Fig. 2.S3B), which implies that there is an accumulation of defects during eggshell calcitic column growth, further supporting the concept of a nanogranular crystal growth mechanism. Previous EBSD analysis of chicken eggshell and other eggshell species (*275, 276*) has also shown that the PL consists of elongated, well crystallographically ordered single crystals of calcite; however, no evidence of internal misalignments of these elongated crystals was described. Thus, these internal misalignments were further investigated by two-dimensional x-ray diffraction (2D XRD). This confirms that the calcitic columnar units were not perfect single crystals but rather had a high degree of internal misorientations characterized by angular spreading of the diffraction spots (>2.5°) (Fig. 2.2F), producing elongated reflection spots (Fig. 2.2F, inset). In contrast, gently ground geologic calcite

(Iceland spar) – commonly used as a reference, high-quality single-crystal control material for calcite – produced sharp, rounded spots (Fig. 2.2G, inset) with a much smaller angular spread (<0.8°) (Fig. 2.2G).

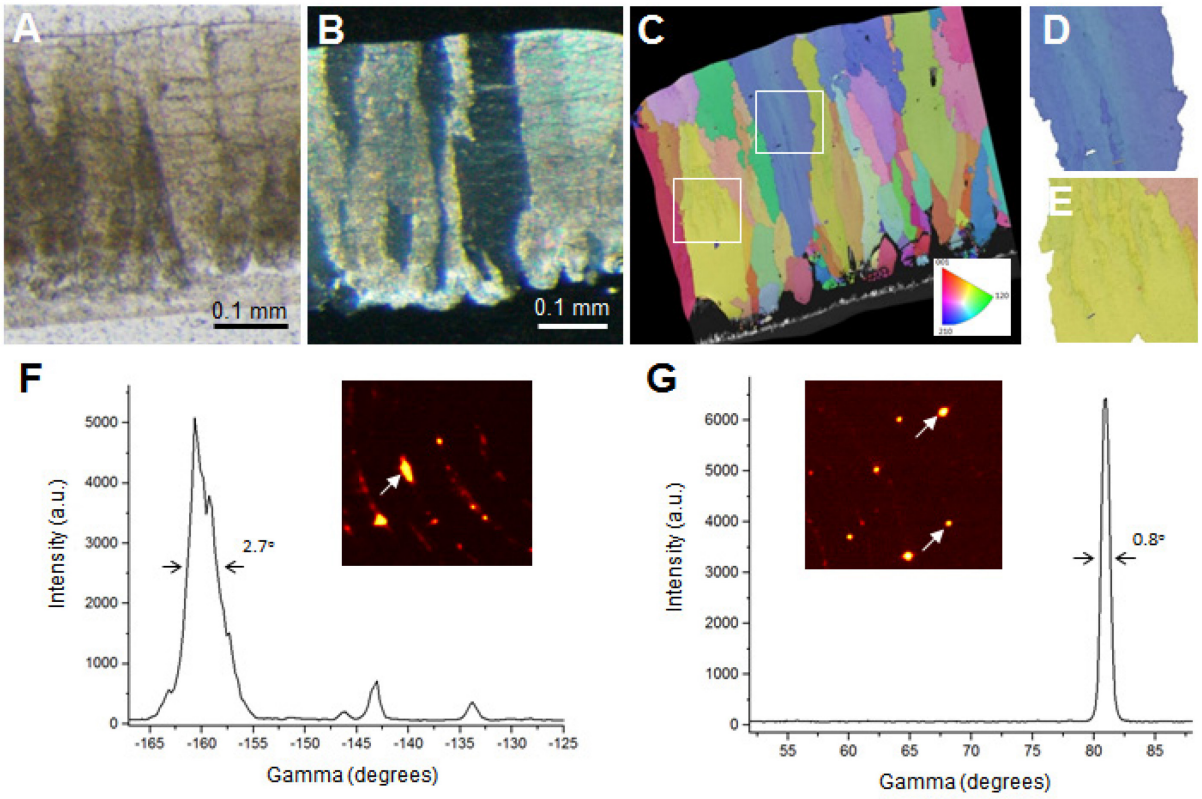

Fig. 2.2 Optical microscopy, EBSD, and 2D XRD of chicken eggshell. (**A**) Thin eggshell cross-section viewed by conventional bright-field light microscopy showing a nonhomogeneous distribution of eggshell material throughout the eggshell layers. (**B**) Thin eggshell cross section [same as in (A)] viewed under cross-polarized light showing multiple, closely packed and well-defined columnar calcite units. (**C**) Crystal orientation map obtained by EBSD of a polished eggshell cross section showing slight internal crystalline misalignments (up to 4º) within the columns as depicted by different pseudocolor shades [see selected boxed areas in (**D**) and (**E**)]. (**F**) 2D XRD of a cross section of an eggshell showing an elongated single-crystal diffraction spot (arrows) and the associated intensity profile of a 104 calcite reflection as a function of the γ angle. Note the widening of the 104 peak due to varying crystallographic orientation within a columnar calcite unit. a.u., arbitrary units. (**G**) 2D XRD of a control powdered Iceland spar calcite crystal showing single-crystal diffraction spots (arrows) and the associated intensity profile of a 104 calcite reflection as a function of the γ angle.

To discard the possibility that these elongated spots were overlapping spots obtained from two or more columnar units, we recorded multiple 2D patterns after rotating the eggshell through 0.3° steps. Together, both the EBSD data and the 2D XRD data – which are complementary techniques – confirm the presence of deviating crystalline subdomains within the calcitic columnar units. These findings describing events occurring within the calcitic eggshell columns emphasize that nanostructure and slight alignment deviations result from a nonclassical crystal growth pathway (*75*).

Eggshell calcite crystals are known to form initially through the deposition of ACC particles that transform directly into calcite while preserving the granular nanostructure of the ACC (*99*). The newly crystallized material can adopt the orientation of previously formed calcite crystals (that is, in the ML) so that the crystallographic orientation is propagated as the columnar calcite crystal units develop by epitaxial nucleation (*277*). Amorphous nanoparticles responsible for the nanostructural morphology of many mineral formations in many organisms can occur as an initial precursor phase stabilized by resident organics, and these can be subsequently crystallized after contact with a crystalline substrate (*2, 69, 77, 278*). In the eggshell, the interplay between organics and mineral precursors likely influences mineralization events leading to internal misalignments.

Given our AFM and SEM findings showing a gradient in nanostructure size across the thickness of the eggshell, we examined the structure of the upper PL in greater detail after using focused-ion beam (FIB) sectioning for further analysis by high-resolution transmission electron microscopy (HRTEM) and electron tomography. Bright-field TEM imaging (Fig. 2.3A) of the prepared FIB section revealed the presence of small mineral nanodomains ranging from 5 to 7 nm in diameter. Nanostructure is also evident at lower TEM magnifications, as shown by both bright-

field (Fig. 2.S4A) and dark-field (Fig. 2.S4B) imaging. Higher-magnification lattice imaging by TEM revealed lattice fringes in these smaller nanodomains, indicating their crystalline nature (Fig. 2.3B). Selected-area electron diffraction (SAED) of these regions showed a coherent orientation of these smaller nanodomains (Fig. 2.3B, inset). Electron tomography of these areas provided 3D reconstructions of this PL nanostructure (Fig. 2.2, C to E, and movies 2.S1 and 2.S2) where abundant and homogeneously dispersed 5- to 7-nm nanodomains were observed to reside within the larger nanostructure initially observed topographically by AFM and SEM (Fig. 2.1C). To confirm this observation using an alternative sample-preparation method, a wedge-polished section of the PL was prepared and thinned using a previously described method (*35*), and similar results were obtained (Fig. 2.S4C). Our work is consistent with observations by Lammie *et al*. (*279*) who used microfocused, small-angle x-ray scattering to report on "nanotexture" variations averaging ~4.5 nm in the PL, a feature that we believe we have now directly visualized and characterized in the present study. In the report of Lammie *et al*., the nanotexture was attributed to voids presumably occupied by globular organic matrix, whereas here, we identify and visualize actual nanostructured, crystalline mineral in 2D and 3D that produces nanostructured texture (and we also present data on protein distribution; see below). Both sets of findings are consistent with the notion that regional variations in organic/protein content (*122*) [acting as activators or inhibitors of mineralization (*90*)], along with relative differences in the amounts, organization, and location of calcite and ACC, all likely contribute to producing the nanostructured texture (*99*).

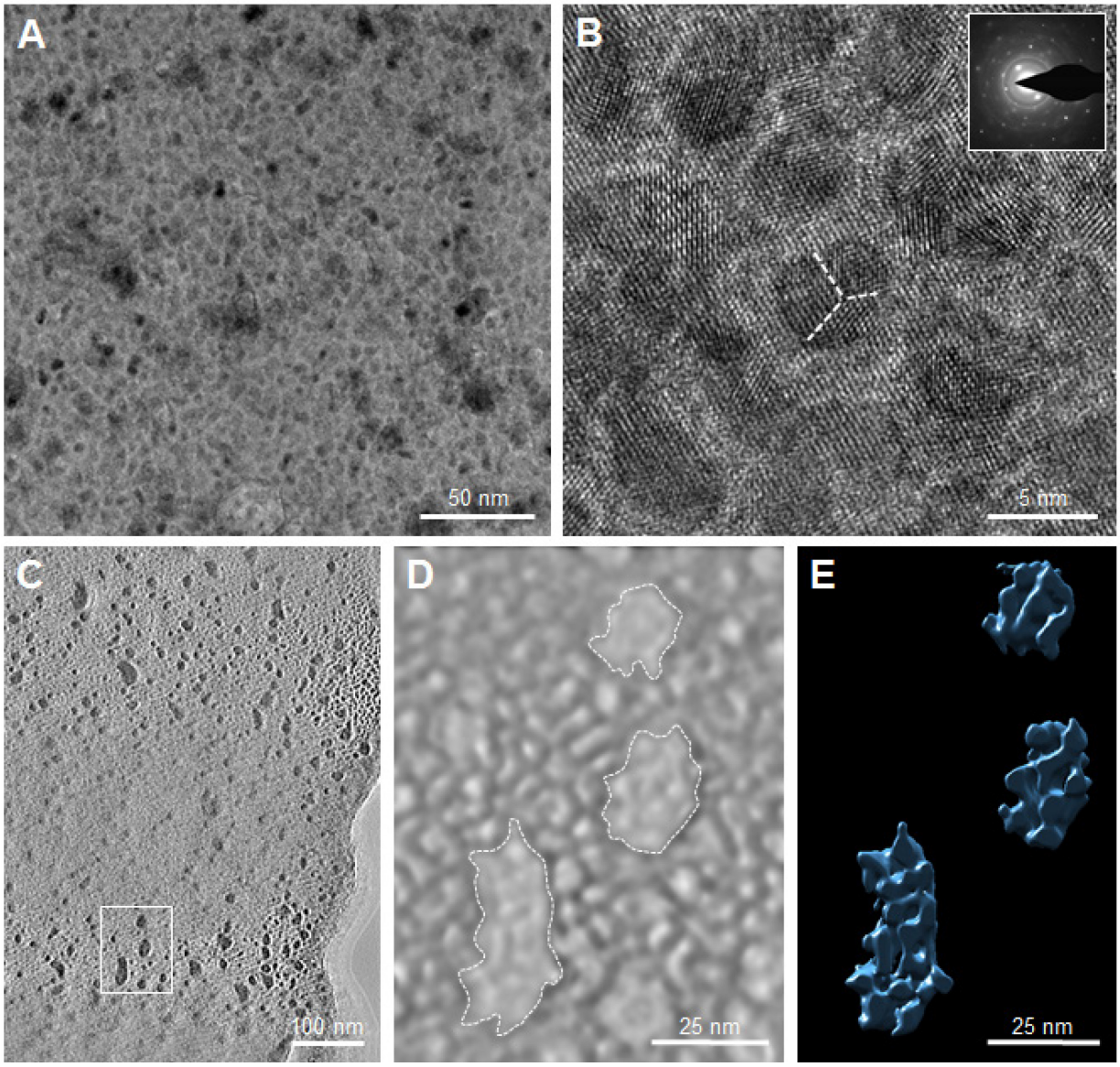

Fig. 2.3 Electron microscopy of a nanodomain substructure in the upper PL. (**A**) Bright-field unstained TEM image of chicken eggshell after FIB sectioning of the PL showing mineral nanodomains with a diameter of 5 to 7 nm. (**B**) HRTEM lattice imaging of the nanodomains, with SAED (inset) showing both a single-crystal diffraction spot pattern and polycrystalline-derived diffraction rings. Evidence for further mineral suborientations within the nanodomains is indicated by the dashed lines. Contrast differences in (A) and (B) presumably result from the relative distributions of a mixture of organic and inorganic (amorphous and crystalline) components. (**C**) Single bright-field TEM image from a tilt series of the nanodomains in the PL. (**D** and **E**) 3D tomographic reconstructions of the same nanodomain region indicated by a box in (C) [solid rendering in (D) and surface rendering in (E)]. The surface rendering in (E) used a threshold that shows only the high-density regions indicated by the dashed lines in (D).

In avian eggs, although the biological benefits of eggshell hierarchical structure (from the nanoscale to the macroscale) for the developing organism (chick) are apparent, the mechanism of nanostructure formation in the chemically crowded (organic and inorganic), and physically confined, milieu is less clear. As a possibility, the formation of pseudoperiodic structures of a uniform size can be explained by the reaction diffusion model, which is also known as the Turing pattern (*280*). Turing patterns are abundant in nature and have remarkable significance in morphogenesis (*281*). The basis of the reaction-diffusion pattern formation is in the competition of two or more oscillating processes having different kinetic constants (for example, short-range activation and long-range inhibition) originating from local instabilities within an initially homogeneous steady-state system (*280*). In the laying hen, uterine fluid bathing the late developing egg (and then the eggshell) is supersaturated with respect to calcite and contains abundant calcium-binding proteins in a metastable system. In this system, heteronucleation events are likely to develop as local instabilities, where the competing processes are the Ca/P ion supply (activation) and the local ion depletion around the growing crystallites (inhibition). Notably, local ion depletion around a growing calcite crystal or a stabilized ACC particle has been demonstrated in the aqueous state in real time, and moreover, the extent of the depletion zone was proportional to mineral particle size (*282*). These reaction-diffusion kinetics could explain the formation of numerous small domains surrounded by a narrow depletion zone or fewer, larger, and more stable domains surrounded by a broader depletion zone, this possibly being a function of ion supply and OPN concentration (and/or other shell proteins) at different stages of eggshell formation (*283*).

2.4.2 OPN and the organic matrix compartment in chicken eggshell

In avian eggshell, OPN was first reported by Pines *et al*. (*145*) who detected strong OPN gene expression by cells specifically in the shell gland that was coincident with eggshell mineralization. In that previous work, immunohistochemistry and light microscopy were used to show that OPN was distributed throughout the shell. Since then, these findings on OPN and eggshell have been confirmed and developed by us and others using a variety of analytical methods (*90, 102, 284*). Here, Fig. 2.4A shows OPN retrieved biochemically from protein extracts of demineralized chicken eggshell. Figure 2.4B demonstrates OPN localization in situ in eggshell by immunohistochemistry at the light microscope level and ultrastructurally by immunogold labeling at the electron microscope level (Fig. 2.4C). Control incubations performed omitting the primary antibody showed only minor background staining. Regional variations in the concentration of OPN are apparent [Fig. 2.4, B (brackets) and C (arrows)]; note that the demineralization procedure itself imparts substantial alterations to the localization pattern as the mineral dissolves and the organic matrix network partially collapses. Qualitatively, by immunostaining, OPN was most abundant in the VCL/PL and least abundant in the ML. Semiquantification of this immunolabeling using intensity-profile, linear plot views obtained from immunostained eggshell sections using ImageJ (Fig. 2.S5A) showed consistently high concentration of OPN in the outermost VCL layer, followed by a steady decline in OPN content toward the ML layer (Fig. 2.S5B). These results are in agreement with quantitative proteomics revealing that eggshell OPN levels are highest during development of the PL (*285*). Other proteomic data from eggshells obtained at various stages of formation, as retrieved from the shell gland of laying hens, have revealed an extensive protein incorporation profile at all stages of shell formation (*122, 259*). Proteins (and other organics) that constitute the organic matrix of the shell interlace extensively, but variably, throughout all regions

of the mineralized shell. How this cohabitation with calcium-carbonate mineral occurs remains poorly understood – a compartmental feature particularly surprising given the highly ordered (albeit with some misalignment) calcite mineral organization.

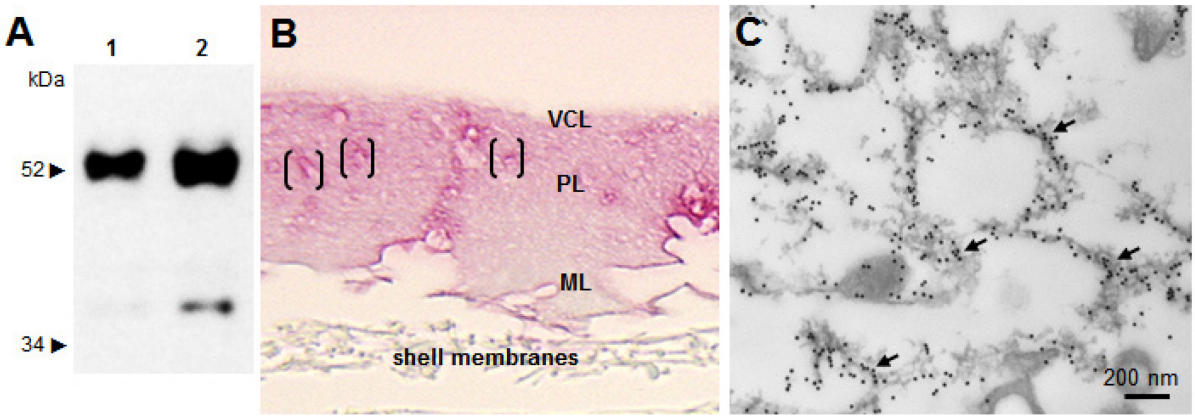

Fig. 2.4 OPN in chicken eggshell. (**A**) Immunoblotting for chicken eggshell OPN. Lane 1, total soluble protein extract from decalcified eggshell (1 M HCl); lane 2, acidic eggshell matrix proteins, not retained on CM Sephadex (see Methods). (**B**) Immunohistochemistry (pink) for OPN protein showing its incorporation and distribution throughout the full thickness of the eggshell (decalcified here). Brackets indicate areas in outermost PL with concentrated OPN amounts. (**C**) Immunogold labeling for OPN (arrows) and TEM showing the association of OPN with a lacy network of organic matrix dispersed throughout the PL of the eggshell. (B) and (C) are from demineralized shell samples, resulting in artifactual partial collapse of an organic matrix structure.

We postulated that regional and local variations in OPN content (and likely other regulatory molecules in the shell) may lead to the differences we observed in nanostructure size that changed from one layer to another. From this, we also surmised that the sites we observed having the 5- to 7-nm nanodomains may contain the highest level of mineralization-inhibiting matrix molecules such as OPN. At these sites, the proteins may exert nanodomain control by binding/sequestering mineral ions and possibly acting to stabilize an ACC precursor phase and by binding to crystallographic faces of calcite. It is also likely that acidic organic matrix molecules fill the

internanosubunit volumes that are not crystallized, all of which may contribute to imaging contrast differences observed by TEM that provide visual evidence for nanostructure.

2.4.3 Controlling the nanostructure of synthetic calcite using OPN

To investigate the possibility that OPN might be able to induce nanostructure in synthetic calcium carbonate, calcite crystals were grown in the presence of OPN. After microtoming to expose the interior of the grown synthetic calcite crystals, control calcite (grown without added protein) showed no internal nanostructure as observed by AFM (Fig. 2.5A). The same analysis performed on similarly microtome-cut calcite showed an internal nanostructure when calcite was grown in either low (0.9 μM) or high (5.9 μM) OPN concentration (Fig. 2.5, B and C, respectively). The average (±SD) size (Feret diameter) of the nanostructure induced in the presence of low and high OPN concentration was 77 ± 27 nm and 29 ± 7 nm, respectively (Fig. 2.S6A). Nanostructure distribution from the synthetic crystals grown with 0.9 or 5.9 μM OPN is shown in Fig. 2.S6 (B and C, respectively). Consistent changes in area measurements for OPN concentration were also observed (Fig. 2.S6D). These nanostructural observations, together with the measured change in nanostructure size after growth in different OPN concentrations, demonstrate not only nanostructure induction but also control of nanostructure size by OPN (increasing concentration produces smaller nanostructure size). HRTEM lattice imaging of a FIB-cut section of a synthetic calcite crystal grown with 5.9 μM OPN (Fig. 2.S7A) confirmed the existence of a nanostructure, with the nanocrystals having a significant preferential crystallographic orientation as shown by SAED (Fig. 2.S7B). Notably, the measured nanostructure size from the synthetic calcite grown at the low OPN concentration was similar to the size found in the inner region of the eggshell PL, whereas the higher OPN concentration produced a nanostructure size similar to the outer part of

the eggshell in the VCL. TEM of control calcite crystals (grown without added OPN) showed no internal nanostructure (Fig. 2.S8). Consistent with this, and as previously shown by others, soluble acidic organic matrix extracted from nacre induces in vitro the formation of nanostructured synthetic calcite crystals (*38*), and Xu *et al*. (*286*) observed a nanocrystalline internal structure and mesoscopic behavior after growing calcite in the presence of copolymers.

As was performed on eggshell, we examined the structure of the synthetic crystals in greater detail after FIB sectioning and HRTEM and electron tomography. Bright-field TEM imaging and tilt-series electron tomography (Fig. 2.S9) showed a homogeneous nanostructure in the crystals having a network of small, high-density mineral nanodomains (movies 2.S3 and 2.S4).

As shown in previous studies (*90, 287*), the significant alterations seen by SEM in external calcite rhombohedral morphology was OPN concentration-dependent (insets in Fig. 2.5, A to C). Eggshell matrix constituents and uterine fluid extracts and proteins have been previously used to modify calcite growth in vitro. SEM observations of calcite crystals precipitated in the presence of chicken uterine fluid (containing OPN and many other proteins) collected from laying hens at different stages of eggshell formation showed quasi-spherical or rodlike aggregations of calcite microcrystals elongated along the *c* axis (*91*). Although some effects of OPN have been noted in modifying external calcite rhombohedral morphology (*90*), to date, no one has observed that an eggshell matrix protein induces internal nanostructure in calcite.

To verify that our nanostructure observations from the interior regions of the synthetic calcite crystals grown in the presence of OPN were indeed attributable to incorporated protein, we recovered the added OPN from the interior of the crystals. This was carried out by first removing surface-bound protein using NaOH and then dissolving the calcite to make a protein extract. We submitted this extract to gel electrophoresis, from which we identified recovered OPN by

immunoblotting and compared it to the state of the originally added protein (Fig. 2.5D). From the dissolved calcite, we obtained characteristic OPN peptide bands arising from originally occluded, and then retrieved, OPN. Compared to the state of the OPN at the time of addition to the growth system, the retrieved protein extract showed no remaining full-length OPN but only the two smaller OPN peptide bands. This perhaps reflects autocatalytic cleavage of OPN during the occlusion process, or site-specific hydrolysis under the basic conditions that can arise in slow-diffusion systems (such as the one we used), or selective occlusion of OPN fragments.

Further confirmation that OPN was occluded into the calcite to generate a nanostructure was obtained from micro-Raman spectroscopy, which showed a broad spectral peak between 2850 cm^{-1} and 3000 cm^{-1} for the two OPN concentrations (Fig. 2.5E). This peak corresponds to C-H vibrational stretching (*288*) observed for proteins, with the peak intensity reflecting the amount of added OPN. Together, these data indicate that OPN occlusion within calcite is part of a process that contributes to the development of calcium-carbonate nanostructures, similar to what we observed in the eggshell.

The influence of OPN on inducing nanostructure and modulating the dimensions of this nanostructure, and its incorporation into calcite, can be largely attributed to its strong binding to mineral occurring through the acidic peptide stretches in its primary amino acid sequence (*209*). We thus computationally modeled, using RosettaSurface (*270*), docking of the highly acidic polyaspartate sequence found in chicken OPN (^{99}DDDDDDDND^{107}) to acute and obtuse growth steps of calcite (Fig. 2.5F). The binding energies to these two calcite surfaces were equal, being approximately –14 kcal/mol. The fact that these two values are the same indicates that there is no preferred selection between the two steps. This conclusion is supported by the observation of the

generally rounded morphology of the nanostructure as shown by AFM imaging (Fig. 2.5, B and C).

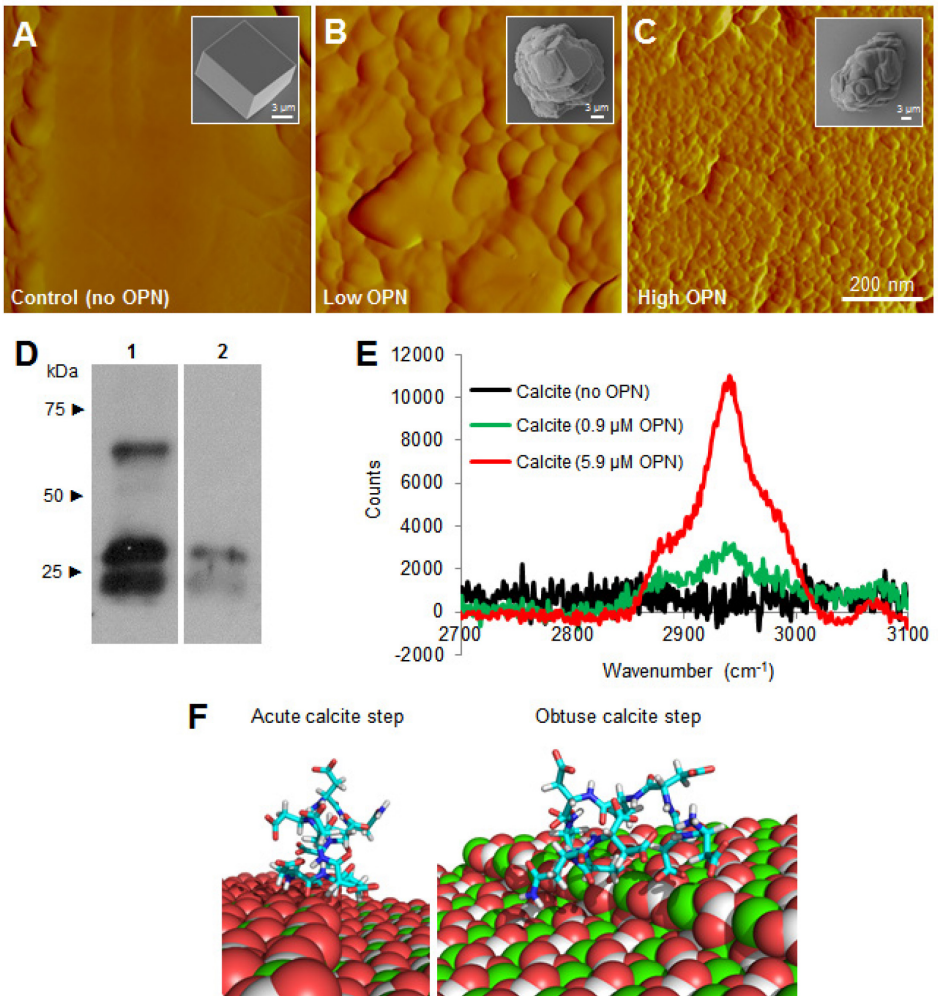

Fig. 2.5 Nanostructure induced by OPN and protein occlusion within calcite. (**A** to **C**) AFM images of the interior of microtome-cut calcite crystals showing no nanostructure in the absence of OPN (A) but visible nanostructure after growth in the presence of 0.9 μM OPN (B) or 5.9 μM OPN (C) (scanning area, 800 nm x 800 nm). Insets in (A) to (C) show typical SEM images of calcite crystals from which AFM images were obtained after microtoming to expose the interior structure. (**D**) Immunoblotting after gel electrophoresis of dissolved crystals showing retrieved OPN and degraded OPN fragments (lane 1, OPN protein alone; lane 2, dissolved crystals growing in the presence of 5.9 μM). (**E**) Micro-Raman spectra from grown crystals, demonstrating a C-H protein peak. (**F**) Computationally simulated (RosettaSurface) conformer docking of the polyaspartate domain (^{99}DDDDDDDND^{107}) of chicken OPN on the obtuse and acute step of calcite (binding energy, approximately –14 kcal/mol for both cases). Calcite atoms: Ca, green; C, grey/white; O, red.

2.4.4 Functional properties of the nanostructured eggshell

The hardness and elastic modulus behavior of the nanostructured layers of chicken eggshell was investigated by observing their nanoindentation characteristics. Nanoindentation strikes, across the full cross-sectional thickness of fractured eggshell, revealed a gradually decreasing hardness and elastic modulus from the outermost region of the eggshell (the VCL) toward the central region of the PL (Fig. 2.6, A and B). Further nanoindenting toward the interior side of the shell showed increasing hardness and elastic modulus values toward the innermost ML (Fig. 2.6, A and B). In correlating the hardness measurements with nanostructure size, the highest hardness values were obtained from the outermost VCL and upper PL where the smallest nanostructure was demonstrated (Fig. 2.6C). The hardness in nanocrystalline materials, including hard ceramics, is known to inversely increase with a decrease in subunit size (up to a certain critical value), which is a well-known feature of the Hall-Petch relationship. Here, the hardness of materials (H) is dependent on crystal size (d), and is shown by the empirical Hall-Petch equation $H = H_0 + k_H d^{-1/2}$, where H_0 is the hardness of a single crystal and k_H is a material-specific constant (*289*). For approximately the outermost half of the shell, our results follow the Hall-Petch model, indicating that eggshell nanostructure, in conjunction with its composition and microarchitecture (*103*), are factors that determines its hardness. In addition, high elastic modulus values were obtained in the outer eggshell layers having the smallest observed nanostructure (VCL and upper PL) and the highest amount of protein including OPN. Similar to other mineralized tissues, it is expected that the tension-shear model (Jaeger-Fratzl model) applies in biocomposites where the mineral carries the tensile load, whereas the protein transfers the load between the nanomineral units via shear (*58*). Moving from the middle PL into the ML, the inverse correlation of decreasing hardness and elastic modulus did not continue to hold with increasing nanostructure size; for this, we have no

explanation other than there potentially being different compositions or less structural homogeneity in these regions, as has been described previously (*90*).

Measurements at the nanoscale of the mechanical properties and their relationship with the size of nanogranular structure complement previous observations on the influence of the structural organization of eggshell at the microscale on its mechanical properties (*103, 290*). In these studies, an increase in the size of calcitic columnar crystal units in eggshell laid by older hens correlated with a significant reduction in eggshell breaking strength. The abrupt decrease of eggshell mechanical properties after 1 year of laying is a substantial problem for the egg industry which is actively looking for strategies to extend the laying period of hens while maintaining eggshell quality. Overall, previous and new data show that the mechanical properties of eggshell are controlled by its structural organization over different length scales. Given this context, we assessed by nanoindentation the mechanical properties of the synthetic calcite crystals grown with OPN (5.9 μM). The hardness of these calcite crystals increased significantly with the occlusion of OPN, which induced nanostructure (Fig. 2.5, A to C, and Figs. 2.S8 and 2.S9). The average (±SD) hardness value of the calcite grown without OPN was 2.02 ± 0.04 GPa, whereas the average (±SD) hardness of the calcite crystals grown with added OPN was 2.79 ± 0.1 GPa (Fig. 2.6D).

Bones, teeth and shells of all types have remarkable mechanical properties, as conferred by their composite hybrid structure of mineral particles/platelets dispersed within an extended organic framework commonly called the extracellular matrix. In many cases, these biocomposites exhibit levels of hierarchical structure ranging from the nanoscale to the macroscale (*58*), architectures that typically provide toughness to biomineralized structures (*291, 292*). In essentially all cases, nanometer-length-scale organized structures are important in providing these mechanical properties (*58*), a feature that currently drives bioinspired materials development

(*293*). The Griffith criterion describing crack propagation in materials in terms of length scale defines a critical limit below which energy considerations will not allow a crack to propagate further (*230*). For biocomposites (where nanostructure is commonplace), this is considered to ensure optimum fracture strength and maximum tolerance of flaws (*58*). In this case, the Griffith criterion applied to intercalated organics between mineral domains at the nanoscale would describe a distribution of stresses across larger volumes; this would provide a toughening mechanism for function that acts to decrease crack propagation in organismal biomineralized structures. In nacre, as another example, Wang *et al*. (*294*) reported that cracks deflect and propagate within the nanostructured tablets along the location of occluded organics, following an undulating intergranular crack path. Together, these and other studies show that nanostructure and the incorporation of organics (*295*) lead to enhanced mechanical properties for biomineralized structures.

Apart from contributing to mechanical properties, we hypothesized that the increased surface area afforded by the small mineral nanodomains in the inner layers of the eggshell makes more surface area available for the mineral dissolution – a process that provides calcium to the developing chick embryo primarily for skeletal growth. In principle, such a process would allow retention of overall shell layer structure but with some thinning and compromised strength, a feature ultimately necessary for successful chick pipping to puncture/break the shell during hatching. To explore this possibility, we examined the shell nanostructure of fertilized eggs incubated for 15 days (chick hatching typically occurs around 21 days of incubation). AFM of these shells revealed that, although the VCL nanostructure remained unaffected [30 ± 7 (SD) nm] as we surmised (Fig. 2.6E), there was a significant decrease in nanostructure size (Feret diameters) from this physiologic mineral dissolution in the innermost region of the PL [36 ± 10 (SD) nm]

(Fig. 2.6F) and in the ML [36 ± 11 (SD) nm] (Fig. 2.6G), and changes in nanostructure area measurements of the same regions were consistent with the changes in diameter values (Fig. 2.S2, B to D). At the microscale and macroscale, inner shell dissolution during egg incubation occurs in the mammillae and at the base plate below the tips of the mammillary knobs, the latter dissolution resulting in detachment of the shell from the outer eggshell membranes (*264*). Moreover, at the ultrastructural and microstructural level, the inner part of the eggshell (ML) consists of much smaller (narrower) calcite crystals compared to the bulk eggshell material that consists of larger (wider) columnar calcite units (*296*); the organization at this level could be a determinant for dissolution of the eggshell.

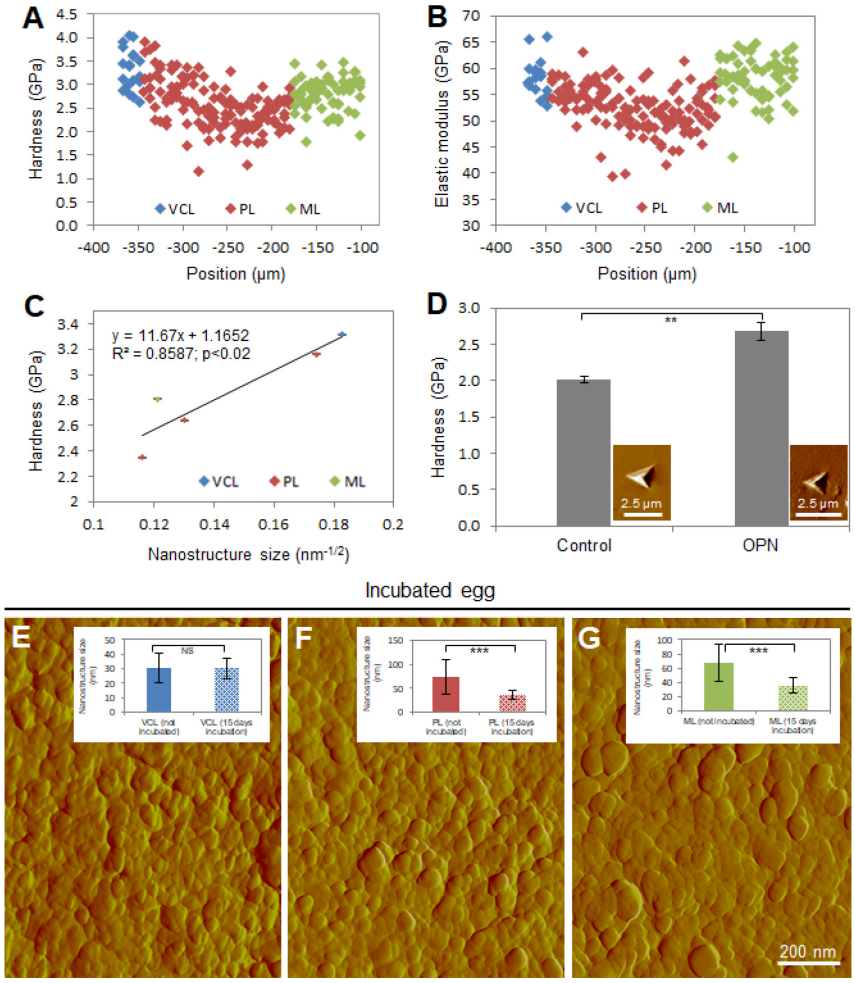

Fig. 2.6 Mechanical testing by nanoindentation of eggshell and synthetic calcite crystals and effects of physiologic eggshell dissolution. (**A**) Hardness distribution across the eggshell layers. (**B**) Elastic modulus distribution across the eggshell layers. (**C**) Hall-Petch plot of average hardness versus nanostructure size distribution in the eggshell layers. (**D**) Hardness values from synthetic calcite crystals grown in the absence (control) and presence of OPN (5.9 μM). Insets show typical images of residual indents on the specimen surface. Significant difference is indicated by a bracket (**$P < 0.01$). (**E** to **G**) AFM images of nanostructured VCL (E), lower PL (F), and ML (G) eggshell layers from a fertilized egg incubated for 15 days (scanning area, 1.2 μm x 1.2 μm). Insets show nanostructure size distribution of the different eggshell layers, comparing eggs that were not incubated to incubated eggs. No significant difference ($P > 0.05$) is observed between VCLs, whereas a significant difference (***$P < 0.001$) in size exists between the two groups for the PL and the ML. Values were compared by a two-paired Student's *t* test.

Related to this physiologic eggshell dissolution, in terms of the stability of nanocrystals in aqueous environments, where nanostructure size is very small as in the VCL, crystallite size can be preserved when that size correlates with a certain critical value of undersaturation conditions for a particular mineral (*297*). Under these critical conditions, the dissolution rate of the nanocrystallites can be self-inhibited, in contrast to the Ostwald-Freundlich scenario, which usually assumes that smaller particles are dissolved faster because of their higher solubility. Thus, the smallest nanostructure observed by AFM, appearing in the outermost region of the VCL, can partly explain eggshell resistance to dissolution under external aqueous (including environmental) conditions. In addition, occluded pericrystal organic material accumulating at nanograin boundaries can reduce their solubility and control the dissolution of biocomposites (*298*). Consequently, nanostructured biominerals can even remain stable in undersaturated biological and other aqueous fluids and remain comparatively resistant to dissolution phenomena (*297*), which is clearly an evolutionary advantage for humid/wet, egg-incubation conditions.

Together, the information we report here on the functional properties of nanostructured eggshell provides insight into biomineralization mechanisms and eggshell mechanical properties. Moreover, the findings also potentially serve to inform rational designs for novel, bioinspired functional nanomaterials having desirable and tunable unique properties.

2.5 Conclusions

Here, the nanostructure of mineralized avian (chicken) eggshell *G. gallus domesticus* is described across the entire thickness of the shell for each of its major layers. Nanostructure size is different for each of the layers, presumably arising from the effects on mineralization of incorporated organic molecules. Using one such shell-resident biomolecule, the protein OPN, a synthetic calcite nanostructure can be induced, and its size can be controlled by the addition of this inhibitory, mineral-binding shell protein; higher concentrations of OPN lead to a smaller nanostructure size. In the outer half of the eggshell, decreased nanostructure size generally correlates with increased shell hardness, an observation reproduced by growing synthetic calcite crystals in the presence of OPN. In fertilized incubated eggs, partial dissolution of calcitic nanostructure occurs in the inner region of the shell, providing calcium for the growing chick embryo skeleton and resulting in the shell weakening required for hatching. These findings provide insight into chicken eggshell formation, mechanical function, and dissolution, and they can be used to inform design concepts for synthetic nanocomposites having novel properties.

2.6 Acknowledgements

We are grateful to D. Liu, L. Mongeon, L. Malynowsky, Q. Wu, and K. Sears for assistance with TEM and FIB work. We also thank Y. Nakano for her help with the immunohistochemistry experiments, E. Sørensen and Arla Foods for donating OPN protein, L. C. Gernstenfeld for the OPN antibody, A. Ryan for providing eggshell samples, and N. Reznikov for her thoughts on Turing patterns. The assistance of A. Gonzalez and J. Romero (Centro de Instrumentacion Cientifica Universidad de Granada) for the 2D XRD and EBSD analyses is acknowledged. We thank A. Saeed for the use of the Matlab code used for analysis of partial unloading data and compliance corrections. Electron microscopy was performed at McGill University's Facility for Electron Microscopy Research. **Funding:** This work was supported by a grant from the Canadian Institutes of Health Research (no. MOP-142330) and the Natural Sciences and Engineering Research Council of Canada (NSERC; no. RGPIN-2016-05031) to M.D.M., an NSERC (no. RGPIN-2016-04410) Discovery grant to M.T.H., a Spanish Government grant (CGL2015-64683-P) to A.B.R.-N., an Emmy Noether research grant from the German Research Foundation (no. WO1712/3-1) to S.E.W., and an NSF grant (NSF BMAT; no. 1507736) to J.J.G. M.D.M. is a member of the Fonds de Recherche Quebec–Sante Network for Oral and Bone Health Research and the McGill Centre for Bone and Periodontal Research. **Author contributions:** D.A., W.J., and M.D.M. designed the overall experimental and analytical plan and drafted the initial manuscript. D.A. was involved in all experimental and analytical work. W.J. contributed to the AFM analysis. D.G., A.S., and R.R.C. contributed to the nanoindentation tests. H.V., K.B., and K.H.B. contributed to the TEM/tomography analyses. A.B.R.-N. contributed to the EBSD and 2D XRD data. M.T.H. provided the OPN extraction biochemical data. C.F.B. and S.E.W. prepared the wedge-polished sections. M.S.P. and J.J.G. performed the computational simulations. All authors

analyzed and interpreted the data and participated in the writing and editing of the manuscript. M.D.M. provided overall supervision of the research. **Competing interests:** The authors declare that they have no competing interests. **Data and materials availability:** All data needed to evaluate the conclusions in the paper are present in the paper and/or the Supplementary Materials. Additional data related to this paper may be requested from the authors.

2.7 Supplementary materials

Fig. 2.S1 Distribution of measured eggshell nanostructures by AFM.

Fig. 2.S2 Eggshell nanostructure area measurements.

Fig. 2.S3 Internal nanocrystal misalignments in the PL of chicken eggshell.

Fig. 2.S4 TEM showing eggshell nanostructure.

Fig. 2.S5 Semiquantification of OPN immunostaining across the eggshell thickness.

Fig. 2.S6 Effect of OPN on nanostructure size in synthetic calcite crystals.

Fig. 2.S7 OPN induces nanostructure in synthetic calcite crystals.

Fig. 2.S8 Absence of nanostructure in synthetic control calcite crystal (no added OPN).

Fig. 2.S9 Electron microscopy of a FIB section showing nanostructure in a synthetic calcite crystal grown with OPN (5.9 μM).

Fig. 2.S10 Nanoindentation displacement curves for eggshell and synthetic calcite crystals grown in OPN (5.9 μM).

Movie 2.S1 Three-dimensional reconstruction from a tilt series of the upper PL of avian chicken eggshell *G. gallus domesticus*.

Movie 2.S2 Three-dimensional reconstruction of nanodomains found in the upper PL of the eggshell.

Movie 2.S3 Three-dimensional reconstruction from a tilt series of the synthetic calcite crystal grown with 5.9 μM OPN.

Movie 2.S4 Three-dimensional reconstruction of a nanostructured region found in the synthetic calcite crystal grown with 5.9 μM OPN.

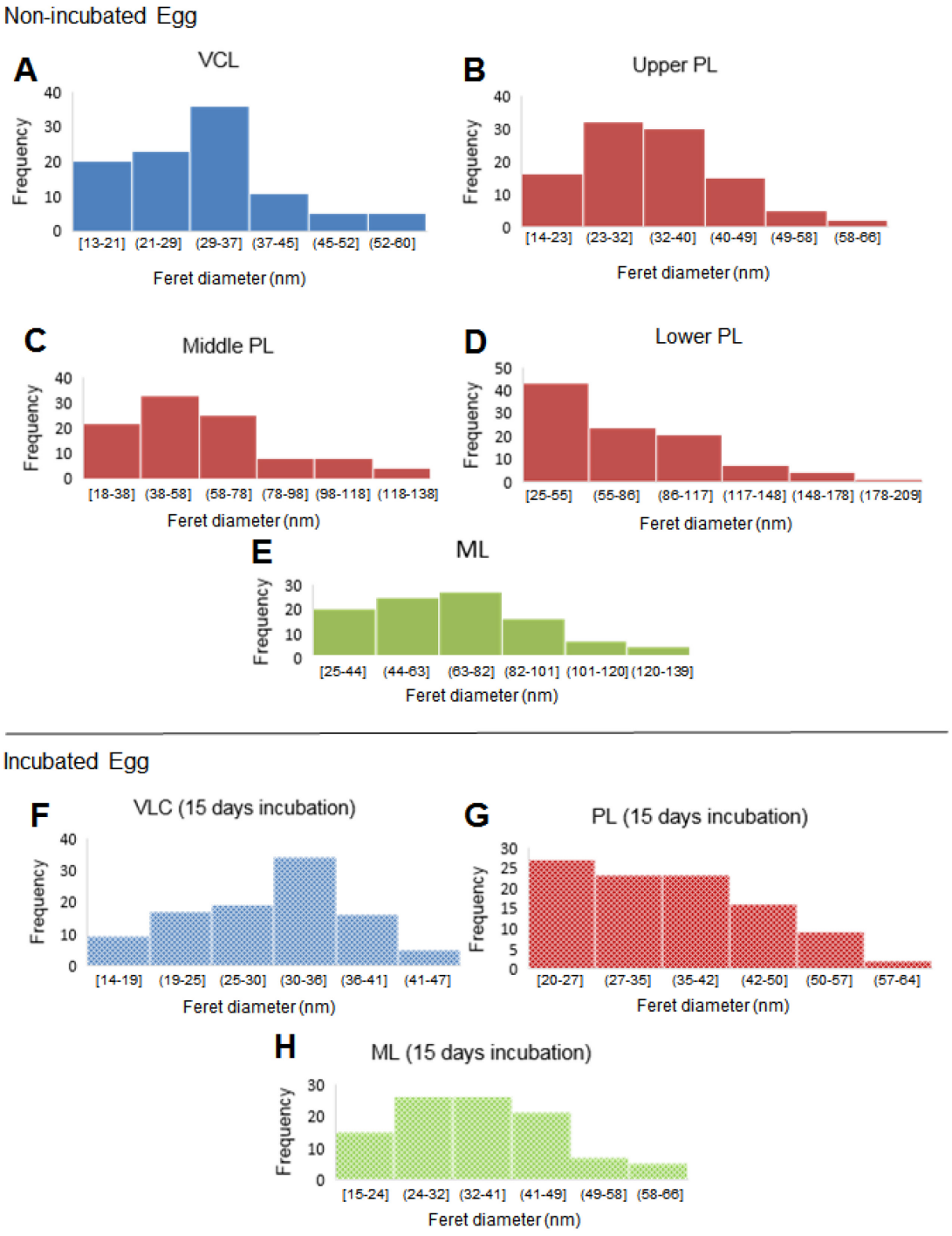

Fig. 2.S1 Distribution of measured eggshell nanostructures by AFM. (**A-E**) Distribution of nanostructure size from VCL (A), upper PL (B), middle PL (C), lower PL (D) and ML (E) layers of the eggshell. (**F-H**) Distribution of nanostructure size from VCL (F), PL (G) and ML (H) of an egg incubated for 15 days.

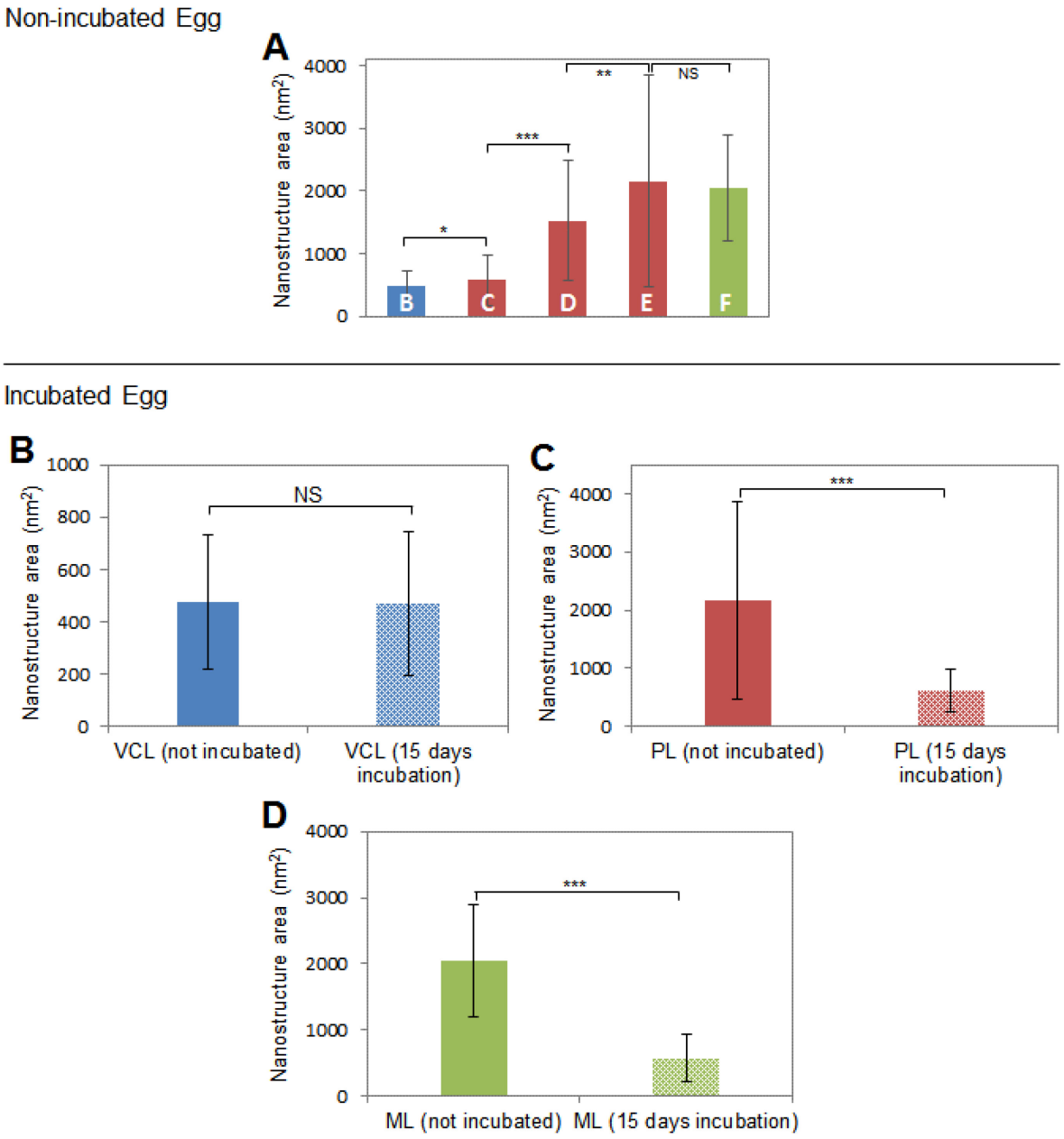

Fig. 2.S2 Eggshell nanostructure area measurements. (**A**) Histogram of nanostructure area distribution in the VCL (**B**), upper PL (**C**), middle PL (**D**), lower PL (**E**) and ML (**F**) (see Fig. 2.1A for identification of these layers). Significant difference indicated by brackets (*$P < 0.05$, **$P < 0.01$ and ***$P < 0.001$). No significant difference (NS) ($P > 0.05$) between bars E and F. Nanostructure area distribution in eggshell VCL (B), PL (C) and ML (D) comparing eggs that were not incubated to incubated eggs. No significant difference ($P > 0.05$) is observed between vertical crystal layers, whereas a significant difference (***$P < 0.001$) in area exists between the two groups for the palisade layer, and for the mammillary layer. Values were compared by a two-paired Student's *t* test.

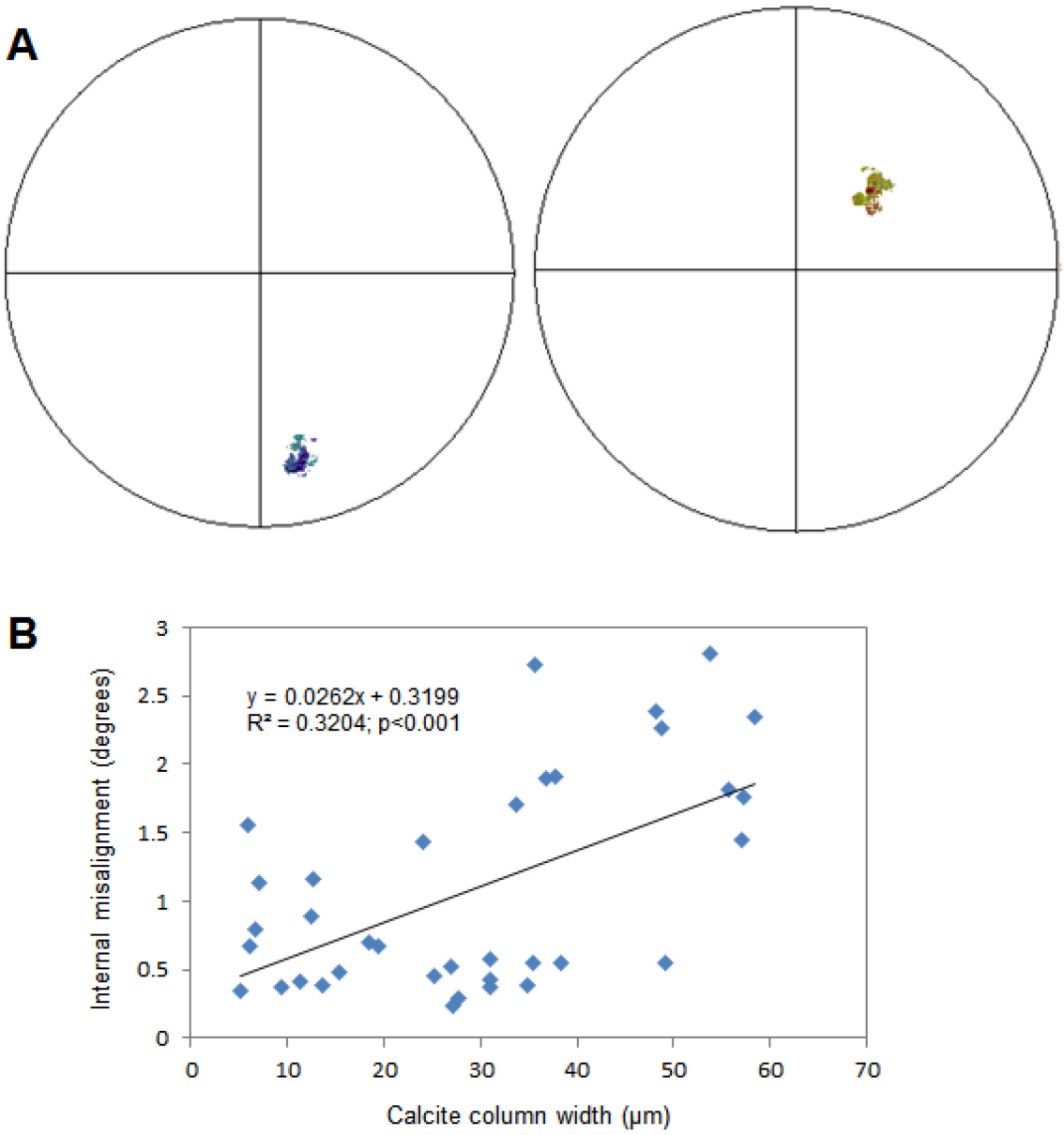

Fig. 2.S3 Internal nanocrystal misalignments in the PL of chicken eggshell. (**A**) 001 pole figure of two columnar calcite units showing a notable scattering of the *c* axis within each column. The orientation of the *c* axis (shown in the same pseudocolor scheme as in the EBSD maps in Fig. 2.2C-E) changes within a range of several degrees. (**B**) Misalignment of internal nanocrystals within a calcite column in the palisade layer as a function of size of the columns. The data indicate that there is an accumulation of defects occurring during crystal/column growth that produces an increase in the observed internal misalignment of nanocrystalline domains.

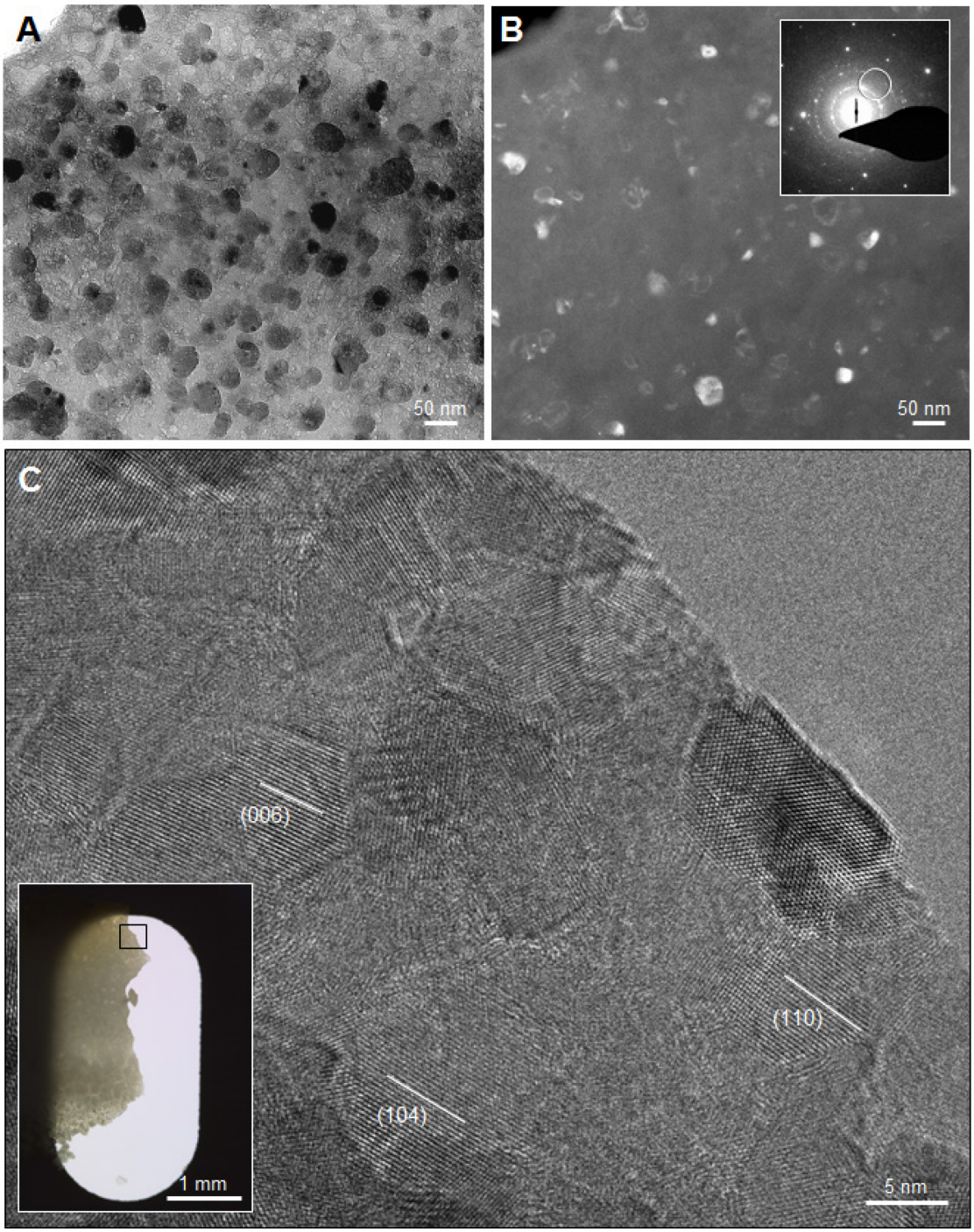

Fig. 2.S4 TEM showing eggshell nanostructure. (**A**) Bright-field and (**B**) dark-field TEM images after FIB sectioning of eggshell. Inset shows the SAED area from where the dark-field image was taken. (**C**) Mechanically prepared and polished chicken eggshell wedge cross section (inset, low-magnification grid-mounted) showing the presence of 5-7 nm nanodomains with various indexed crystallographic orientations.

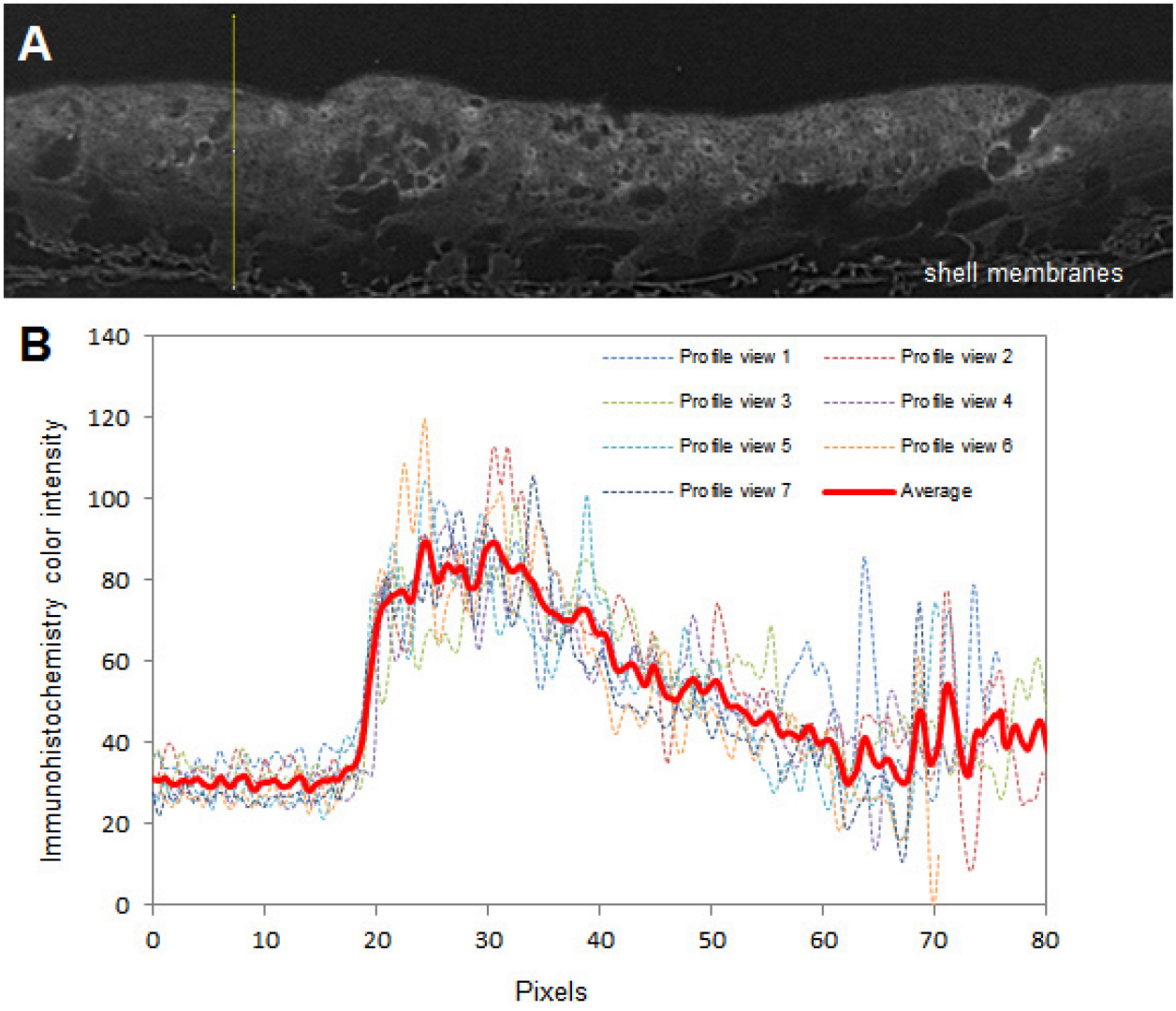

Fig. 2.S5 Semiquantification of OPN immunostaining across the eggshell thickness. (**A**) Typical profile view (vertical yellow line) from an inverted image created with ImageJ software from a digital image taken of OPN immunostaining of a paraffin section from a decalcified eggshell. (**B**) Plot of seven intensity profile views for OPN staining, with the average OPN intensity profile view shown in red.

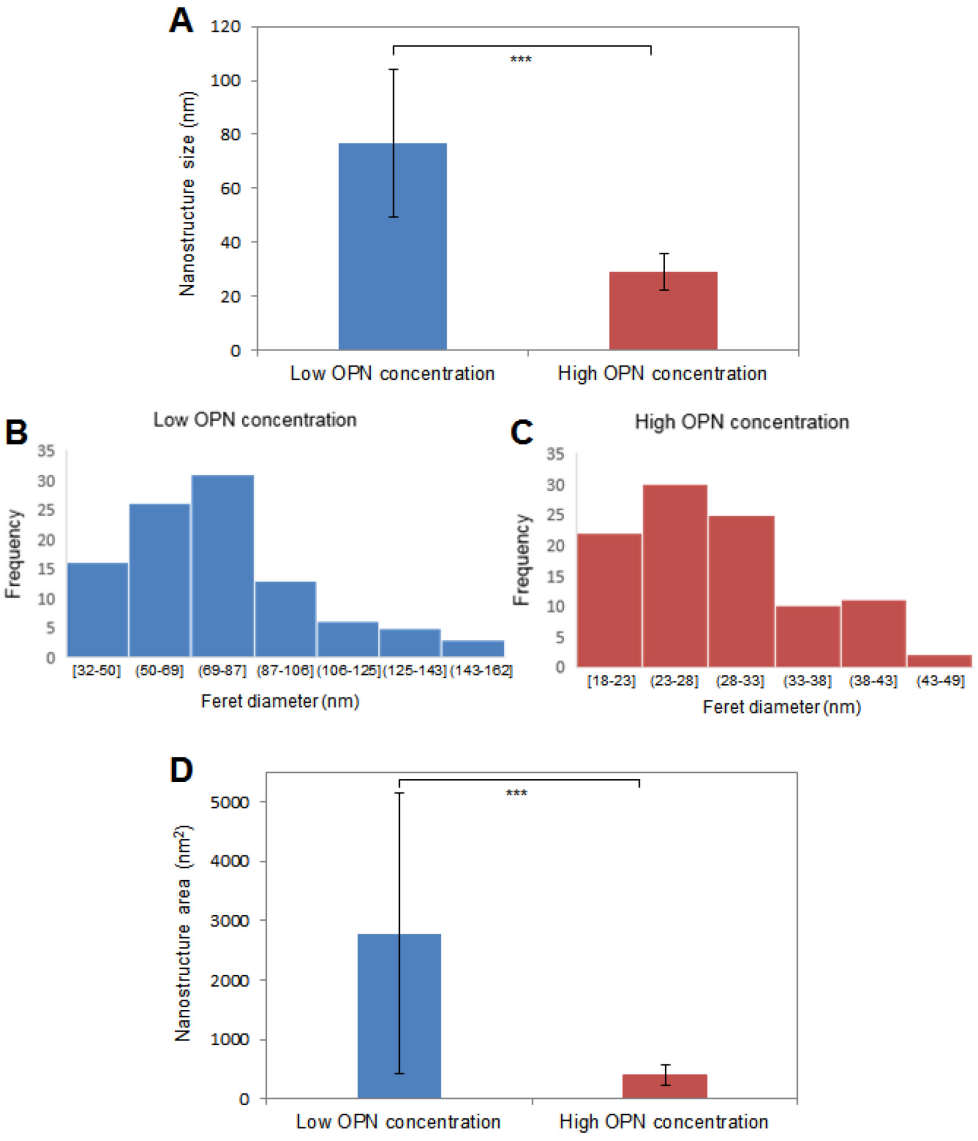

Fig. 2.S6 Effect of OPN on nanostructure size in synthetic calcite crystals. (**A**) Nanostructure size distribution between calcite crystals grown with 0.9 µM OPN or with 5.9 µM OPN. Significant difference indicated by bracket ***$P < 0.001$. (**B** and **C**) Distribution of nanostructure in synthetic calcite crystals grown in a low (0.9 µM, B) and high (5.9 µM, C) OPN concentration. (**D**) Nanostructure area distribution of synthetic calcite crystals grown in 0.9 µM OPN or in 5.9 µM OPN. Significant difference indicated by bracket ***$P < 0.001$. Values were compared by a two-paired Student's *t* test.

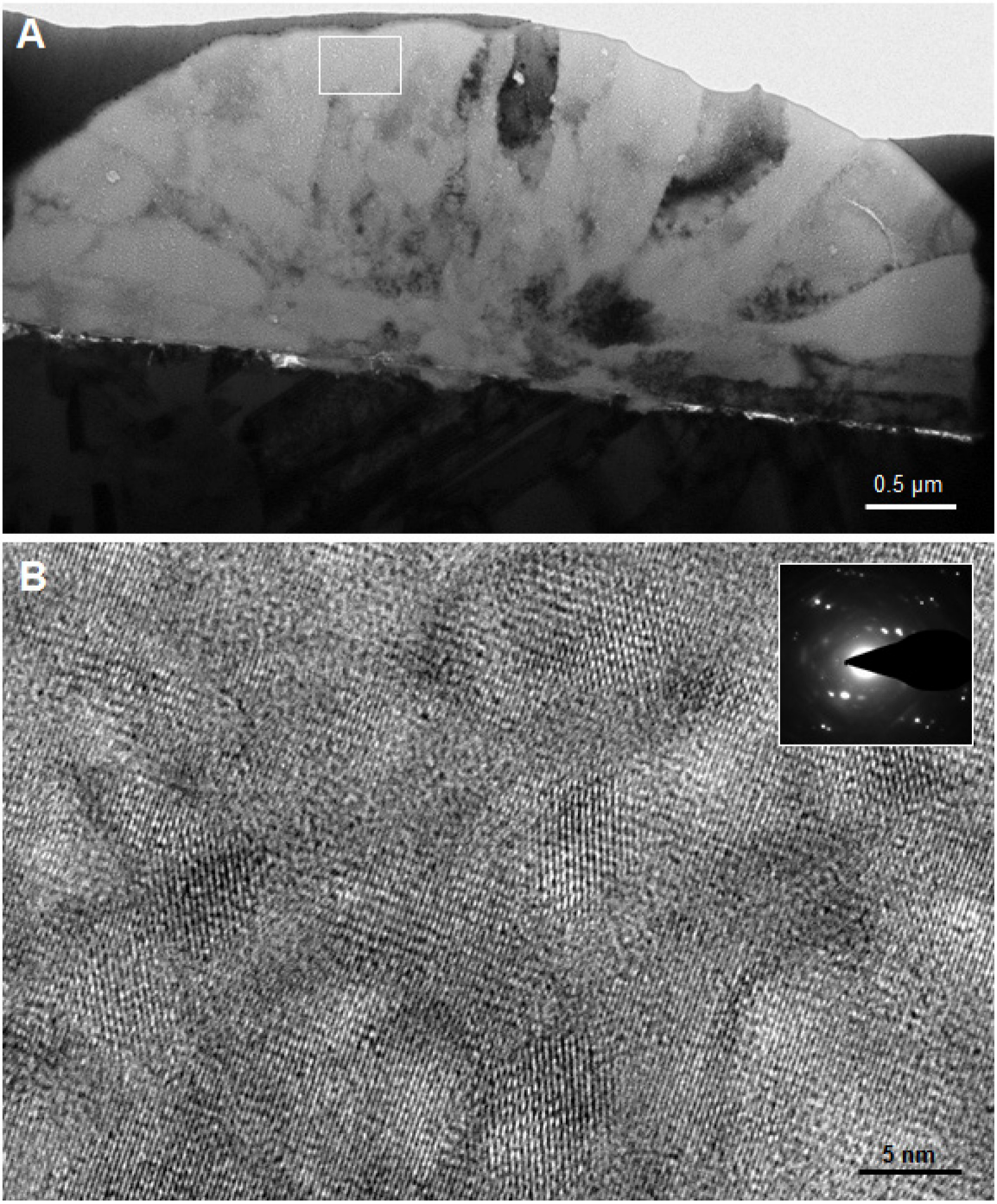

Fig. 2.S7 OPN induces nanostructure in synthetic calcite crystals. (**A**) Bright-field TEM image after FIB sectioning of a calcite crystal grown in the presence of 5.9 µM OPN. (**B**) HRTEM lattice imaging of the region boxed in A. Inset shows the selected-area electron diffraction pattern from this region.

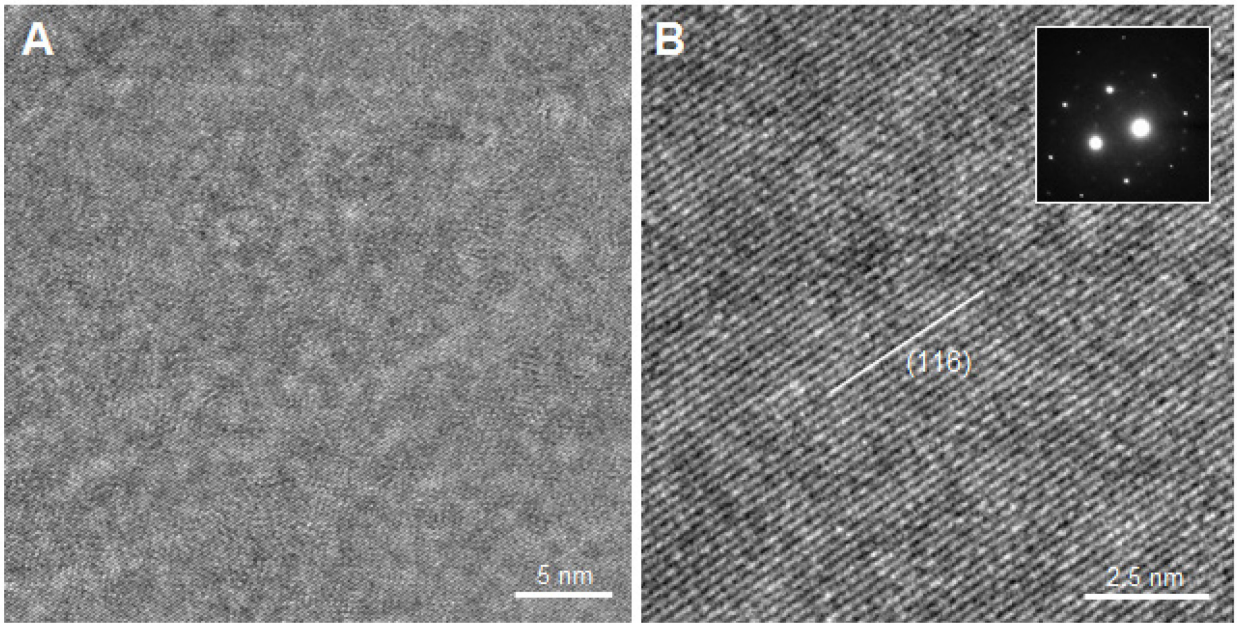

Fig. 2.S8 Absence of nanostructure in synthetic control calcite crystal (no added OPN). (**A**) Bright-field TEM image of calcite control sample after FIB sectioning showing no evidence of nanostructure. (**B**) HRTEM indexed lattice imaging of calcite control sample. Inset shows the selected-area electron diffraction pattern of the calcite showing a single crystal spot diffraction pattern.

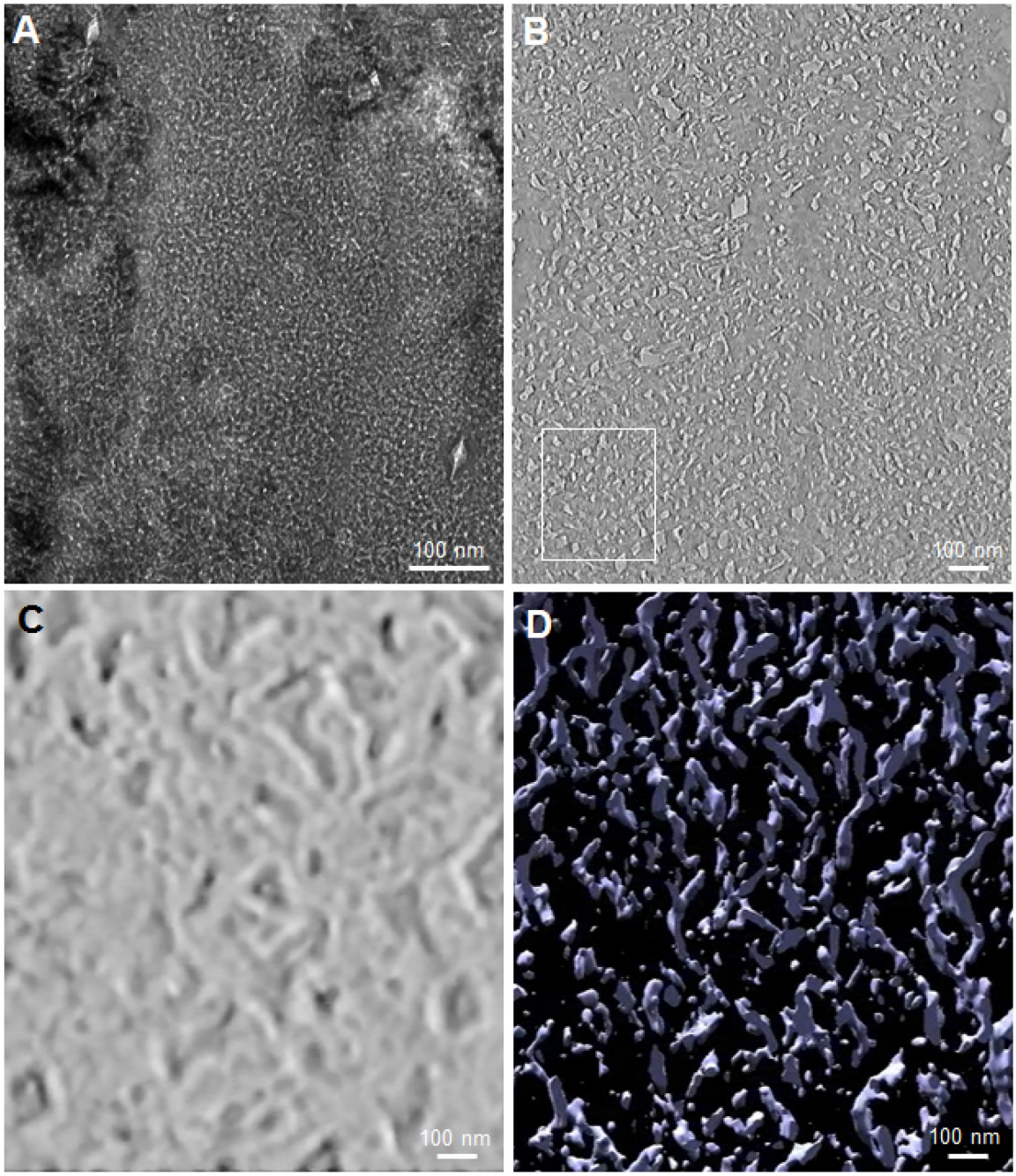

Fig. 2.S9 Electron microscopy of a FIB section showing nanostructure in a synthetic calcite crystal grown with OPN (5.9 µM). (**A**) Bright-field TEM image of a synthetic calcite crystal grown with OPN. (**B**) A single TEM image from the tomographic tilt series. (**C, D**) Three-dimensional tomographic reconstructions of the same nanostructured region indicated by the box in B (solid rendering in panel C, surface rendering in panel D). The surface rendering in panel D used a threshold that shows only high-density regions within the indicated box in panel B (see also movies 2.S3 and 2.S4).

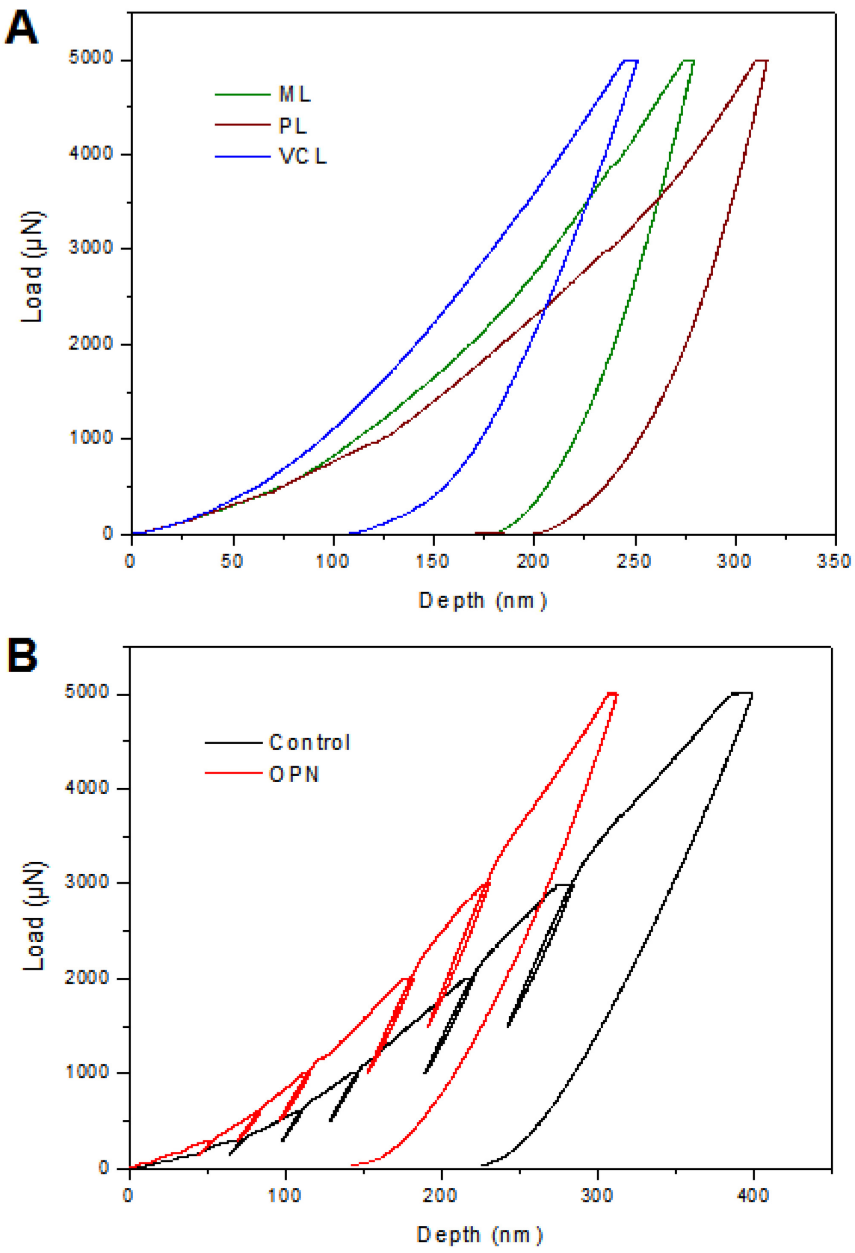

Fig. 2.S10 Nanoindentation displacement curves for eggshell and synthetic calcite crystals grown in OPN (5.9 μM). (**A**) Representative load-displacement curves from the VCL, PL (lower) and ML layers. (**B**) Partial unloading-displacement curves from synthetic calcite crystals grown with and without OPN.

Chicken eggshell and mouse otoconia are two nonskeletal mineralized calcareous biominerals in vertebrates. These two calcium-based mineralized structures have a fine-scale organization across multiple length scales which also share common patterns observed in the structural features of invertebrates such as seashells. Particularly, at the nanoscale, chicken eggshell and mouse otoconia structures consist of closely-packed nanogranules having a coherent orientation. Previous proteomic analysis has revealed abundant information about the protein composition from the chicken eggshell layers and mouse otoconia. In both systems, the observed nanostructure is attributed to the presence of an organic matrix, consisting mainly of proteins that are highly acidic (having substantial negative charge). However, it is remarkable that even though they share a nanostructure of the same mineral phase, these two biominerals form under different physiological conditions and perform entirely different functions. The next chapter of this dissertation examines in greater detail the fine structure of mouse otoconia.

Chapter 3 - Nanostructure of mammalian otoconia

Dimitra Athanasiadou[a], Wenge Jiang[a,1], Natalie Reznikov[a], Alejandro B. Rodríguez-Navarro[b], Valentin Nelea[a], Yongfeng Hu[c], and Marc D. McKee[a,d*]

[a]Faculty of Dentistry, McGill University, Montreal, QC, Canada H3A 0C7.

[b]Departamento de Mineralogía y Petrología, Universidad de Granada, Granada, Spain 18002.

[c]Canadian Light Source, University of Saskatchewan, Saskatoon, SK, Canada S7N 2V3.

[d]Department of Anatomy and Cell Biology, McGill University, Montreal, QC, Canada H3A 0C7.

[1]Present address: Department of Chemistry, Tianjin Key Laboratory of Molecular Optoelectronic Sciences, and Tianjin Collaborative Innovation Center of Chemical Science & Engineering, Tianjin University, Tianjin, P. R. China, 300072.

Manuscript in preparation

3.1 Abstract

Otoconia of the human inner ear are calcium carbonate (calcite)-containing mineralized structures involved in maintaining balance and in detecting linear acceleration. Otoconia contain abundant proteins including osteopontin (OPN), a highly phosphorylated mineral-binding protein present also in bones, teeth and chicken eggshells. Here we investigate, at the ultrastructural level, mineral structure and OPN localization in mouse otoconia. In microtome-cut/fractured otoconia obtained from normal (wild-type) C57BL/6 mice, scanning electron microscopy and atomic force microscopy revealed an internal nanostructure of approximately 50 nm in Feret diameter. Transmission electron microscopy and/or electron tomography of focused-ion beam-cut sections of otoconia confirmed this nanostructure with similar and smaller (approximately 10 nm) dimensions. By X-ray diffraction, only calcite was present; and Raman and X-ray absorption spectroscopies, which are chemically sensitive to both crystalline and amorphous forms in the sample, showed no evidence of amorphous calcium carbonate (in these samples from 8-day-old mice). Scanning and transmission electron microscopy combined with colloidal-gold immunolabeling for OPN revealed that this protein was located at the surface of the otoconia where its presence associated with surface nanostructure. In conclusion, these findings provide details on the composition and nanostructure of mammalian otoconia, and suggest that while OPN may influence surface rounding and surface nanostructure in otoconia, other incorporated proteins (also possibly including OPN) likely participate in creating internal nanostructure.

3.2 Introduction

Biomineralization processes have been broadly studied for many mineralized tissues (*5*). Otoconia (or otoliths in fish) are composites of calcium carbonate ($CaCO_3$) and proteins found in the utricle and the saccule of vertebrate mammals and lagena of non-mammalian vertebrates (*9, 147*). The vestibular system of the inner ear is responsible for head movement detection for spatial orientation and body balance (body equilibrium) (*147, 299*). In mammalian vertebrates, the vestibular system retains three fluid-filled semicircular canals, which respond to rotational acceleration and two receptor organs, the utricle and the saccule, which sense linear acceleration and gravity (*9, 164, 177*). Otoconia, surrounded by a low-calcium solution termed the endolymph, are embedded in a membranous structure, the otoconial membrane, and rest on the top of hair cell kinocilia and stereocilia in the utricular and saccular sensory epithelium also known as the macula (*9, 177*). With each head movement, the otoconia are displaced, leading to the sensory hair bundles bending (*177*). This mechanical impetus is transformed to electrical signals, transmitted by the hair cells to the central nervous system of the brain, which informs it of the exact head position in space (*177, 299*). Therefore, accurate knowledge of otoconia formation and structure is fundamental to the entire vestibular system and its function.

Otoconia occur as all the calcium-carbonate polymorphs depending upon the organism within which they reside (*155*). In mammals and birds, the polymorph for otoconia is calcite, the most thermodynamically calcium carbonate polymorph under ambient conditions (*300*). In amphibians and fish, the predominant polymorph is aragonite (*148, 155*). Vaterite is found in primitive jawfish or in pathologic conditions in human inner ear (*155, 158, 159*). Mammalian otoconia are barrel-like crystals having tri-planar facets at their ends (*177*), and they are the only biomineral in normal healthy mammals that is not carbonated hydroxyapatite (calcium phosphate),

the latter being the main mineral phase of bones and teeth. However, calcium-phosphate spherical otoconia occur in *Agnatha* species (jawless fish) where they have negligible or absent crystalline structure (*148*), or in malformed human inner ears sometimes mixed with calcite (*159*). Specific matrix proteins have been shown to promote the calcium-carbonate polymorph selection of otoconia (*163*).

As in other biominerals, and important for $CaCO_3$ crystallization in the inner ear, is the presence of an organic matrix consisting mainly of glycoproteins and proteoglycans (*9, 163, 177, 301, 302*). The presence of the otoconial proteins is necessary for the formation of otoconia since they can recruit and concentrate calcium ions from the low-calcium endolymph fluid (*177*). Proteins identified in mammalian otoconia are otoconin 90 (Oc90), otolin-1 (or otolin), osteopontin (OPN), fetuin-A, Sparc-like protein 1 (Sc1), secreted protein acidic and rich in cysteine (Sparc), dentin matrix protein 1 (DMP1) (*9, 173, 177*) and α-tectorin (*176*). Oc90, the main soluble matrix molecule, modulates the form of calcite crystals in vitro (*303*), whereas in the absence of this protein, no otoconia or few massive otoconia are formed and the calcite amounts are decreased roughly in half (*180, 304*). Otolin, also identified in bony fish (*305*), is a member of the collagen X family, localized in both otoconia and the surrounding otoconial matrix where it can serve as a scaffold protein for biomineralization (*181, 182*). Other proteins, such as fetuin-A, Sparc, OPN and DMP1, are considered as minor otoconins because of their negligible or no effect on otoconial formation and vestibular function (*168, 175, 176*). Other candidates for mediating otoconial mineralization are the keratan sulfate proteoglycans (KSPGs) (*176*), having strong negative charges for attracting calcium ions and appearing to interact with Oc90 and otolin proteins (*9*). OPN is a highly phosphorylated mineral-binding protein, having multiple roles in cell adhesion and protein binding in the extracellular matrix of bone and teeth (*200, 209, 244*). It is expressed in

the sensory hair cells, the nonsensory dark cells and the endolymph sac (*175*). As has been discussed previously, proteins could induce also a nanostructure in vivo or in vitro (*1, 38, 306*), despite their faceted morphology at microscale, suggesting perhaps a nonclassical crystallization pathway (*2, 3, 75*).

Otoconia are formed during the late embryonic stages and they are considered stable until mid-life where demineralization signs can be clearly observed in human otoconia (*307*). In mice, which share many otoconial features with humans, the seeding of otoconia is detected on embryonic day 14 with the highest rate of mineralization occurring at embryonic days 15 and 16 (*308*). Otoconia acquire their final size by postnatal day 7 and are generally preserved throughout life with minimum calcium transitions (*308, 309*). Studies on otoconia in humans are rare and mainly are associated with pathologic circumstances and developmental abnormalities (*158, 159*). In terms of their ultrastructure, human otoconia are composed of 3 sectors/branches at each end that extend outwards from the center, and a belly region, a site more susceptible to otoconial degeneration (*156*).

Morphological and compositional alterations of otoconia are frequently produced by head trauma, ototoxic drugs, aging, environmental and genetic factors lead to balance-related disorders (*9*). Benign paroxysmal positional vertigo (BPPV) is a serious disease in which the patients suffer from intense nausea (*193*). BPPV occurs when otoconia are dislodged from their initial position and migrate into the semicircular canals (canalithiasis), or when otoconia exist in larger numbers than the active surface area of the utricular cells (utriculithiasis) (*310*). Aging-related otoconial degeneration is a high-risk factor for creating free otoconial debris that results in loss of balance in elderly people, consequently leading to falls which may cause bone fracture or even death (*311*).

Women, particularly in their postmenopausal period, are more likely to be affected by BPPV than men (*198*).

To understand the formation of otoconia and possibly treat abnormalities, it is crucial to investigate the structure of otoconia at the nanoscale. In this study, at the molecular/atomic level, we describe the internal nanostructure of mouse otoconia using scanning and transmission electron microscopy/tomography as well as atomic force microscopy. We also describe the localization of OPN at the ultrastructural level in these otoconia using a high-resolution immunogold labeling approach. Finally, we examine in vitro the effects of OPN on calcite morphology.

3.3 Materials and methods

3.3.1 Harvesting and embedding of otoconia

Otoconia were dissected from C57BL/6 normal (wild-type) and *Opn*$^{-/-}$ knockout mice obtained from the Jackson Laboratory (Bar Harbor, ME, USA). All mice used were either 8 days old or 3 months old. Animals were kept in pathogen-free conditions with 12-hour light and 12-hour dark cycles at 24°C. Mice were fed normal mouse chow (2920X, Teklad global soy protein-free extruded rodent diet, Envigo, Huntingdon, UK), and had access to water *ad libitum*. The mice were sacrificed under isoflurane anesthesia followed by decapitation, and some mouse heads were fixed with aldehyde, dissected to isolate the inner ear, dehydrated and embedded in either Epon or LR White resin, while other heads were transferred unfixed immediately into 100% ethanol to prevent any otoconial dissolution. From the latter, otoconia were carefully retrieved under a stereoscope and kept in 100% ethanol. Embedded samples were sectioned for histology and mounted on either glass slides for atomic force microscopy or grids for scanning electron microscopy. Animal procedures were evaluated and approved by the McGill University

Institutional Animal Care and Use Committee following the Canadian Council on Animal Care guidelines.

3.3.2 Light microscopy of the vestibular inner ear system

For the inner ear vestibular system and otoconia observation, 1-µm sections from wild-type mouse otoconia were cut from polymerized blocks using a Leica Ultracut E ultramicrotome (Leica, Wetzlar, Germany). These sections were stained by von Kossa staining for mineral followed by toluidine blue staining and visualisation using a light microscope.

3.3.3 X-ray diffraction (XRD), Raman spectroscopy and X-ray absorption (XAS) of the otoconia mineral phase

The mineral phase of wild-type mice otoconia was analyzed by X-ray diffraction and Raman spectroscopy using a Bruker D8 Discover diffractometer equipped with a Cu X-ray tube (wavelength 0.154056 nm) and a Renishaw inVia Raman microscope (Renishaw, Gloucestershire, UK) equipped with a holographic spectrometer and a Leica DM2500 M optical microscope (Leica Microsystems GmbH, Wetzlar, Germany), respectively. For XRD analyses, measurements were run in coupled θ-θ scan in conventional powder diffraction mode (500 µm beam spot size). Samples of otoconia were placed in a small spot (ca. 1 mm diameter) using the sharp tip of a spatula. For Raman spectroscopy, the excitation source was a 514.5 nm Ar laser with a ca. 2 µm laser spot size and a 25mW excitation power. The laser was focused through a 50× objective (numerical aperture 0.75) on a dense array of otoconia. For each measurement, Raman spectra were acquired for 10 seconds were 3 scans were accumulated for minimizing any noise effects. Spectral reproducibility was confirmed by taking several spot analyses. XAS data collection was performed at the CLS at beamline 07ID-2. Otoconia sections of 1 µm thickness were placed on Si

wafers. The beam was run at energy of 2.8 GeV with a beam current of approximately 200 mA. A set of 5 scans was averaged from three samples to achieve the best signal-to noise ratio. All the spectra were obtained at the calcium K-edge and were normalized in reference to the positions of the intrinsic monochromator glitches and of the calcite edge spectrum.

3.3.4 Scanning electron microscopy (SEM)

To analyze the external and internal morphology of otoconia, isolated otoconia and resin-embedded and ultramicrotome-cut 1 µm-sections of otoconia were placed on conductive grids. Scanning electron microscopy using an Inspect F-50 FE-SEM (FEI Company) was performed at an accelerating voltage of 2 or 5 kV and the sections were not sputter-coated. Intact isolated otoconia were placed on aluminum SEM stubs, coated with a 2-nm thick Pt layer, and examined by SEM.

3.3.5 Atomic force microscopy (AFM)

To further investigate and interrogate the internal nanogranular structure of otoconia and the distribution of organic matrix, AFM was conducted on 1 µm diamond saw-cut sections from wild-type. AFM height and amplitude images were taken using a Nanoscope IIIa (Veeco, Santa Barbara, CA, USA) operating in the tapping mode in air at room temperature using a vertical engage E-scanner and NanoScope version 5.30 software (Veeco/Bruker-AXS Inc., Madison, WI, USA). In the AFM experiments, V-shaped tapping mode probes (typical tip apex radius of approximately 7 nm) with Si cantilevers having a spring constant k=42 N/m (Bruker-AXS Inc.) were used. The tip force exerted on the surface was optimized by the amplitude set-point being as high as possible to reduce imaging artefacts. The Feret diameters of the units comprising the nanostructure observed by AFM were calculated using ImageJ software. At least 200 Feret

diameters of the otoconial nanostructure were calculated from AFM images (obtained using amplitude mode) after performing high-pass processing to enhance boundaries.

3.3.6 Transmission electron microscopy (TEM) and focused-ion beam (FIB) sample preparation

The TEM investigation was performed on a thin FIB section of an otoconium. Bright-field TEM images and selected-area electron diffraction patterns (SAED) were obtained with a Tecnai TF-20 (FEI) microscope operating at 200 kV. A thin section of a single otoconium was prepared by a dual-beam focused-ion beam microscope (FEI Helios 600 NanoLab, FEI, Hillsboro, OR, USA) equipped with a gallium ion source. A nickel TEM grid with otoconia was placed on a flat aluminium SEM stub. A single otoconium was then covered with a protective 2-µm layer of Pt and a 2 µm slab cut from an otoconium was milled/thinned by the focused gallium ion beam. Afterwards, the thin section was transferred onto a Cu TEM half-grid using an EasyLift nanomanipulator for the final thinning. A final thin section of 80 nm was prepared at 5 kV and 9.4 nA.

3.3.7 Electron tomography

The FIB-cut section of an otoconium of approximately 80-nm-thick was collected on a copper grid. A Tecnai G2 F20 cryo-S/TEM (FEI) was used to collect a series of single-axis-tilt images at an accelerating voltage of 200 kV and equipped with a Gatan Ultrascan 4000 4k × 4k digital CCD camera system (model 895). Images were captured at a magnification of 62,000 over a tilt range of from –40° to +50° for the samples (2° increments in both low tilts and high tilts on the 80-nm-thick sections). The resulting images had pixel sizes of 0.19 nm. The images from the tilt series were aligned, filtered and reconstructed into a tomogram using the IMOD software

package (*266*). The movies for the raw tilt series and reconstruction were done using IMOD, whereas the movies with 3D volume with solid and surface rendering were generated using UCSF Chimera (version 1.10.1) software.

3.3.8 3D imaging and reconstruction

Three-dimensional imaging of utricular otoconia embedded in an LR White resin block was performed using a Zeiss Xradia 520 Versa (Carl Zeiss Canada Ltd). A series of X-ray frames (totalling 1989 projections) was collected over 360-degrees of rotation at 60 V with a pixel resolution of 0.5 µm. A reconstructed movie of the rotation series was generated using Dragonfly software (Object Research Systems Inc., Montreal).

3.3.9 2D X-ray diffraction

Otoconia crystal aggregates (3-month old) were analyzed with an X-ray single crystal diffractometer Bruker D8 VENTURE equipped with a photon area detector and a copper microsource. Three samples were analyzed in transmission mode. A series of frames were recorded while the sample was rotating in φ angle within the 3° to 10° angular range using steps of 0.3°.

3.3.10 Calcite crystal growth in the presence of OPN

Synthetic calcite crystals were grown into a 10 mM $CaCl_2$ solution with (or without) added full-length OPN (0.15, 0.3, 0.45 and 0.9 µM). Calcite crystallization took place for 2 hours on round glass coverslips in small wells placed within a well sealed desiccator previously charged with 1 g of $(NH_4)_2CO_3$ powder. Glass coverslips with calcite crystals were removed from solution, gently rinsed with distilled water and ethanol, and then, air-dried for further characterization. Triplicates were used for all the crystallization experiments. For the in vitro experiments, bovine

phosphorylated milk OPN was used (averaging 24 phosphorylations per molecule), as provided by Arla Foods and prepared according to the procedure described by Sørensen and Petersen (*265*).

3.3.11 Immunogold labeling of OPN

For immunogold OPN labeling, microtome-cut sections 80-nm-thick, as well as polymerized block faces containing both otoconia of wild-type and *Opn*-null mice (negative control), were used. All samples were incubated with anti-mouse OPN antibody (R&D systems) followed by protein A-colloidal gold complex (14-nm gold particles from G. Posthuma, University of Utrecht) to detect the immunolabeling reactions, then followed by conventional uranyl acetate and lead citrate staining. The cut sections were visualised by TEM as described above, and the block faces by SEM.

3.4 Results

3.4.1 Optical microscopy and scanning electron microscopy (SEM) – external morphology of otoconia

Fig. 3.1A shows by light microscopy an overview of a toluidine blue-stained utricle containing otoconia from wild-type mice. Otoconia (arrow), stained by the von Kossa method, rested upon a gelatinous mass, the otoconial membrane, overlying the hair cells of the utricular macula. The external morphology of wild-type mouse otoconia was observed by scanning electron microscopy (SEM) (Figs. 3.1B and C) while movie 3.S1 displays the 3D organization of otoconia in the utricle. The size of the majority of the otoconia generally ranged between 5 to 8 μm, with some smaller otoconia of approximately 2 μm in length (Fig. 3.1B). Higher magnification of the

otoconial surface reveals an external nanogranular structure on the barrel-shaped body, whereas the triplanar faceted surfaces appeared smoother (Fig. 3.1C).

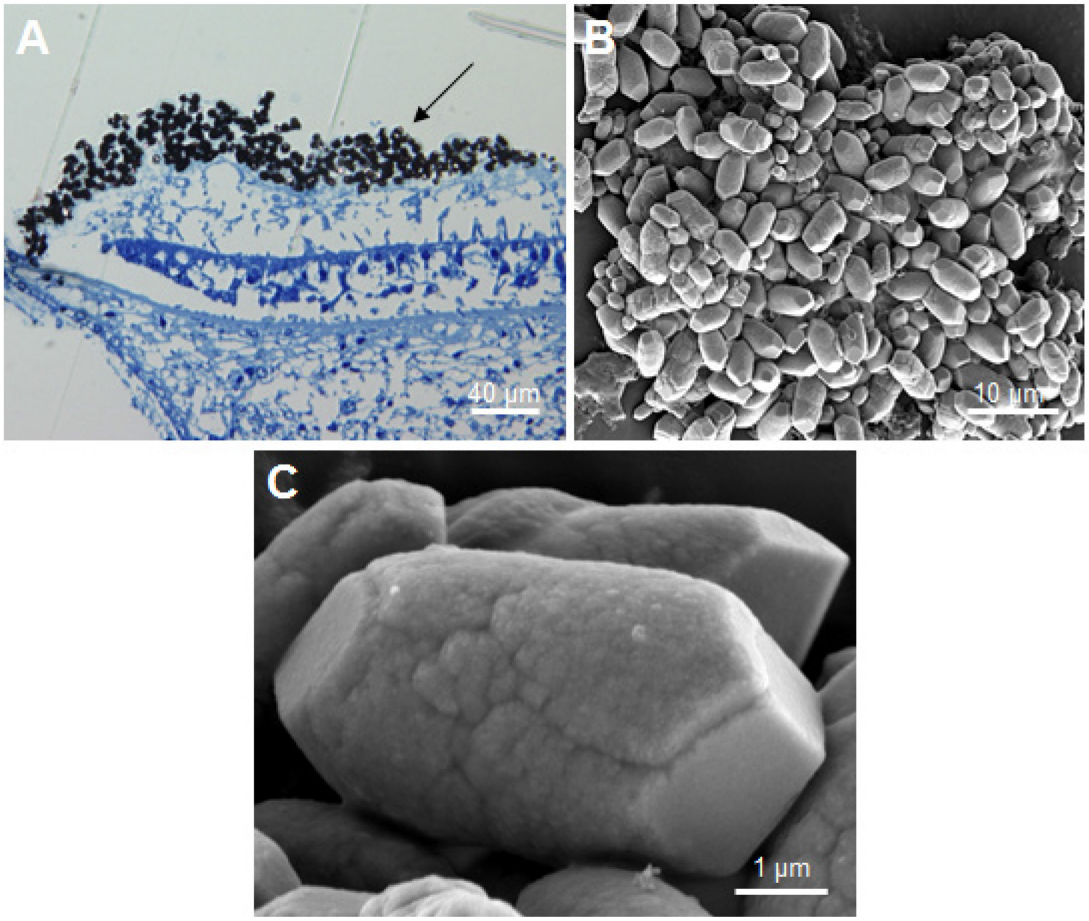

Fig. 3.1 External morphology of wild-type mouse otoconia. (**A**) Histological staining of a section of the mouse utricle observed by light microscopy after von Kossa staining for mineralized otoconia (black). (**B**) Low magnification SEM image of otoconia. (**C**) Higher magnification SEM image showing surface details of a single otoconium.

3.4.2 XRD, raman spectroscopy and X-ray absorption (XAS) – identification of $CaCO_3$ polymorphs and crystallinity of otoconia

As has been observed previously (*312*), mouse otoconia are crystallized in the form of calcite. XRD patterns from a cluster of many agglomerated otoconia revealed characteristic peaks corresponding to calcite (Fig. 3.2A). Similar to the XRD results, Raman spectra revealed characteristic peaks in the region between 100-1200 cm^{-1} attributable to vibrations arising from the calcite polymorph (Fig. 3.2B). Particularly, the bands 281 cm^{-1} and 155 cm^{-1} below 400 cm^{-1} are attributable to the vibrations of the complete unit cell, referred to as lattice modes. The bands of the region above 400 cm^{-1} are attributable to the internal modes of the carbonate ions, the symmetric stretching at 1085 cm^{-1} and the in-plane bending at 711 cm^{-1} (*30*). No evidence of amorphous calcium carbonate was observed from the 8-day-old mice otoconia. The pre-edge peak at 4035.8 eV, corresponding to the electronic transition 1s-3d and characteristic for ACC samples (*14*), was absent from the otoconia samples (Fig. 3.2C).

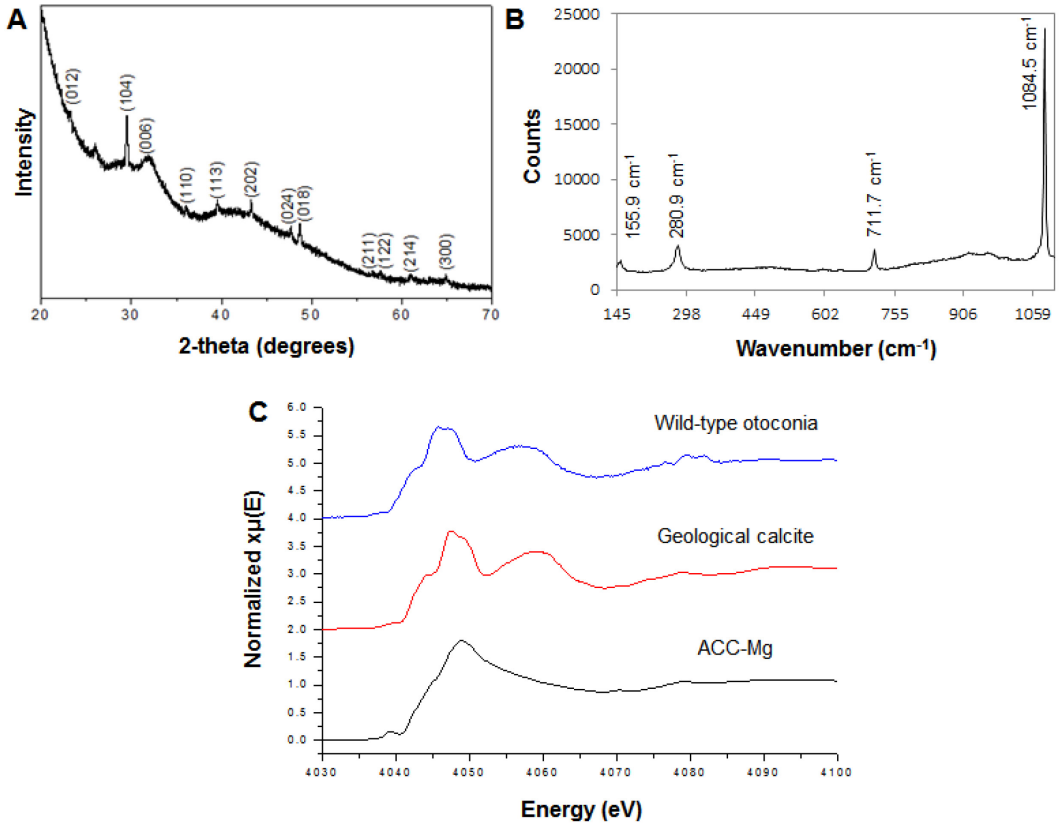

Fig. 3.2 Calcitic mouse otoconia. (**A**) XRD pattern showing calcite as the mineral phase in mouse otoconia with the predominant crystallographic-plane reflections labelled. (**B**) Micro-Raman spectrum obtained from a single otoconium. The Raman spectrum was compared with spectra obtained from a Raman database (Department of Geosciences, Johannes Gutenberg-Universität, Mainz) (*30*). (**C**) XAS spectra of wild-type mouse otoconia showing peaks characteristics for calcite. The spectrum was compared with XAS spectra of geological calcite and ACC-Mg obtained under the same experimental imaging conditions.

3.4.3 Internal structure of otoconia

Fig 3.3A shows an SEM image of an uncoated microtome-cut single otoconium revealing ubiquitous nanostructure throughout the otoconium. To further analyze this nanogranular structure cut-sections were also examined by atomic force microscopy (AFM). AFM height (Fig. 3.3B) and amplitude (Fig. 3.3C) images revealed an otoconial nanogranular structure consisted of about 50 ± 14 nm (SD) nanogranules in Feret diameter. Furthermore, phase-mode AFM images, as is shown

in Fig. 3.3D, disclosed areas of different composition at the boundaries of the nanogranules (arrows). Since there is no evidence of ACC, according to the XRD, Raman and XAS spectroscopy, at this mouse age (8-day old), these variations could be attributed to the presence of an organic content surrounding these nanogranules.

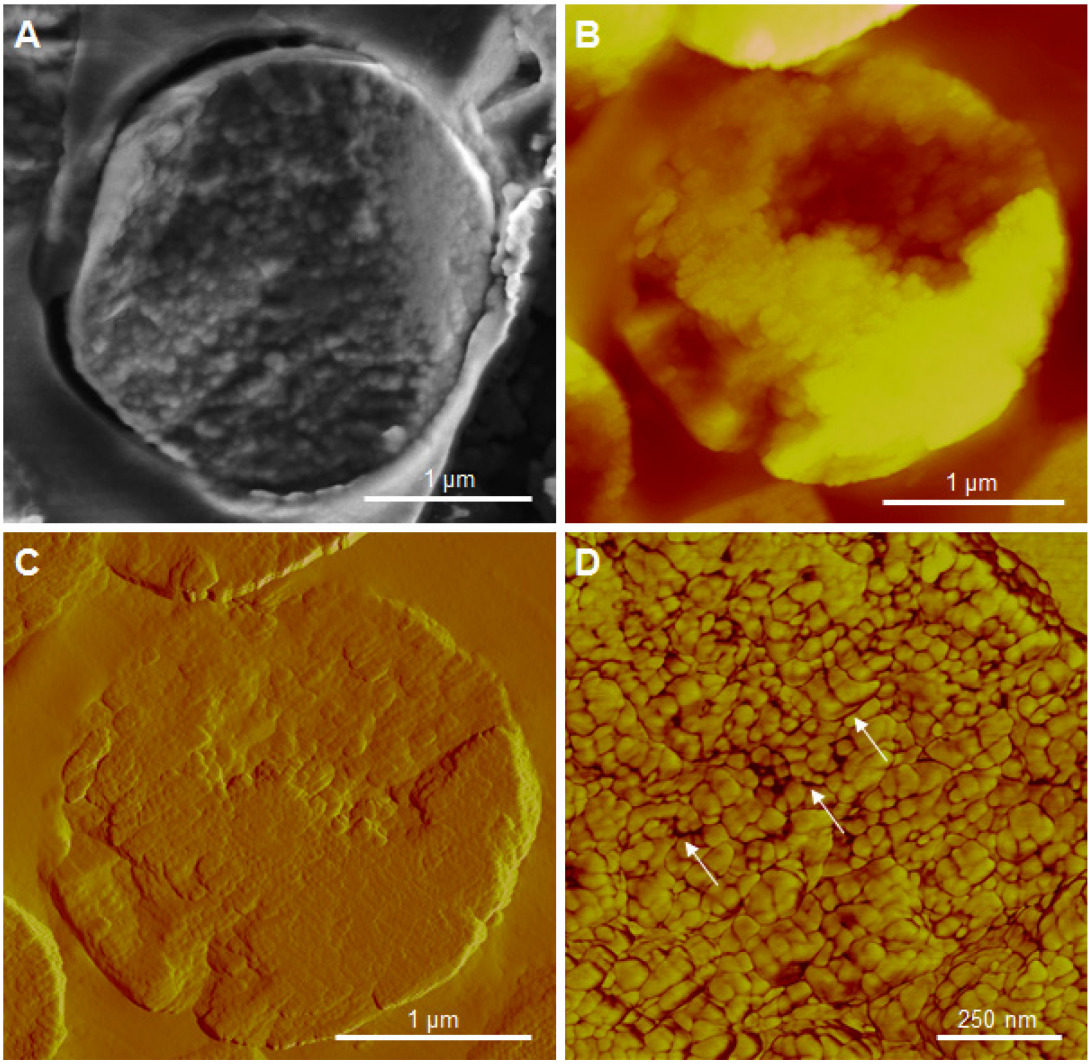

Fig. 3.3 Interior nanostructure of wild-type mouse otoconia. (**A**) SEM image from an uncoated otoconium. AFM image in (**B**) height and (**C**) amplitude mode showing internal otoconial nanostructure. (**D**) AFM phase mode image showing inorganic calcitic nanogranules (yellow) surrounded by organic material (red) (arrows).

An even smaller nanostructure size of approximately 10 nm in diameter was detected as seen by higher magnification lattice imaging in TEM (Fig. 3.4A). Selected-area electron diffraction (SAED) of these regions showed predominantly single crystal alignment (Fig. 3.4A, inset). Electron tomography showed 3D reconstructions of mouse otoconia (Fig. 3.4, B to D, and movies 3.S2 and 3.S3) where abundant and homogeneously dispersed 10-nm nanodomains were observed together with the larger nanostructure initially observed and measured by AFM (Fig. 3.3, B to D).

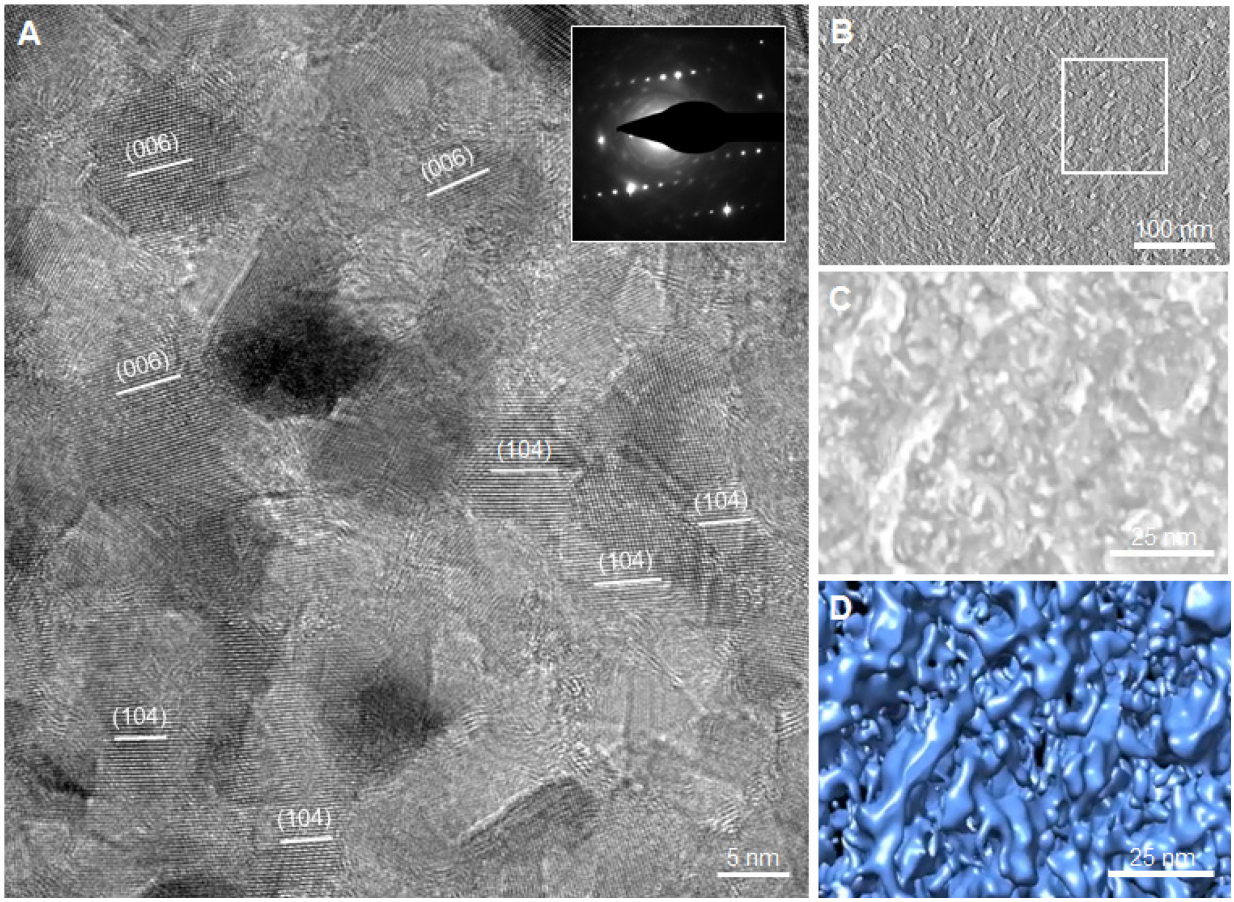

Fig. 3.4 Nanostructure of otoconia by TEM after FIB sectioning. (**A**) High-resolution TEM lattice imaging of nanodomains, with SAED indicating predominantly single crystal alignment. (**B**) Bright-field TEM image from a tilt series of a nanostructured branch region. (**C** and **D**) Three-dimensional tomographic reconstructions of the nanodomain branch region indicated by the box in (B) [solid and surface rendering in (C) and (D), respectively].

According to 2D XRD results, calcitic otoconia produced rings with rounded spots like those produced by gently ground geological calcite crystal (optical quality Iceland spar) which indicate that otoconia calcite crystals are randomly oriented and that individual crystals behave like high-quality calcite single crystals (Fig. 3.5, A and B). However, the otoconia calcite crystals have an internal granular nanostructure similar to that observed in other calcium carbonate biomineralization systems. Thus, the nanograins forming the otoconia calcite crystals must have a nearly perfect coherent orientation as it can be seen by SAED pattern (Fig. 3.4A, inset).

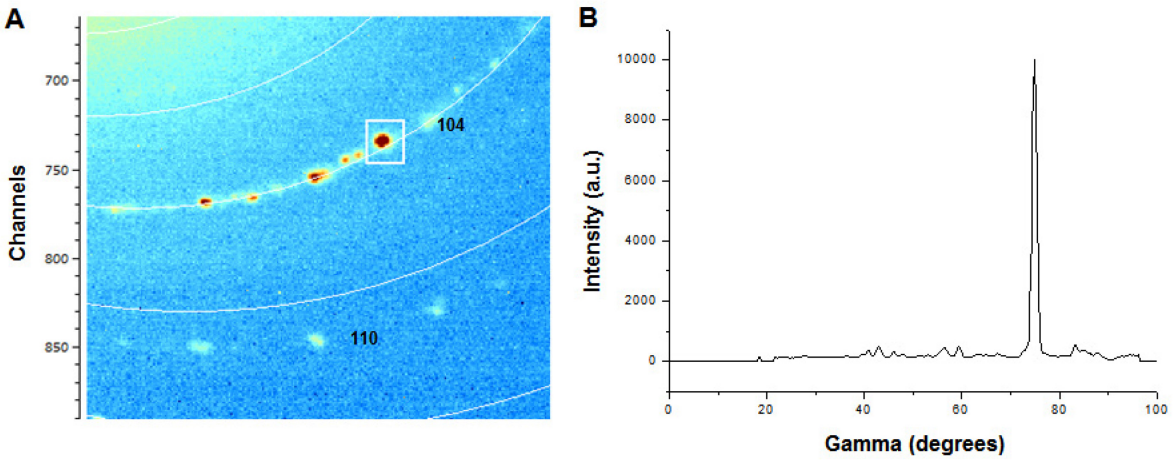

Fig. 3.5 2D XRD analysis of otoconia. (A) 2D X-ray diffraction pattern produced by otoconia showing single-crystal diffraction spots (box). **(B)** Intensity profile along the 104 calcite ring as a function of the γ angle.

3.4.4 Effect of OPN on calcite crystal growth in vitro

The effects of OPN on calcite crystal growth in vitro are shown in Fig. 3.6. At a low OPN concentration (0.15 μM), calcite crystals still retain their 104 rhombohedral morphology (Fig. 3.6A). After increasing the OPN concentration to 0.3 μM and 0.45 μM, morphological changes become more evident producing altered rounded growth step edges (Fig. 3.6, B and C,

respectively). At the highest OPN concentration (0.9 µM), calcite crystals start developing aggregates of 104 rhombohedra (Fig. 3.6D), all with rough surfaces.

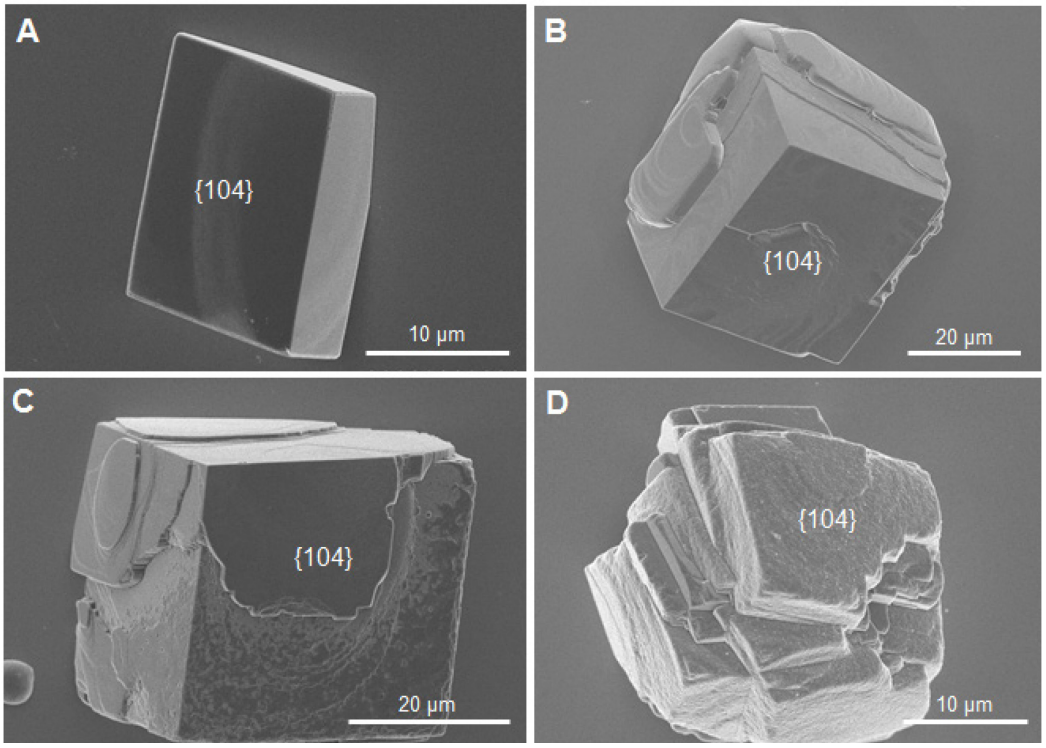

Fig. 3.6 Effect of full-length purified OPN protein on calcite growth in vitro. Increasing concentration of OPN (**A**) 0.15 µM, (**B**) 0.3 µM, (**C**) 0.45 µM and (**D**) 0.9 µM gradually alters the external morphology of synthetically grown calcite crystals.

3.4.5 Immunogold labeling for OPN in mouse otoconia

Colloidal-gold immunolabeling for OPN in otoconia was detected by TEM and SEM in wild-type and *Opn*$^{-/-}$ mice, the latter used as a negative control. The aqueous incubation steps required for OPN gold immunolabeling produced essentially a total decalcification of the otoconia resulting in voids in the prepared samples which precluded potential labeling of the otoconial interior but allowed OPN localization at the surface of the otoconia where OPN molecules are trapped locally by the infiltrated embedding resin and are not affected by the dissolution. OPN at

the surface of the otoconia was thus readily detected, with Figs. 3.7, A to D showing TEM and SEM immunogold labeling for OPN as indicated at the surface of the otoconia in wild-type mice. As expected, no labeling was observed in control mice lacking OPN (*Opn*$^{-/-}$) (Figs. 3.7, E to H).

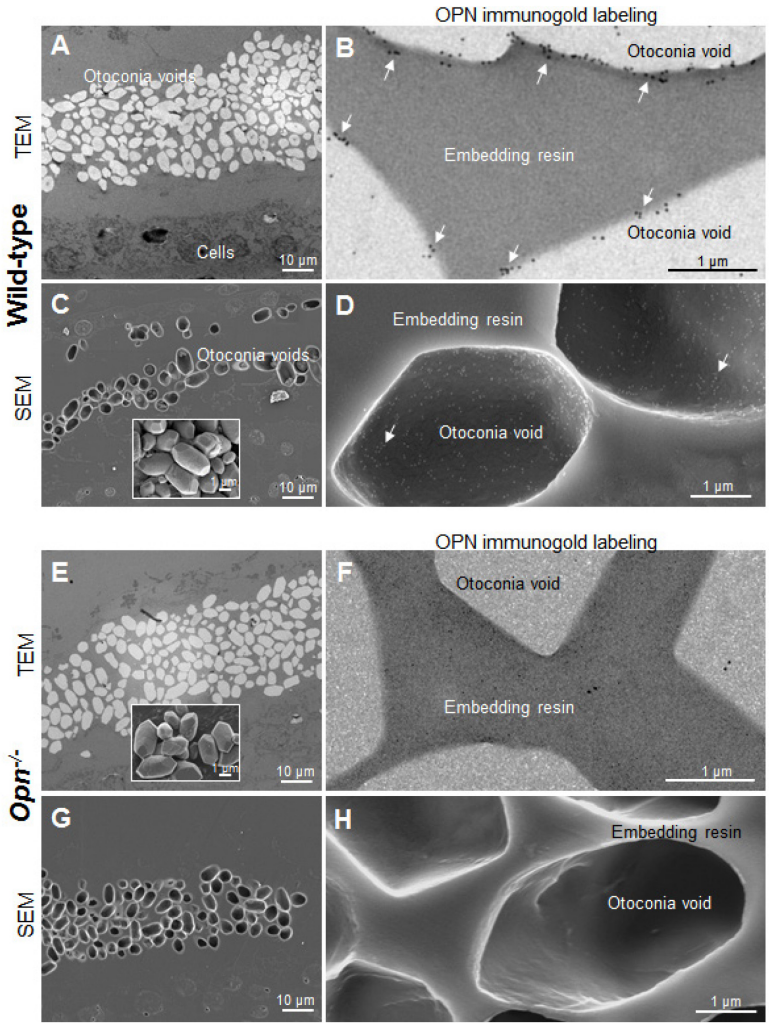

Fig. 3.7 Immunogold labeling of OPN in otoconia. (**A** and **C**) In wild-type mice, otoconial voids shown by TEM and SEM, respectively, after immunolabeling for OPN (aqueous procedures dissolve the calcitic otoconia). Inset: Intact wild-type mouse otoconia (without aqueous exposure) shown by SEM. By TEM (**B**) and SEM (**D**), immunogold labeling for OPN shows gold nanoparticles (arrows) at the surface of otoconial voids. (**E** and **G**) In OPN-deficient mice, otoconial voids shown by TEM and SEM, respectively, after immunolabeling for OPN. Inset: Intact otoconia from OPN-deficient mice (without aqueous exposure) shown by SEM. By TEM (**F**) and SEM (**H**), as expected in this negative control, immunogold labeling for OPN was absent.

3.5 Discussion

The structural relationship between the organic matrix and mineral constituents in otoconia is a topic of ongoing interest in the field of biomineralization. Even though the pervasiveness of human otoconia-related health problems has been recognized, little is known about the structural analysis of otoconia at the nanoscale. Nanostructured biominerals are now being found to be quite common in Nature, with their nanostructured morphology and properties being attributed to the presence of incorporated organic matrix (*2*). In the present study, using high-resolution, structure-determining techniques, we describe by AFM an internal nanostructure in mouse otoconia consisting of a packed nanostructure having approximately a grain size of 50 ± 14 nm (SD) with organic material surrounding the inorganic calcitic nanostructures. Inorganic phases and organic matrix of complex biominerals are distinguished using the phase function in the AFM tapping mode, which is very sensitive to sample inhomogeneous surfaces and compositional variations (*313*). This observation of packed nanogranules aligns with other descriptions of similar features in numerous calcareous biominerals such as the mature tablets of nacre (*35*) and the chicken and guinea fowl eggshells (*275, 306*). Commonly it seems, these nanogranules are surrounded by a composition, of either pure organic matrix or a combination of organics and ACC (*1*). Notably, most observations on mineralized tissues have revealed a nanostructure similar to what we report here for the first time in otoconia, characterized by roughly spheroidal nanogranules of a size ranging between 50 to 100 nm (*275, 306*). Such results align with there being the existence of a nonclassical crystallization pathway that escapes the classical crystallization pathway (*2, 3*), but further work under cryo-conditions is needed to confirm this. Previous model studies have indicated that organic additives, e.g. acidic biomacromolecules (*314*), could favorize a nonclassical aggregation-based crystal growth mechanism by stabilizing ACC particles (*2, 315*). Here, ACC

was not detected, but this could be attributed to the mature state (8-day-old) of the examined otoconia samples, where ACC could in fact be present at earlier stages of mouse otoconial development.

The smallest nanodomain size (~10 nm) observed by HRTEM could be related to regional variations in the organic content, likely proteins, acting as inhibitors/regulators of mineralization as has been proposed for calcitic chicken eggshell *G. gallus domesticus (306)*. Previously, it has been shown that Oc90, fetuin-A and OPN act as inhibitors of calcite crystal growth in vitro, primarily attributable to their high-binding affinity to calcium (*287*). These results are in agreement with our calcite crystal growth experiments here in which the presence of OPN modifies the typical rhombohedral shape of calcite in a concentration-dependent manner. With increasing OPN concentration, calcite {104} crystal faces have abundant growth islands and rounded step edges, disclosing changes in the growth mechanism of these crystal faces attributable to the added OPN. Even at higher OPN concentrations, the synthetic calcite crystals tend to create aggregates with rough surfaces of slightly mismatched {104} rhombohedra. This reflects surface activity, but previously we have shown the additional incorporation of a portion of the OPN into the crystal interior to generate inner nanostructure (*306*).

In previous in vitro experiments by others, it has been demonstrated that the addition of neither Oc90 nor otolin protein alone to growing calcite could produce the external shape of mature otoconia, but in combination of both proteins, they could to some degree (*182*). Similar to this, calcite-gelatin composites grown in gelatin gel matrices by a double diffusion method reveals similar morphological features to mammalian otoconia (branch and belly regions), but having a much larger size (*316*). Our TEM and tomography analysis on mouse otoconia revealed a crystalline calcitic structure in the branch region consisting of a dense nanostructure. Interestingly,

focused-ion beam-cut sections of these artificial composites demonstrated a dense crystalline branch region and a poorly crystalline belly region (*317*).

Occluded OPN into synthetic calcite crystals can induce a nanostructure similar to the nanostructure observed in calcitic chicken eggshell *G. gallus domesticus*, where higher OPN concentration creates smaller nanostructure and increased hardness *(306)*. Our findings of OPN at the surface of the otoconia by electron microscopy methods are consistent with previous studies using conventional immunohistochemistry and light microscopy (*4, 174*). However, because of the otoconia/calcite dissolution that occurs during the required aqueous immunolabeling incubation steps, we were not able to associate OPN with interior structure, and it thus remains possible that OPN is present within otoconia and contributes to the nanostructure. Indeed, otoconins such as Oc90 could likewise participate. OPN is co-expressed with Oc90 by the vestibular dark cells and in the endolymphatic sac (*4, 172, 318*), meaning that Oc90 could compensate for OPN during otoconial formation, and indeed Oc90 has a strong effect on otoconial formation. Oc90 knockout mice have rodlike large calcitic aggregates that are susceptible to dissolution (*168*). In contrast, *Opn*-null mice are characterized by normal balance behaviors and normal otoconial morphology (*175*).

Since OPN has now been localized to the periphery of otoconia in mice (our work) and rats (*174*), it could be involved in regulating their formation by controlling surface growth and nanostructure. The interplay between OPN and Oc90, and other ocotonial proteins, remains to be determined.

3.6 Conclusions

In summary, the internal structure of mouse otoconia at the nanoscale has been described. Within the interior of otoconia, using a combination of advanced imaging techniques, we show a densely packed calcite nanocrystals surrounded by organic material, with OPN being present at the very surface of the otoconia, suggesting involvement in the growth process and/or termination of otoconial growth via the mineralization-inhibiting activity of this protein. These findings provide detailed findings about the internal and external structure of otoconia, information that may lead to a better understanding of vertigo.

3.7 Acknowledgments

We are grateful to Ms. Lydia Malynowsky and Dr. Betty Hoac for otoconia dissections. We also thank Dr. Kelly Sears, Dr. David Liu, Ms. Weawkamol Leelapornpisit, Dr. Kaustuv Basu and Prof. Khanh Huy Bui for assistance with FIB, TEM and tomography work, and Dr. Natalie Reznikov and Dr. Rui Tahara for assistance with Xradia 520 versa imaging and Dragonfly software. We would like also to thank the Soft X-ray Microcharacterization Beamline (SXRMB) 06B1-1 at Canadian Light Source (CLS) for their technical support. This work was supported by Canadian Institutes of Health Research [MOP-142330, 2016] and the Natural Sciences and Engineering Research Council of Canada [RGPIN-2016-05031, 2016] to MDM. MDM is a member of the FRQ-S Network for Oral and Bone Health Research.

3.8 Supplementary materials

Movie 3.S1 Three-dimensional reconstruction of utricular otoconia (otoconia in grey and bone in orange) from an X-ray computed tomography series.

Movie 3.S2 Three-dimensional reconstruction from the branch region of 8-day-old mouse utricular otoconia from a TEM tomography tilt series.

Movie 3.S3 Three-dimensional reconstruction of a nanostructured region found in the branch region of 8-day-old mouse utricular otoconia from a TEM tomography tilt series.

Chapter 4 – Summary

4.1 General summary, discussion, future directions and final conclusions

Calcium carbonate is one of the most abundant biominerals in Nature. Chicken eggshell and otoconia are complex hierarchical structures of calcite, the most thermodynamically stable polymorph of calcium carbonate at ambient conditions. OPN is an acidic (Asp/D and Glu/E) calcium- and mineral-binding protein, phosphorylated (specifically P-Ser) and glycosylated by post-translational modifications, distributed in many tissue fluids and tissues, and particularly abundant in mineralized tissues such as bones and teeth, and also in chicken eggshell and mammalian otoconia. In recent years, there has been an extensive study of calcium carbonate biominerals at the nanometer length scale, with correlation to superior functional and mechanical properties. In mollusks, for example, nacre (aragonite) studied in *Pinna nobilis* shell is formed as the result of a nanoparticle assembly process where nanoparticles of 50-80 nm in size are packed gradually to form tablets in the mature nacre layer in association with an organic matrix (rich in acidic proteins and polysaccharides) (*35*). Nanostructure is also evident in the prismatic calcitic layer of *Pinna nobilis* as well as in *Pictada margaritifera* (the pearl oyster), where calcitic layer depositions exhibit similar nanogranules that are morphologically indistinguishable, an internal nanomorphology obvious among a broad spectrum of shells (*1*).

The aim of this dissertation was to investigate and provide novel findings on the detailed calcitic nanostructure of chicken eggshell and mouse otoconia, and on the possible role of OPN in creating this nanostructure, thus revealing new insights into calcium carbonate biomineralization processes.

Following the Chapter 1 literature review, in Chapter 2, the details of a nanostructure has been described for the first time in the various layers of the chicken eggshell. OPN was found to

be more abundant in the outermost eggshell layers correlating with the smallest nanostructure and with the highest hardness and elastic modulus. Moreover, in vitro, OPN was able to induce a similar nanostructure in synthetic calcite crystals. The nanostructure size that was observed was OPN concentration-dependent, with the smallest nanostructure observed in the calcite crystal growth experiments used a high amount of OPN. Previously in the eggshell, the only evidence of a nanostructure was provided at the initial chicken eggshell formation where disk-shaped ACC appears on the eggshell membranes (*99*). Our data is also the first to show that OPN, a prominent eggshell matrix protein, can induce calcitic nanostructure. In a previous study by Tseng et al. (*38*), a total extracted soluble nacreous acidic organic matrix – but not individual, characterized and purified organic constituents – resulted in nanostructured crystals. It remains entirely possible that also other eggshell acidic matrix proteins such as ovocleidin-17, ovocalyxin-32 and ovocalyxin-36 (*91, 97, 122, 259, 306*), besides OPN, can induce nanostructure, and additional future work is thus needed to determine whether they have similar actions.

In the same context, in Chapter 3, nanostructure was also investigated in mammalian otoconia (mice). Nanostructure of approximately 50 nm in Feret diameter (by AFM) and 10 nm (by TEM) was evident inside single otoconia. OPN was detected only at the surface of the otoconia even though an internal nanostructure is also present, but the possibility for internal OPN was not excluded based on methodological constraints. In either case, and given that mice lacking OPN have seemingly normal otoconia and vestibular apparatus function, it is likely that other incorporated otoconial acidic proteins exist to exert control over internal nanostructure. Future experiments could focus on individual proteins (otoconins) for identifying their specific role on nanostructure formation. A good example would be Oc90, which has previously been shown to

have substantial effects on the external morphology of otoconia (*168*), or possibly DMP1, although the latter's influence on otoconial structure remains still unclear.

The research results presented in this dissertation describe in detail the nanostructure of two calcareous biominerals – chicken eggshell (*G. gallus domesticus*) and mammalian otoconia. Previous studies have focused mainly on microscale structural analyses. By knowing the structure of these biominerals at the nanoscale, important advances could be achieved in the food industry for reducing eggshell breakage by cracking. Likewise, advances in the understanding of the causes for otoconial malformations and displacements within the semicircular canals that lead to vertigo might be realized. Finally, this information on nanostructure could be inspirational for the design of novel materials having enhanced mechanical and functional properties.

References

1. Y. Dauphin, J.- P. Cuif, J. E. Sorauf, *Biominerals and fossils through time* (Cambridge Univ. Press, 2010).
2. S. E. Wolf *et al.*, Nonclassical crystallization in vivo et in vitro (I): process-structure-property relationships of nanogranular biominerals. *J. Struct. Biol.* **196**, 244-259 (2016).
3. C. Rodríguez-Navarro, E. Ruiz-Agudo, J. Harris, S. E. Wolf, Nonclassical crystallization in vivo et in vitro (II): nanogranular features in biomimetic minerals disclose a general colloid-mediated crystal growth mechanism. *J. Struct. Biol.* **196**, 260-287 (2016).
4. M. Sakagami, Role of osteopontin in the rodent inner ear as revealed by in situ hybridization. *Med. Electron Microsc.* **33**, 3-10 (2000).
5. H.A. Lowenstam, S. Weiner, *On Biomineralization* (Oxford Univ. Press, 1989).
6. O. A. Jimoh, K. S. Ariffin, H. B. Hussin, A. E. Temitope, *Carbonate Evaporite* (Springer, 2018).
7. C. T. t. Hendley, J. Tao, J. A. Kunitake, J. J. De Yoreo, L. A. Estroff, Microscopy techniques for investigating the control of organic constituents on biomineralization. *MRS Bull.* **40**, 480-489 (2015).
8. L. Li *et al.*, A highly conspicuous mineralized composite photonic architecture in the translucent shell of the blue-rayed limpet. *Nat. Commun.* **6**, 6322 (2015).
9. Y. W. Lundberg, Y. F. Xu, K. D. Thiessen, K. L. Kramer, Mechanisms of otoconia and otolith development. *Dev. Dyn.* **244**, 239-253 (2015).
10. A. Sato *et al.*, Glycolytic intermediates induce amorphous calcium carbonate formation in crustaceans. *Nat. Chem. Biol.* **7**, 197-199 (2011).

11. J. Aizenberg, A. Tkachenko, S. Weiner, L. Addadi, G. Hendler, Calcitic microlenses as part of the photoreceptor system in brittlestars. *Nature* **412**, 819-822 (2001).

12. D. Faivre, D. Schuler, Magnetotactic bacteria and magnetosomes. *Chem. Rev.* **108**, 4875-4898 (2008).

13. K. Naka, *Biomineralization I: crystallization and self-organization process* (Springer 2007).

14. Y. Politi *et al.*, Structural characterization of the transient amorphous calcium carbonate precursor phase in sea urchin embryos. *Adv. Funct. Mater.* **16**, 1289-1298 (2006).

15. S. Raz, P. C. Hamilton, F. H. Wilt, S. Weiner, L. Addadi, The transient phase of amorphous calcium carbonate in sea urchin larval spicules: the involvement of proteins and magnesium ions in its formation and stabilization. *Adv. Funct. Mater.* **13**, 480-486 (2003).

16. L. Addadi, S. Raz, S. Weiner, Taking advantage of disorder: amorphous calcium carbonate and its roles in biomineralization. *Adv. Mater.* **15**, 959-970 (2003).

17. A. Berman, *Biomineralization: from nature to application* (Wiley, 2008).

18. R. A. Boulos *et al.*, Spinning up the polymorphs of calcium carbonate. *Sci. Rep.* **4**, 3616 (2014).

19. J. L. Wray, F. Daniels, Precipitation of calcite and aragonite. *J. Am. Chem. Soc.* **79**, 2031-2034 (1957).

20. T. Ogino, T. Suzuki, K. Sawada, The formation and transformation mechanism of calcium-carbonate in water. *Geochim. Cosmochim. Acta* **51**, 2757-2767 (1987).

21. S. Yoshioka, Y. Kitano, Transformation of aragonite to calcite through heating. *Geochem. J.* **19**, 245-249 (1985).

22. J. D. Rodríguez-Blanco, S. Shaw, L. G. Benning, The kinetics and mechanisms of amorphous calcium carbonate (ACC) crystallization to calcite, via vaterite. *Nanoscale* **3**, 265-271 (2011).

23. N. H. de Leeuw, S. C. Parker, Surface structure and morphology of calcium carbonate polymorphs calcite, aragonite, and vaterite: an atomistic approach. *J. Phys. Chem. B* **102**, 2914-2922 (1998).

24. B. Dickens, J. S. Bowen, Refinement of crystal structure of aragonite phase of $CaCO_3$. *J. Res. NBS A Phys. Chem.* **A 75**, 27-32 (1971).

25. L. Kabalah-Amitai *et al.*, Vaterite crystals contain two interspersed crystal structures. *Science* **340**, 454-457 (2013).

26. E. Mugnaioli *et al.*, Ab initio structure determination of vaterite by automated electron diffraction. *Angew. Chem. Int. Edit.* **51**, 7041-7045 (2012).

27. R. Demichelis, P. Raiteri, J. D. Gale, R. Dovesi, The multiple structures of vaterite. *Cryst. Growth Des.* **13**, 2247-2251 (2013).

28. D. L. Bryce, E. B. Bultz, D. Aebi, Calcium-43 chemical shift tensors as probes of calcium binding environments. Insight into the structure of the vaterite $CaCO_3$ polymorph by 43Ca solid-state NMR spectroscopy. *J. Am. Chem. Soc.* **130**, 9282-9292 (2008).

29. R. Lakshminarayanan, E. O. Chi-Jin, X. J. Loh, R. M. Kini, S. Valiyaveettil, Purification and characterization of a vaterite-inducing peptide, pelovaterin, from the eggshells of *Pelodiscus sinensis* (Chinese soft-shelled turtle). *Biomacromolecules* **6**, 1429-1437 (2005).

30. U. Wehrmeister *et al.*, Amorphous, nanocrystalline and crystalline calcium carbonates in biological materials. *J. Raman Spectrosc.* **42**, 926-935 (2011).

31. L. Qiao, Q. L. Feng, Z. Li, Special vaterite found in freshwater lackluster pearls. *Cryst. Growth Des.* **7**, 275-279 (2007).

32. M. P. Isaure *et al.*, Calcium promotes cadmium elimination as vaterite grains by tobacco trichomes. *Geochim. Cosmochim. Acta* **74**, 5817-5834 (2010).

33. H. A. Lowenstam, D. P. Abbott, Vaterite: a mineralization product of the hard tissues of a marine organism (Ascidiacea). *Science* **188**, 363-365 (1975).

34. G. Nehrke, H. Poigner, D. Wilhelms-Dick, T. Brey, D. Abele, Coexistence of three calcium carbonate polymorphs in the shell of the Antarctic clam *Laternula elliptica*. *Geochem. Geophys.* **13**, (2012).

35. R. Hovden *et al.*, Nanoscale assembly processes revealed in the nacroprismatic transition zone of Pinna nobilis mollusc shells. *Nat. Commun.* **6**, 1-7 (2015).

36. Y. Dauphin, J. P. Cuif, C. Salome, J. Susini, Speciation and distribution of sulfur in a mollusk shell as revealed by in situ maps using X-ray absorption near-edge structure (XANES) spectroscopy at the S K-edge. *Am. Mineral.* **90**, 1748-1758 (2005).

37. G. Falini, S. Albeck, S. Weiner, L. Addadi, Control of aragonite or calcite polymorphism by mollusk shell macromolecules. *Science* **271**, 67-69 (1996).

38. Y. H. Tseng, C. Chevallard, Y. Dauphin, P. Guenoun, $CaCO_3$ nanostructured crystals induced by nacreous organic extracts. *Cryst. Eng. Comm.* **16**, 561-569 (2014).

39. J. Aizenberg, S. Weiner, L. Addadi, Coexistence of amorphous and crystalline calcium carbonate in skeletal tissues. *Connect. Tissue Res.* **44**, 20-25 (2003).

40. J. Seto *et al.*, Structure-property relationships of a biological mesocrystal in the adult sea urchin spine. *Proc. Natl. Acad. Sci. USA* **109**, 7126-7126 (2012).

41. E. Zolotoyabko *et al.*, Differences between bond lengths in biogenic and geological calcite. *Cryst. Growth Des.* **10**, 1207-1214 (2010).

42. A. Berman *et al.*, Biological-control of crystal texture: a widespread strategy for adapting crystal properties to function. *Science* **259**, 776-779 (1993).

43. S. Weiner, L. Addadi, H. D. Wagner, Materials design in biology. *Mater. Sci. Eng. C* **11**, 1-8 (2000).

44. F. Natalio *et al.*, Flexible minerals: self-assembled calcite spicules with extreme bending strength. *Science* **339**, 1298-1302 (2013).

45. Y. Y. Kim *et al.*, An artificial biomineral formed by incorporation of copolymer micelles in calcite crystals. *Nat. Mater.* **10**, 890-896 (2011).

46. K. R. Cho *et al.*, Direct observation of mineral-organic composite formation reveals occlusion mechanism. *Nat. Commun.* **7**, 10187 (2016).

47. J. W. Pro, F. Barthelat, The fracture mechanics of biological and bioinspired materials. *MRS Bulletin* **44**, 46-52 (2019).

48. L. L. Hench, Bioceramics: from concept to clinic. *J. Am. Ceram. Soc.* **74**, 1487-1510 (1991).

49. F. L. Coe, A. Evan, E. Worcester, Kidney stone disease. *J. Clin. Invest.* **115**, 2598-2608 (2005).

50. K. M. Cobb, C. D. Charles, H. Cheng, R. L. Edwards, El Niño/Southern oscillation and tropical Pacific climate during the last millennium. *Nature* **424**, 271-276 (2003).

51. H. Elderfield, G. Ganssen, Past temperature and delta 18O of surface ocean waters inferred from foraminiferal Mg/Ca ratios. *Nature* **405**, 442-445 (2000).

52. Y. Dauphin, Structure and composition of the septal nacreous layer of Nautilus macromphalus L. (Mollusca, Cephalopoda). *Zoology* **109**, 85-95 (2006).

53. Y. Dauphin, The nanostructural unity of mollusc shells. *Mineral. Mag.* **72**, 243-246 (2008).

54. D. E. Jacob *et al.*, Nanostructure, composition and mechanisms of bivalve shell growth. *Geochim. Cosmochim. Acta* **72**, 5401-5415 (2008).

55. I. Sethmann, A. Putnis, O. Grassmann, P. Lobmann, Observation of nano-clustered calcite growth via a transient phase mediated by organic polyanions: a close match for biomineralization. *Am. Mineral.* **90**, 1213-1217 (2005).

56. J. Stolarski, P. Gorzelak, M. Mazur, Y. Marrocchi, A. Meibom, Nanostructural and geochemical features of the Jurassic isocrinid columnal ossicles. *Acta Palaeontol. Pol.* **54**, 69-75 (2009).

57. S. E. Wolf *et al.*, Merging models of biomineralisation with concepts of nonclassical crystallisation: is a liquid amorphous precursor involved in the formation of the prismatic layer of the mediterranean fan mussel *Pinna nobilis*? *Faraday Discuss.* **159**, 433-448 (2012).

58. H. J. Gao, B. H. Ji, I. L. Jager, E. Arzt, P. Fratzl, Materials become insensitive to flaws at nanoscale: lessons from nature. *Proc. Natl. Acad. Sci. USA* **100**, 5597-5600 (2003).

59. Y. Oaki, H. Imai, Nanoengineering in echinoderms: the emergence of morphology from nanobricks. *Small* **2**, 66-70 (2006).

60. K. Oaki, H. Imai, The hierarchical architecture of nacre and its mimetic material. *Angew. Chem. Int. Edit.* **44**, 6571-6575 (2005).

61. D. Vielzeuf *et al.*, Multilevel modular mesocrystalline organization in red coral. *Am. Mineral.* **95**, 242-248 (2010).

62. D. Vielzeuf, J. Garrabou, A. Baronnet, O. Grauby, C. Marschal, Nano to macroscale biomineral architecture of red coral (*Corallium rubrum*). *Am. Mineral.* **93**, 1799-1815 (2008).

63. A. G. Checa *et al.*, Crystallographic orientation inhomogeneity and crystal splitting in biogenic calcite. *J. R. Soc. Interface* **10** (2013).

64. T. Okumura, M. Suzuki, H. Nagasawa, T. Kogure, Microstructural variation of biogenic calcite with intracrystalline organic macromolecules. *Cryst. Growth Des.* **12**, 224-230 (2012).

65. V. C. Sundar, A. D. Yablon, J. L. Grazul, M. Ilan, J. Aizenberg, Fibre-optical features of a glass sponge. *Nature* **424**, 899-900 (2003).

66. J. C. Weaver *et al.*, Hierarchical assembly of the siliceous skeletal lattice of the hexactinellid sponge *Euplectella aspergillum*. *J. Struct. Biol.* **158**, 93-106 (2007).

67. J. C. Weaver *et al.*, Nanostructural features of demosponge biosilica. *J. Struct. Biol.* **144**, 271-281 (2003).

68. J. Stolarski, A. Meibom, R. Przenioslo, M. Mazur, A cretaceous scleractinian coral with a calcitic skeleton. *Science* **318**, 92-94 (2007).

69. A. Gal, S. Weiner, L. Addadi, A perspective on underlying crystal growth mechanisms in biomineralization: solution mediated growth versus nanosphere particle accretion. *Cryst. Eng. Comm.* **17**, 2606-2615 (2015).

70. K. Henriksen, J. R. Young, P. R. Bown, S. L. S. Stipp, Coccolith biomineralisation studied with atomic force microscopy. *Palaeontology* **47**, 725-743 (2004).

71. H. Cölfen, M. Antonietti, Mesocrystals: inorganic superstructures made by highly parallel crystallization and controlled alignment. *Angew. Chem. Int. Edit.* **44**, 5576-5591 (2005).

72. H. Cölfen, S. Mann, Higher-order organization by mesoscale self-assembly and transformation of hybrid nanostructures. *Angew. Chem. Int. Edit.* **42**, 2350-2365 (2003).

73. F. C. Meldrum, H. Cölfen, Controlling mineral morphologies and structures in biological and synthetic systems. *Chem. Rev.* **108**, 4332-4432 (2008).

74. I. C. Olson *et al.*, Crystal lattice tilting in prismatic calcite. *J. Struct. Biol.* **183**, 180-190 (2013).

75. J. J. De Yoreo *et al.*, Crystal growth. Crystallization by particle attachment in synthetic, biogenic, and geologic environments. *Science* **349**, aaa6760 (2015).

76. C. Rodríguez-Navarro, A. B. Cara, K. Elert, C. V. Putnis, E. Ruiz-Agudo, Direct nanoscale imaging reveals the growth of calcite crystals via amorphous nanoparticles. *Cryst. Growth Des.* **16**, 1850-1860 (2016).

77. L. B. Gower, Biomimetic model systems for investigating the amorphous precursor pathway and its role in biomineralization. *Chem. Rev.* **108**, 4551-4627 (2008).

78. D. Gebauer, A. Volkel, H. Cölfen, Stable prenucleation calcium carbonate clusters. *Science* **322**, 1819-1822 (2008).

79. Y. Politi *et al.*, Transformation mechanism of amorphous calcium carbonate into calcite in the sea urchin larval spicule. *Proc. Natl. Acad. Sci. USA* **105**, 17362-17366 (2008).

80. N. Vidavsky *et al.*, Initial stages of calcium uptake and mineral deposition in sea urchin embryos. *Proc. Natl. Acad. Sci. USA* **111**, 39-44 (2014).

81. J. Mahamid, A. Sharir, L. Addadi, S. Weiner, Amorphous calcium phosphate is a major component of the forming fin bones of zebrafish: indications for an amorphous precursor phase. *Proc. Natl. Acad. Sci. USA* **105**, 12748-12753 (2008).

82. J. Mahamid *et al.*, Bone mineralization proceeds through intracellular calcium phosphate loaded vesicles: a cryo-electron microscopy study. *J. Struct. Biol.* **174**, 527-535 (2011).

83. E. Beniash, R. A. Metzler, R. S. K. Lam, P. U. P. A. Gilbert, Transient amorphous calcium phosphate in forming enamel. *J. Struct. Biol.* **166**, 133-143 (2009).

84. D. Gur *et al.*, Guanine-based photonic crystals in fish scales form from an amorphous precursor. *Angew. Chem. Int. Edit.* **52**, 388-391 (2013).

85. J. R. Dorvee, A. Veis, Water in the formation of biogenic minerals: peeling away the hydration layers. *J. Struct. Biol.* **183**, 278-303 (2013).

86. E. Beniash, L. Addadi, S. Weiner, Cellular control over spicule formation in sea urchin embryos: a structural approach. *J. Struct. Biol.* **125**, 50-62 (1999).

87. J. M. Neff, Ultrastructural studies of periostracum formation in hard shelled clam *Mercenaria Mercenaria* (L). *Tissue Cell* **4**, 311-326 (1972).

88. Y. Isa, An electron-microscope study on the mineralization of the skeleton of the staghorn coral *Acropora hebes*. *Mar. Biol.* **93**, 91-101 (1986).

89. P. G. Robey, Vertebrate mineralized matrix proteins: structure and function. *Connect. Tissue Res.* **35**, 131-136 (1996).

90. Y. C. Chien, M. T. Hincke, H. Vali, M. D. McKee, Ultrastructural matrix-mineral relationships in avian eggshell, and effects of osteopontin on calcite growth in vitro. *J. Struct. Biol.* **163**, 84-99 (2008).

91. M. T. Hincke *et al.*, The eggshell: structure, composition and mineralization. *Front. Biosci.-Landmark* **17**, 1266-1280 (2012).

92. J. L. Arias, D. J. Fink, S. Q. Xiao, A. H. Heuer, A. I. Caplan, Biomineralization and eggshells: cell-mediated acellular compartments of mineralized extracellular-matrix. *Int. Rev. Cytol.* **145**, 217-250 (1993).

93. Y. Nys, M. T. Hincke, J. L. Arias, J. M. Garcia-Ruiz, S. E. Solomon, Avian eggshell mineralization. *Poult. Avian Biol. Rev.* **10**, 143-166 (1999).

94. M. T. Hincke *et al.*, Identification and localization of lysozyme as a component of eggshell membranes and eggshell matrix. *Matrix Biol.* **19**, 443-453 (2000).

95. M. Wong, M. J. Hendrix, K. von der Mark, C. Little, R. Stern, Collagen in the egg shell membranes of the hen. *Dev. Biol.* **104**, 28-36 (1984).

96. Y. Nys, J. Gautron, J. M. Garcia-Ruiz, M. T. Hincke, Avian eggshell mineralization: biochemical and functional characterization of matrix proteins. *Comptes. Rendus. Palevol.* **3**, 549-562 (2004).

97. M. Hincke, J. Gautron, Y. Nys, A. B. Rodríguez-Navarro, M. D. McKee, The eggshell: structure and protective function. *Woodhead Publ. Food Sci, Tech. Nutrit.* 151-182 (2011).

98. Y. Nys, J. Zawadzki, J. Gautron, A. D. Mills, Whitening of brown-shelled eggs: mineral-composition of uterine fluid and rate of protoporphyrin deposition. *Poult. Sci.* **70**, 1236-1245 (1991).

99. A. B. Rodríguez-Navarro, P. Marie, Y. Nys, M. T. Hincke, J. Gautron, Amorphous calcium carbonate controls avian eggshell mineralization: a new paradigm for understanding rapid eggshell calcification. *J. Struct. Biol.* **190**, 291-303 (2015).

100. J. W. Dieckert, M. C. Dieckert, C. R. Creger, Calcium reserve assembly: a basis structural unit of the calcium reserve system of the hen egg-shell. *Poult. Sci.* **68**, 1569-1584 (1989).

101. J. E. Dennis *et al.*, Microstructure of matrix and mineral components of eggshells from white leghorn chickens (*Gallus gallus*). *J. Morphol.* **228**, 287-306 (1996).

102. M. T. Hincke, Y. C. Chien, L. C. Gerstenfeld, M. D. McKee, Colloidal-gold immunocytochemical localization of osteopontin in avian eggshell gland and eggshell. *J. Histochem. Cytochem.* **56**, 467-476 (2008).

103. A. Rodríguez-Navarro, O. Kalin, Y. Nys, J. M. Garcia-Ruiz, Influence of the microstructure on the shell strength of eggs laid by hens of different ages. *Br. Poult. Sci.* **43**, 395-403 (2002).

104. L. Severa, J. Němeček, S. Nedomová, J. Buchar, Determination of micromechanical properties of a hen's eggshell by means of nanoindentation. *J. Food Eng.* **101**, 146-151 (2010).

105. A. L. Romanoff, A. J. Romanoff, *The avian egg* (Wiley, 1949).

106. M. M. Bain *et al.*, Enhancing the egg's natural defence against bacterial penetration by increasing cuticle deposition. *Anim. Genet.* **44**, 661-668 (2013).

107. M. M. Bain *et al.*, Cuticle deposition improves the biosecurity of eggs through the laying cycle and can be measured on hatching eggs without compromising embryonic development. *Poult. Sci.* 1-10 (2018).

108. J. Gautron, M. T. Hincke, Y. Nys, Precursor matrix proteins in the uterine fluid change with stages of eggshell formation in hens. *Connect. Tissue Res.* **36**, 195-210 (1997).

109. M. Cusack, A. C. Fraser, T. Stachel, Magnesium and phosphorus distribution in the avian eggshell. *Comp. Biochem. Phys. B* **134**, 63-69 (2003).

110. Y. P. Lin, P. C. Singer, Inhibition of calcite crystal growth by polyphosphates. *Water Res.* **39**, 4835-4843 (2005).

111. M. Rose-Martel, S. Smiley, M. T. Hincke, Novel identification of matrix proteins involved in calcitic biomineralization. *J. Proteomics* **116**, 81-96 (2015).

112. A. Hernandez-Hernandez *et al.*, Identification of some active proteins in the process of hen eggshell formation. *Cryst. Growth Des.* **8**, 4330-4339 (2008).

113. J. M. Dominguez-Vera, J. Gautron, J. M. Garcia-Ruiz, Y. Nys, The effect of avian uterine fluid on the growth behavior of calcite crystals. *Poult. Sci.* **79**, 901-907 (2000).

114. J. Gautron, M. Pain, S. Solomon, Y. Nys, Soluble matrix of hen's eggshell extracts changes in vitro the rate of calcium carbonate precipitation and crystal morphology. *Br. Poult. Sci.* **37**, 853-866 (1996).

115. A. Hernandez-Hernandez *et al.*, Influence of eggshell matrix proteins on the precipitation of calcium carbonate ($CaCO_3$). *J. Cryst. Growth* **310**, 1754-1759 (2008).

116. E. D. Harris, J. E. Blount, R. M. Leach, Localization of lysyl oxidase in hen oviduct: implications in eggshell membrane formation and composition. *Science* **208**, 55-56 (1980).

117. J. L. Arias, M. S. Fernandez, J. E. Dennis, A. I. Caplan, Collagens of the chicken eggshell membranes. *Connect. Tissue Res.* **26**, 37-45 (1991).

118. M. S. Fernandez, M. Araya, J. L. Arias, Eggshells are shaped by a precise spatio-temporal arrangement of sequentially deposited macromolecules. *Matrix Biol.* **16**, 13-20 (1997).

119. M. S. Fernandez, A. Moya, L. Lopez, J. L. Arias, Secretion pattern, ultrastructural localization and function of extracellular matrix molecules involved in eggshell formation. *Matrix Biol.* **19**, 793-803 (2001).

120. J. L. Arias, M. Cataldo, M. S. Fernandez, E. Kessi, Effect of beta-aminoproprionitrile on eggshell formation. *Br. Poult. Sci.* **38**, 349-354 (1997).

121. S. D. Chowdhury, R. H. Davis, Influence of dietary osteolathyrogens on the ultrastructure of shell and membranes of eggs from laying hens. *Br. Poult. Sci.* **36**, 575-583 (1995).

122. K. Mann, B. Macek, J. V. Olsen, Proteomic analysis of the acid-soluble organic matrix of the chicken calcified eggshell layer. *Proteomics* **6**, 3801-3810 (2006).

123. I. Miksik, A. Eckhardt, P. Sedlakova, K. Mikulikova, Proteins of insoluble matrix of avian (*Gallus Gallus*) eggshell. *Connect. Tissue Res.* **48**, 1-8 (2007).

124. J. Gautron *et al.*, Ovocalyxin-32, a novel chicken eggshell matrix protein. isolation, amino acid sequencing, cloning, and immunocytochemical localization. *J. Biol. Chem.* **276**, 39243-39252 (2001).

125. M. T. Hincke, J. Gautron, C. P. Tsang, M. D. McKee, Y. Nys, Molecular cloning and ultrastructural localization of the core protein of an eggshell matrix proteoglycan, ovocleidin-116. *J. Biol. Chem.* **274**, 32915-32923 (1999).

126. M. T. Hincke, C. P. W. Tsang, M. Courtney, V. Hill, R. Narbaitz, Purification and immunochemistry of a soluble matrix protein of the chicken eggshell (ovocleidin-17). *Calcif. Tissue Int.* **56**, 578-583 (1995).

127. J. Gautron *et al.*, Cloning of ovocalyxin-36, a novel chicken eggshell protein related to lipopolysaccharide-binding proteins, bactericidal permeability-increasing proteins, and plunc family proteins. *J. Biol. Chem.* **282**, 5273-5286 (2007).

128. K. Mann, F. Siedler, The amino acid sequence of ovocleidin 17, a major protein of the avian eggshell calcified layer. *Biochem. Mol. Biol. Int.* **47**, 997-1007 (1999).

129. J. P. Reyes-Grajeda, A. Moreno, A. Romero, Crystal structure of ovocleidin-17, a major protein of the calcified *Gallus gallus* eggshell - Implications in the calcite mineral growth pattern. *J. Biol. Chem.* **279**, 40876-40881 (2004).

130. R. Lakshminarayanan, J. S. Joseph, R. M. Kini, S. Valiyaveettil, Structure-function relationship of avian eggshell matrix proteins: a comparative study of two major eggshell matrix proteins, ansocalcin and OC-17. *Biomacromolecules* **6**, 741-751 (2005).

131. C. L. Freeman, J. H. Harding, D. Quigley, P. M. Rodger, Structural control of crystal nuclei by an eggshell protein. *Angew. Chem. Int. Edit.* **49**, 5135-5137 (2010).

132. K. Mann, M. T. Hincke, Y. Nys, Isolation of ovocleidin-116 from chicken eggshells, correction of its amino acid sequence and identification of disulfide bonds and glycosylated Asn. *Matrix Biol.* **21**, 383-387 (2002).

133. C. Bardet, C. Vincent, M. C. Lajarille, T. Jaffredo, J. Y. Sire, OC-116, the chicken ortholog of mammalian MEPE found in eggshell, is also expressed in bone cells. *J. Exp. Zool. Part B* **314b**, 653-662 (2010).

134. M. Horvat-Gordon, F. Yu, D. Burns, R. M. Leach, Ovocleidin (OC116) is present in avian skeletal tissues. *Poult. Sci.* **87**, 1618-1623 (2008).

135. M. T. Hincke *et al.*, Purification of ovocalyxin-32, a novel chicken eggshell matrix protein. *Connect. Tissue Res.* **44**, 16-19 (2003).

136. J. Gautron *et al.*, Cloning of ovocalyxin-36, a novel chicken eggshell protein related to lipopolysaccharide-binding proteins, bactericidal permeability-increasing proteins, and plunc family proteins. *J. Biol. Chem.* **282**, 5273-5286 (2007).

137. M. L. H. Rose, M. T. Hincke, Protein constituents of the eggshell: eggshell-specific matrix proteins. *Cell. Mol. Life Sci.* **66**, 2707-2719 (2009).

138. J. Gautron *et al.*, Ovotransferrin is a matrix protein of the hen eggshell membranes and basal calcified layer. *Connect. Tissue Res.* **42**, 255-267 (2001).

139. M. T. Hincke, Ovalbumin is a component of the chicken eggshell matrix. *Connect. Tissue Res.* **31**, 227-233 (1995).

140. C. Jimenez-Lopez, A. Rodríguez-Navarro, J. M. Dominguez-Vera, J. M. Garcia-Ruiz, Influence of lysozyme on the precipitation of calcium carbonate: a kinetic and morphologic study. *Geochim. Cosmochim. Acta* **67**, 1667-1676 (2003).

141. X. Q. Wang *et al.*, Lysozyme mediated calcium carbonate mineralization. *J. Colloid. Interf. Sci.* **332**, 96-103 (2009).

142. V. Pipich, M. Balz, S. E. Wolf, W. Tremel, D. Schwahn, Nucleation and growth of $CaCO_3$ mediated by the egg-white protein ovalbumin: a time-resolved in situ study using small-angle neutron scattering. *J. Am. Chem. Soc.* **130**, 6879-6892 (2008).

143. X. Q. Wang *et al.*, Role of ovalbumin in the stabilization of metastable vaterite in calcium carbonate biomineralization. *J. Phys. Chem. B* **113**, 8975-8982 (2009).

144. X. Q. Wang *et al.*, Influence of ovalbumin on $CaCO_3$ precipitation during in vitro biomineralization. *J. Phys. Chem. B* **114**, 5301-5308 (2010).

145. M. Pines, V. Knopov, A. Bar, Involvement of osteopontin in egg shell formation in the laying chicken. *Matrix Biol.* **14**, 765-771 (1995).

146. M. R. J. Navarro, Carretero A., *Morphological mouse phenotyping: anatomy, histology and imaging* (Acad. Press, 2017).

147. G. A. Hiatt, *Color atlas and text of histology* (Wolters Kluwer, 2014).

148. D. D. Carlström, Crystallographic study of vertebrate otoliths. *Biol. Bull.* **125**, 441-463 (1963).

149. R. Thalmann, E. Ignatova, B. Kachar, D. M. Ornitz, I. Thalmann, Development and maintenance of otoconia - Biochemical considerations. *Ann. N. Y. Acad. Sci.* **942**, 162-178 (2001).

150. B. Fritzsch, H. Straka, Evolution of vertebrate mechanosensory hair cells and inner ears: toward identifying stimuli that select mutation driven altered morphologies. *J. Comp. Physiol. A Neuroethol. Sens. Neural. Behav. Physiol.* **200**, 5-18 (2014).

151. A. J. Hudspeth, Making an effort to listen: mechanical amplification in the ear. *Neuron.* **59**, 530-545 (2008).

152. S. M. Jones, L. C. Erway, R. A. Bergstrom, J. C. Schimenti, T. A. Jones, Vestibular responses to linear acceleration are absent in otoconia-deficient C57BL/6JEi-het mice. *Hear. Res.* **135**, 56-60 (1999).

153. S. M. Jones, L. C. Erway, K. R. Johnson, H. P. Yu, T. A. Jones, Gravity receptor function in mice with graded otoconial deficiencies. *Hear. Res.* **191**, 34-40 (2004).

154. M. C. Simmler *et al.*, Targeted disruption of Otog results in deafness and severe imbalance. *Nat. Genet.* **24**, 139-143 (2000).

155. M. D. Ross, K. G. Pote, Some properties of otoconia. *Philos. T. Roy. Soc. B* **304**, 445-& (1984).

156. L. E. Walther *et al.*, The inner structure of human otoconia. *Otol. Neurotol.* **35**, 686-694 (2014).

157. M. D. Ross, D. R. Peacor, The nature and crystal growth of otoconia in the rat. *Ann. Otol. Rhinol. Laryngol.* **84**, 22-36 (1975).

158. C. G. Wright *et al.*, A calcareous concretion in the posterior semicircular duct of a human labyrinth. *Am. J. Otolaryng.* **3**, 196-201 (1982).

159. L. G. Johnsson, R. C. Rouse, C. G. Wright, P. J. Henry, J. E. Hawkins, Pathology of neuroepithelial suprastructures of the human inner-ear. *Am. J. Otolaryng.* **3**, 77-90 (1982).

160. D. V. Lychakov, Evolution of otolithic membrane. Structure of otolithic membrane in amphibians and reptilians. *J. Evol. Biochem. Phys.* **40**, 331-342 (2004).

161. F. Marmo, G. Balsamo, E. Franco, Calcite in the statoconia of amphibians: a detailed analysis in the frog *Rana esculenta*. *Cell Tissue Res.* **233**, 35-43 (1983).

162. K. G. Pote, M. D. Ross, Utricular otoconia of some amphibians have calcitic morphology. *Hear. Res.* **67**, 189-197 (1993).

163. K. G. Pote, M. D. Ross, Each otoconia polymorph has a protein unique to that polymorph. *Comp. Biochem. Phys. B* **98**, 287-295 (1991).

164. I. Hughes, I. Thalmann, R. Thalmann, D. M. Ornitz, Mixing model systems: using zebrafish and mouse inner ear mutants and other organ systems to unravel the mystery of otoconial development. *Brain Res.* **1091**, 58-74 (2006).

165. S. E. Campana, Chemistry and composition of fish otoliths: pathways, mechanisms and applications. *Mar. Ecol. Prog. Ser.* **188**, 263-297 (1999).

166. M. S. Salamat, M. D. Ross, D. R. Peacor, Otoconial formation in the fetal-rat. *Ann. Oto. Rhinol. Laryn.* **89**, 229-238 (1980).

167. M. R. Deans, J. M. Peterson, G. W. Wong, Mammalian otolin: a multimeric glycoprotein specific to the inner ear that interacts with otoconial matrix protein otoconin-90 and cerebellin-1. *Plos One* **5**, e12765 (2010).

168. X. Zhao, H. Yang, E. N. Yamoah, Y. W. Lundberg, Gene targeting reveals the role of Oc90 as the essential organizer of the otoconial organic matrix. *Dev. Biol.* **304**, 508-524 (2007).

169. E. Ferrary, P. Tran Ba Huy, N. Roinel, C. Bernard, C. Amiel, Calcium and the inner ear fluids. *Acta Otolaryngol. Suppl.* **460**, 13-17 (1988).

170. A. N. Salt, N. Inamura, R. Thalmann, A. Vora, Calcium gradients in inner ear endolymph. *Am. J. Otolaryngol.* **10**, 371-375 (1989).

171. Y. Wang *et al.*, Otoconin-90, the mammalian otoconial matrix protein, contains two domains of homology to secretory phospholipase A2. *Proc. Natl. Acad. Sci. USA* **95**, 15345-15350 (1998).

172. E. Verpy, M. Leibovici, C. Petit, Characterization of otoconin-95, the major protein of murine otoconia, provides insights into the formation of these inner ear biominerals. *Proc. Natl. Acad. Sci. USA* **96**, 529-534 (1999).

173. I. Thalmann, I. Hughes, B. D. Tong, D. M. Ornitz, R. Thalmann, Microscale analysis of proteins in inner ear tissues and fluids with emphasis on endolymphatic sac, otoconia, and organ of Corti. *Electrophoresis* **27**, 1598-1608 (2006).

174. T. Takemura *et al.*, Localization of osteopontin in the otoconial organs of adult rats. *Hear. Res.* **79**, 99-104 (1994).

175. X. Zhao, S. M. Jones, W. B. Thoreson, Y. W. Lundberg, Osteopontin is not critical for otoconia formation or balance function. *J. Assoc. Res. Otolaryngol.* **9**, 191-201 (2008).

176. Y. Xu *et al.*, Expression, functional, and structural analysis of proteins critical for otoconia development. *Dev. Dyn.* **239**, 2659-2673 (2010).

177. Y. W. Lundberg, *Proteins involved in otoconia formation and maintenance* (B. S. Gendeh, Ed., 2012).

178. W. Lu *et al.*, In vitro effects of recombinant otoconin 90 upon calcite crystal growth. Significance of tertiary structure. *Hear. Res.* **268**, 172-183 (2010).

179. S. M. Smith *et al.*, Temporally-independent functional modes of spontaneous brain activity. *Proc. Natl. Acad. Sci. USA* **109**, 3131-3136 (2012).

180. L. R. Andrade, U. Lins, M. Farina, B. Kachar, R. Thalmann, Immunogold TEM of otoconin 90 and otolin - relevance to mineralization of otoconia, and pathogenesis of benign positional vertigo. *Hear. Res.* **292**, 14-25 (2012).

181. H. Yang *et al.*, Matrix recruitment and calcium sequestration for spatial specific otoconia development. *Plos One* **6**, e20498 (2011).

182. K. T. Moreland *et al.*, In vitro calcite crystal morphology is modulated by otoconial proteins otolin-1 and otoconin-90. *Plos One* **9**, e95333 (2014).

183. S. A. Shapses *et al.*, Osteopontin facilitates bone resorption, decreasing bone mineral crystallinity and content during calcium deficiency. *Calcif. Tissue Int.* **73**, 86-92 (2003).

184. M. Cohen-Salmon, A. El-Amraoui, M. Leibovici, C. Petit, Otogelin: a glycoprotein specific to the acellular membranes of the inner ear. *Proc. Natl. Acad. Sci. USA* **94**, 14450-14455 (1997).

185. A. El-Amraoui, M. Cohen-Salmon, C. Petit, M. C. Simmler, Spatiotemporal expression of otogelin in the developing and adult mouse inner ear. *Hear. Res.* **158**, 151-159 (2001).

186. M. C. Simmler *et al.*, Twister mutant mice are defective for otogelin, a component specific to inner ear acellular membranes. *Mamm. Genome* **11**, 961-966 (2000).

187. P. K. Legan, A. Rau, J. N. Keen, G. P. Richardson, The mouse tectorins. Modular matrix proteins of the inner ear homologous to components of the sperm-egg adhesion system. *J. Biol. Chem.* **272**, 8791-8801 (1997).

188. P. K. Legan *et al.*, A targeted deletion in alpha-tectorin reveals that the tectorial membrane is required for the gain and timing of cochlear feedback. *Neuron.* **28**, 273-285 (2000).

189. I. J. Russell *et al.*, Sharpened cochlear tuning in a mouse with a genetically modified tectorial membrane. *Nat. Neurosci.* **10**, 215-223 (2007).

190. I. Zwaenepoel *et al.*, Otoancorin, an inner ear protein restricted to the interface between the apical surface of sensory epithelia and their overlying acellular gels, is defective in autosomal recessive deafness DFNB22. *Proc. Natl. Acad. Sci. USA* **99**, 6240-6245 (2002).

191. J. G. Oas, Benign paroxysmal positional vertigo: a clinician's perspective. *Ann. N. Y. Acad. Sci.* **942**, 201-209 (2001).

192. J. M. Epley, Human experience with canalith repositioning maneuvers. *Ann. N. Y. Acad. Sci.* **942**, 179-191 (2001).

193. F. Salvinelli *et al.*, Benign paroxysmal positional vertigo: diagnosis and treatment. *Clin. Ter.* **155**, 395-400 (2004).

194. K. Mizukoshi, Y. Watanabe, H. Shojaku, J. Okubo, I. Watanabe, Epidemiological studies on benign paroxysmal positional vertigo in Japan. *Acta Otolaryngol. Suppl.* **447**, 67-72 (1988).

195. P. M. Bourgeois, I. Dehaene, Benign paroxysmal positional vertigo (BPPV). Clinical features in 34 cases and review of literature. *Acta Neurol. Belg.* **88**, 65-74 (1988).

196. W. T. Kao, L. S. Parnes, R. A. Chole, Otoconia and otolithic membrane fragments within the posterior semicircular canal in benign paroxysmal positional vertigo. *Laryngoscope* **127**, 709-714 (2017).

197. T. Yamanaka *et al.*, Osteoporosis as a risk factor for the recurrence of benign paroxysmal positional vertigo. *Laryngoscope* **123**, 2813-2816 (2013).

198. D. Vibert, M. Kompis, R. Hausler, Benign paroxysmal positional vertigo in older women may be related to osteoporosis and osteopenia. *Ann. Oto. Rhinol. Laryn.* **112**, 885-889 (2003).

199. S. H. Jeong *et al.*, Osteopenia and osteoporosis in idiopathic benign positional vertigo. *Neurology* **72**, 1069-1076 (2009).

200. L. W. Fisher, D. A. Torchia, B. Fohr, M. F. Young, N. S. Fedarko, Flexible structures of SIBLING proteins, bone sialoprotein, and osteopontin. *Biochem. Bioph. Res. Commun.* **280**, 460-465 (2001).

201. M. D. McKee, A. Nanci, Osteopontin: an interfacial extracellular matrix protein in mineralized tissues. *Connect. Tissue Res.* **35**, 197-205 (1996).

202. M. D. McKee, A. Nanci, Osteopontin at mineralized tissue interfaces in bone, teeth, and osseointegrated implants: ultrastructural distribution and implications for mineralized tissue formation, turnover, and repair. *Microsc. Res. Techniq.* **33**, 141-164 (1996).

203. K. Kohri *et al.*, Structure and expression of the mRNA encoding urinary stone protein (osteopontin). *J. Biol. Chem.* **268**, 15180-15184 (1993).

204. C. M. Giachelli *et al.*, Osteopontin is elevated during neointima formation in rat arteries and is a novel component of human atherosclerotic plaques. *J. Clin. Invest.* **92**, 1686-1696 (1993).

205. L. F. Brown *et al.*, Expression and distribution of osteopontin in human tissues: widespread association with luminal epithelial surfaces. *Mol. Biol. Cell* **3**, 1169-1180 (1992).

206. D. R. Senger, C. A. Perruzzi, A. Papadopoulos, D. G. Tenen, Purification of a human-milk protein closely similar to tumor-secreted phosphoproteins and osteopontin. *Biochim. Biophys. Acta* **996**, 43-48 (1989).

207. J. R. Hoyer, L. Otvos, L. Urge, Osteopontin in urinary stone formation. *Ann. N. Y. Acad. Sci.* **760**, 257-265 (1995).

208. D. S. Bautista *et al.*, Quantification of osteopontin in human plasma with an ELISA: basal levels in pre- and postmenopausal women. *Clin. Biochem.* **29**, 231-239 (1996).

209. J. Sodek, B. Ganss, M. D. McKee, Osteopontin. *Crit. Rev. Oral Biol. Med.* **11**, 279-303 (2000).

210. D. T. Denhardt *et al.*, Osteopontin-induced modifications of cellular functions. *Ann. N. Y. Acad. Sci.* **760**, 127-142 (1995).

211. G. F. Weber, H. Cantor, The immunology of Eta-1/osteopontin. *Cytokine Growth Factor Rev.* **7**, 241-248 (1996).

212. D. T. Denhardt, A. F. Chambers, Overcoming obstacles to metastasis--defenses against host defenses: osteopontin (OPN) as a shield against attack by cytotoxic host cells. *J. Cell. Biochem.* **56**, 48-51 (1994).

213. T. Uede, Y. Katagiri, J. Iizuka, M. Murakami, Osteopontin, a coordinator of host defense system: a cytokine or an extracellular adhesive protein? *Microbiol. Immunol.* **41**, 641-648 (1997).

214. H. Yoshitake, S. R. Rittling, D. T. Denhardt, M. Noda, Osteopontin-deficient mice are resistant to ovariectomy-induced bone resorption. *Proc. Natl. Acad. Sci. USA* **96**, 8156-8160 (1999).

215. V. Ophascharoensuk *et al.*, Obstructive uropathy in the mouse: role of osteopontin in interstitial fibrosis and apoptosis. *Kidney Int.* **56**, 571-580 (1999).

216. S. R. Rittling *et al.*, Protective role of osteopontin in endodontic infection. *Immunology* **129**, 105-114 (2010).

217. H. C. Crawford, L. M. Matrisian, L. Liaw, Distinct roles of osteopontin in host defense activity and tumor survival during squamous cell carcinoma progression in vivo. *Cancer Res.* **58**, 5206-5215 (1998).

218. Y. Yokosaki, K. Tanaka, F. Higashikawa, K. Yamashita, A. Eboshida, Distinct structural requirements for binding of the integrins alphavbeta6, alphavbeta3, alphavbeta5, alpha5beta1 and alpha9beta1 to osteopontin. *Matrix Biol.* **24**, 418-427 (2005).

219. S. T. Barry, S. B. Ludbrook, E. Murrison, C. M. T. Horgan, A regulated interaction between alpha 5 beta 1 integrin and osteopontin. *Biochem. Biophys. Res. Commun.* **267**, 764-769 (2000).

220. S. Denda, L. F. Reichardt, U. Muller, Identification of osteopontin as a novel ligand for the integrin alpha 8 beta 1 and potential roles for this integrin-ligand interaction in kidney morphogenesis. *Mol. Biol. Cell* **9**, 1425-1435 (1998).

221. D. D. Hu, E. C. K. Lin, N. L. Kovach, J. R. Hoyer, J. W. Smith, A biochemical-characterization of the binding of osteopontin to integrins alpha(v)beta(1) and alpha(v)beta(5). *J. Biol. Chem.* **270**, 26232-26238 (1995).

222. L. Liaw *et al.*, The adhesive and migratory effects of osteopontin are mediated via distinct cell surface integrins. Role of alpha v beta 3 in smooth muscle cell migration to osteopontin in vitro. *J. Clin. Invest.* **95**, 713-724 (1995).

223. A. Miyauchi *et al.*, Recognition of osteopontin and related peptides by an alpha-v-beta-3 integrin stimulates immediate cell signals in osteoclasts. *J. Biol. Chem.* **266**, 20369-20374 (1991).

224. D. D. Hu, J. R. Hoyer, J. W. Smith, characterization of the interaction between integrins and recombinant human osteopontin. *Ann. N. Y. Acad. Sci.* **760**, 312-314 (1995).

225. Y. Yokosaki *et al.*, The integrin alpha(9)beta(1) binds to a novel recognition sequence (SVVYGLR) in the thrombin-cleaved amino-terminal fragment of osteopontin. *J. Biol. Chem.* **274**, 36328-36334 (1999).

226. L. L. Smith *et al.*, Osteopontin N-terminal domain contains a cryptic adhesive sequence recognized by alpha9beta1 integrin. *J. Biol. Chem.* **271**, 28485-28491 (1996).

227. K. J. Bayless, G. E. Davis, Identification of dual alpha(4)beta(1) integrin binding sites within a 38 amino acid domain in the N-terminal thrombin fragment of human osteopontin. *J. Biol. Chem.* **276**, 13483-13489 (2001).

228. R. Agnihotri *et al.*, Osteopontin, a novel substrate for matrix metalloproteinase-3 (stromelysin-1) and matrix metalloproteinase-7 (matrilysin). *J. Biol. Chem.* **276**, 28261-28267 (2001).

229. B. Christensen, L. Schack, E. Klaning, E. S. Sorensen, Osteopontin is cleaved at multiple sites close to its integrin-binding motifs in milk and is a novel substrate for plasmin and cathepsin D. *J. Biol. Chem.* **285**, 7929-7937 (2010).

230. D. R. Senger, C. A. Perruzzi, Cell migration promoted by a potent GRGDS-containing thrombin-cleavage fragment of osteopontin. *Biochim. Biophys. Acta* **1314**, 13-24 (1996).

231. N. Nishimichi *et al.*, Polymeric osteopontin employs integrin alpha9beta1 as a receptor and attracts neutrophils by presenting a de novo binding site. *J. Biol. Chem.* **284**, 14769-14776 (2009).

232. N. Nishimichi *et al.*, Osteopontin undergoes polymerization in vivo and gains chemotactic activity for neutrophils mediated by integrin alpha9beta1. *J. Biol. Chem.* **286**, 11170-11178 (2011).

233. L. Du *et al.*, cDNA cloning of the murine Pex gene implicated in X-linked hypophosphatemia and evidence for expression in bone. *Genomics* **36**, 22-28 (1996).

234. A. F. Ruchon *et al.*, Pex mRNA is localized in developing mouse osteoblasts and odontoblasts. *J. Histochem. Cytochem.* **46**, 459-468 (1998).

235. N. M. Barros *et al.*, Proteolytic processing of osteopontin by PHEX and accumulation of osteopontin fragments in Hyp mouse bone, the murine model of X-linked hypophosphatemia. *J. Bone Miner. Res.* **28**, 688-699 (2013).

236. G. F. Weber, S. Ashkar, H. Cantor, Interaction between CD44 and osteopontin as a potential basis for metastasis formation. *Proc. Assoc. Am. Physicians* **109**, 1-9 (1997).

237. Y. U. Katagiri *et al.*, CD44 variants but not CD44s cooperate with beta1-containing integrins to permit cells to bind to osteopontin independently of arginine-glycine-aspartic acid, thereby stimulating cell motility and chemotaxis. *Cancer Res.* **59**, 219-226 (1999).

238. L. T. Senbanjo, M. A. Chellaiah, CD44: a multifunctional cell surface adhesion receptor is a regulator of progression and metastasis of cancer cells. *Front. Cell Dev. Biol.* **5**, 1-6 (2017).

239. W. N. Addison, F. Azari, E. S. Sorensen, M. T. Kaartinen, M. D. McKee, Pyrophosphate inhibits mineralization of osteoblast cultures by binding to mineral, up-regulating osteopontin, and inhibiting alkaline phosphatase activity. *J. Biol. Chem.* **282**, 15872-15883 (2007).

240. A. L. Boskey *et al.*, Osteopontin-hydroxyapatite interactions in vitro: inhibition of hydroxyapatite formation and growth in a gelatin-gel. *Bone Miner.* **22**, 147-159 (1993).

241. J. R. de Bruyn *et al.*, Dynamic light scattering study of inhibition of nucleation and growth of hydroxyapatite crystals by osteopontin. *Plos One* **8**, e56764 (2013).

242. B. Christensen, M. S. Nielsen, K. F. Haselmann, T. E. Petersen, E. S. Sorensen, Post-translationally modified residues of native human osteopontin are located in clusters: identification of 36 phosphorylation and five O-glycosylation sites and their biological implications. *Biochem. J.* **390**, 285-292 (2005).

243. B. Christensen *et al.*, Cell type-specific post-translational modifications of mouse osteopontin are associated with different adhesive properties. *J. Biol. Chem.* **282**, 19463-19472 (2007).

244. E. S. Sorensen, P. Hojrup, T. E. Petersen, Posttranslational modifications of bovine osteopontin: identification of twenty-eight phosphorylation and three O-glycosylation sites. *Protein Sci.* **4**, 2040-2049 (1995).

245. E. Salih, S. Ashkar, L. C. Gerstenfeld, M. J. Glimcher, Identification of the phosphorylated sites of metabolically 32P-labeled osteopontin from cultured chicken osteoblasts. *J. Biol. Chem.* **272**, 13966-13973 (1997).

246. M. Hincke, M. St Maurice, Phosphorylation-dependent modulation of calcium carbonate precipitation by chicken eggshell matrix proteins. In: M. Goldberg, A. Boskey, C. Robinson, Eds. (Chemistry and Biology of Mineralized Tissues: Am. Acad. Orthop. Surg. Rosemont, IL, 1998), pp. 13-17.

247. L. D. Silverman *et al.*, Hydroxyapatite growth inhibition by osteopontin hexapeptide sequences. *Langmuir* **26**, 9899-9904 (2010).

248. P. S. Rowe *et al.*, MEPE, a new gene expressed in bone marrow and tumors causing osteomalacia. *Genomics* **67**, 54-68 (2000).

249. A. Oldberg, A. Franzen, D. Heinegard, Cloning and sequence-analysis of rat bone sialoprotein (osteopontin) cDNA reveals an Arg-Gly-Asp cell-binding sequence. *Proc. Natl. Acad. Sci. USA* **83**, 8819-8823 (1986).

250. W. N. Addison, D. L. Masica, J. J. Gray, M. D. McKee, Phosphorylation-dependent inhibition of mineralization by osteopontin ASARM peptides is regulated by PHEX cleavage. *J. Bone Miner. Res.* **25**, 695-705 (2010).

251. G. K. Hunter, C. L. Kyle, H. A. Goldberg, Modulation of crystal formation by bone phosphoproteins: structural specificity of the osteopontin-mediated inhibition of hydroxyapatite formation. *Biochem. J.* **300 (Pt 3)**, 723-728 (1994).

252. J. R. Hoyer, J. R. Asplin, L. Otvos, Phosphorylated osteopontin peptides suppress crystallization by inhibiting the growth of calcium oxalate crystals. *Kidney Int.* **60**, 77-82 (2001).

253. L. J. Wang *et al.*, Phosphorylation of osteopontin is required for inhibition of calcium oxalate crystallization. *J. Phys. Chem. B* **112**, 9151-9157 (2008).

254. G. K. Hunter *et al.*, Role of phosphate groups in inhibition of calcium oxalate crystal growth by osteopontin. *Cells Tissues Organs* **189**, 44-50 (2009).

255. J. O'Young *et al.*, Phosphorylation of osteopontin peptides mediates adsorption to and incorporation into calcium oxalate crystals. *Cells Tissues Organs* **189**, 51-55 (2009).

256. Y. C. Chien *et al.*, Modulation of calcium oxalate dihydrate growth by selective crystal-face binding of phosphorylated osteopontin and polyaspartate peptide showing occlusion by sectoral (compositional) zoning. *J. Biol. Chem.* **284**, 23491-23501 (2009).

257. A. Langdon, B. Grohe, The osteopontin-controlled switching of calcium oxalate monohydrate morphologies in artificial urine provides insights into the formation of papillary kidney stones. *Colloids Surf. B Biointerfaces* **146**, 296-306 (2016).

258. A. Langdon *et al.*, Kinetics of calcium oxalate crystal growth in the presence of osteopontin isoforms: an analysis by scanning confocal interference microcopy. *Calcif. Tissue Int.* **84**, 240-248 (2009).

259. K. Mann, J. V. Olsen, B. Macek, F. Gnad, M. Mann, Phosphoproteins of the chicken eggshell calcified layer. *Proteomics* **7**, 106-115 (2007).

260. L. Kalmar, D. Homola, G. Varga, P. Tompa, Structural disorder in proteins brings order to crystal growth in biomineralization. *Bone* **51**, 528-534 (2012).

261. G. K. Hunter, J. O'Young, B. Grohe, M. Karttunen, H. A. Goldberg, The flexible polyelectrolyte hypothesis of protein-biomineral interaction. *Langmuir* **26**, 18639-18646 (2010).

262. J. J. De Yoreo *et al.*, Crystallization by particle attachment in synthetic, biogenic, and geologic environments. *Science* **349**, 6760-6769 (2015).

263. G. Wu, K. C. Chan, L. L. Zhu, L. G. Sun, J. Lu, Dual-phase nanostructuring as a route to high-strength magnesium alloys. *Nature* **545**, 80-83 (2017).

264. Y. C. Chien, M. T. Hincke, M. D. McKee, Ultrastructure of avian eggshell during resorption following egg fertilization. *J. Struct. Biol.* **168**, 527-538 (2009).

265. E. S. Sorensen, T. E. Petersen, Purification and characterization of 3 proteins isolated from the proteose peptone fraction of bovine-milk. *J. Dairy Res.* **60**, 189-197 (1993).

266. J. R. Kremer, D. N. Mastronarde, J. R. McIntosh, Computer visualization of three-dimensional image data using IMOD. *Journal of Structural Biology* **116**, 71-76 (1996).

267. T. E. Buchheit, T. J. Vogler, Measurement of ceramic powders using instrumented indentation and correlation with their dynamic response. *Mech. Mater.* **42**, 599-614 (2010).

268. J. W. Leggoe, Determination of the elastic modulus of microscale ceramic particles via nanoindentation. *J. Mater. Res.* **19**, 2437-2447 (2004).

269. W. C. Oliver, G. M. Pharr, An improved technique for determining hardness and elastic-modulus using load and displacement sensing indentation experiments. *J. Mater. Res.* **7**, 1564-1583 (1992).

270. M. S. Pacella, C. E. da Koo, R. A. Thottungal, J. J. Gray, Using the RosettaSurface algorithm to predict protein structure at mineral surfaces. *Method. Enzymol.* **532**, 343-366 (2013).

271. R. A. Engh, R. Huber, Accurate bond and angle parameters for X-ray protein-structure refinement. *Acta Crystallogr. A* **47**, 392-400 (1991).

272. D. L. Graf, Crystallographic tables for the rhombohedral carbonates. *Am. Mineral.* **46**, 1283-1316 (1961).

273. M. J. O'Meara *et al.*, Combined covalent-electrostatic model of hydrogen bonding improves structure prediction with Rosetta. *J. Chem. Theory Comput.* **11**, 609-622 (2015).

274. P. Raiteri, J. D. Gale, D. Quigley, P. M. Rodger, Derivation of an accurate force-field for simulating the growth of calcium carbonate from aqueous solution: a new model for the calcite-water interface. *J. Phys. Chem. C* **114**, 5997-6010 (2010).

275. A. Perez-Huerta, Y. Dauphin, Comparison of the structure, crystallography and composition of eggshells of the guinea fowl and graylag goose. *Zoology (Jena)* **119**, 52-63 (2016).

276. P. Dalbeck, M. Cusack, Crystallography (electron backscatter diffraction) and chemistry (electron probe microanalysis) of the avian eggshell. *Cryst. Growth Des.* **6**, 2558-2562 (2006).

277. S. Weiner, L. Addadi, Crystallization pathways in biomineralization. *Annu. Rev. Mater. Res.* **41**, 21-40 (2011).

278. S. E. G. Wolf, L. B. Gower, "Challenges and perspectives of the polymer-induced liquid-precursor process: the pathway from liquid-condensed mineral precursors to mesocrystalline products" in new perspectives on mineral nucleation and growth. A. E. S. Van Driessche, M. Kellermeier, L. G. Benning, D. Gebauer, Eds. (Springer Intern.: Cham, Switzerland, 2017), pp. 43-75.

279. D. Lammie, M. M. Bain, T. J. Wess, Microfocus X-ray scattering investigations of eggshell nanotexture. *J. Synchrotron Radiat.* **12**, 721-726 (2005).

280. A. M. Turing, The chemical basis of morphogenesis. *Philos. T. Roy. Soc. B* **237**, 37-72 (1952).

281. A. D. Economou *et al.*, Periodic stripe formation by a Turing mechanism operating at growth zones in the mammalian palate. *Nat. Genet.* **44**, 348-351 (2012).

282. A. Verch, I. E. G. Morrison, R. van de Locht, R. Kroger, In situ electron microscopy studies of calcium carbonate precipitation from aqueous solution with and Without organic additives. *J. Struct. Biol.* **183**, 270-277 (2013).

283. T. Bansagi, V. K. Vanag, I. R. Epstein, Tomography of reaction-diffusion microemulsions reveals three-dimensional turing patterns. *Science* **331**, 1309-1312 (2011).

284. Y. C. Chien, M. T. Hincke, M. D. McKee, Avian eggshell structure and osteopontin. *Cells Tissues Organs* **189**, 38-43 (2009).

285. P. Marie *et al.*, Quantitative proteomics and bioinformatic analysis provide new insight into protein function during avian eggshell biomineralization. *J. Proteomics* **113**, 178-193 (2015).

286. A. W. Xu, M. Antonietti, S. H. Yu, H. Cölfen, Polymer-mediated mineralization and self-similar mesoscale-organized calcium carbonate with unusual superstructures. *Adv. Mater.* **20**, 1333-1338 (2008).

287. M. N. Hong *et al.*, Effect of otoconial proteins fetuin a, osteopontin, and otoconin 90 on the nucleation and growth of calcite. *Cryst. Growth Des.* **15**, 129-136 (2015).

288. K. M. Bromley *et al.*, Amelogenin processing by MMP-20 prevents protein occlusion inside calcite crystals. *Cryst. Growth Des.* **12**, 4897-4905 (2012).

289. J. Musil, D. Rostislav, *Novel nanocomposite coatings: Advances and industrial applications* (Pan Stanford, 2013).

290. A. M. H. Ahmed *et al.*, Changes in eggshell mechanical properties, crystallographic texture and in matrix proteins induced by moult in hens. *Br. Poult. Sci.* **46**, 268-279 (2005).

291. R. Menig, M. H. Meyers, M. A. Meyers, K. S. Vecchio, Quasi-static and dynamic mechanical response of *Strombus gigas* (conch) shells. *Mater. Sci. Eng. A,* **297**, 203-211 (2001).

292. P. Fratzl, R. Weinkamer, Nature's hierarchical materials. *Prog. Mater. Sci.* **52**, 1263-1334 (2007).

293. F. Nudelman, N. A. J. M. Sommerdijk, Biomineralization as an inspiration for materials chemistry. *Angew. Chem. Int. Edit.* **51**, 6582-6596 (2012).

294. S. N. Wang, X. Q. Zhu, Q. Y. Li, R. Z. Wang, X. X. Wang, Damage-tolerance strategies for nacre tablets. *J. Struct. Biol.* **194**, 199-204 (2016).

295. Y. Y. Kim *et al.*, Tuning hardness in calcite by incorporation of amino acids. *Nat. Mater.* **15**, 903-910 (2016).

296. A. B. Rodríguez-Navarro, A. Yebra, Y. Nys, C. Jimenez-Lopez, J. M. Garcia-Ruiz, Analysis of avian eggshell microstructure using X-ray area detectors. *Eur. J. Mineral.* **19**, 391-398 (2007).

297. R. K. Tang *et al.*, Dissolution at the nanoscale: Self-preservation of biominerals. *Angew. Chem. Int. Edit.* **43**, 2697-2701 (2004).

298. V. Nelea, Y. C. Chien, J. Paquette, M. D. McKee, Effects of full-length phosphorylated osteopontin and constituent acidic peptides and amino acids on calcite dissolution. *Cryst. Growth Des.* **14**, 979-987 (2014).

299. E. N. Marieb, Essentials of human anatomy and physiology. *Nurs. Stand.* **6**, 48 (1991).

300. U. Lins *et al.*, The otoconia of the guinea pig utricle: internal structure, surface exposure, and interactions with the filament matrix. *J. Struct. Biol.* **131**, 67-78 (2000).

301. C. D. Fermin, D. S. Martin, Y. T. Li, S. C. Li, The glycan keratan sulfate in inner ear crystals. *Cell. Mol. Biol. (Noisy-le-grand)* **41**, 577-591 (1995).

302. M. Tachibana, H. Morioka, Glucuronic acid-containing glycosaminoglycans occur in otoconia: cytochemical evidence by hyaluronidase-gold labeling. *Hear. Res.* **62**, 11-15 (1992).

303. W. F. Lu *et al.*, In vitro effects of recombinant otoconin 90 upon calcite crystal growth. Significance of tertiary structure. *Hear. Res.* **268**, 172-183 (2010).

304. Y. F. Xu *et al.*, Expression, functional, and structural analysis of proteins critical for otoconia development. *Dev. Dyn.* **239**, 2659-2673 (2010).

305. E. Murayama, P. Herbomel, A. Kawakami, H. Takeda, H. Nagasawa, Otolith matrix proteins OMP-1 and Otolin-1 are necessary for normal otolith growth and their correct anchoring onto the sensory maculae. *Mech. Dev.* **122**, 791-803 (2005).

306. D. Athanasiadou *et al.*, Nanostructure, osteopontin, and mechanical properties of calcitic avian eggshell. *Sci. Adv.* **4**, eaar3219 (2018).

307. M. Anniko, J. Ylikoski, R. Wroblewski, Microprobe analysis of human otoconia. *Acta Otolaryngol.* **97**, 283-289 (1984).

308. D. M. Ornitz, B. A. Bohne, I. Thalmann, G. W. Harding, R. Thalmann, Otoconial agenesis in tilted mutant mice. *Hear. Res.* **122**, 60-70 (1998).

309. M. G. House, V. Honrubia, Theoretical models for the mechanisms of benign paroxysmal positional vertigo. *Audiol. Neurootol.* **8**, 91-99 (2003).

310. J. G. Oas, Benign paroxysmal positional vertigo: a clinician's perspective. *Ann. N. Y. Acad. Sci.* **942**, 201-209 (2001).

311. Y. Agrawal, Disorders of balance and vestibular function in us adults: data from the national health and nutrition examination survey, 2001-2004. *Arch. Intern. Med.* **169**, 1419-1419 (2009).

312. K. G. Pote, M. D. Ross, Ultrastructural morphology and protein-content of the internal organic material of rat otoconia. *J. Ultrastruct. Mol. Struct. Res.* **95**, 61-70 (1986).

313. T. Mass, J. L. Drake, E. C. Peters, W. Jiang, P. G. Falkowski, Immunolocalization of skeletal matrix proteins in tissue and mineral of the coral *Stylophora pistillata*. *Proc. Natl. Acad. Sci. USA* **111**, 12728-12733 (2014).

314. F. Marin et al., 'Shellome': proteins involved in mollusc shell biomineralization-diversity, functions. *Rec. Adv. Pearl Res.* (2013).

315. H. Cölfen, M. Antonietti, *Mesocrystals and nonclassical crystallization* (Wiley, 2008).

316. Y. X. Huang *et al.*, Shape development and structure of a complex (otoconia-like?) calcite-gelatine composite. *Angew. Chem. Int. Ed. Engl.* **47**, 8280-8284 (2008).

317. P. Simon *et al.*, Structural relationship between calcite-gelatine composites and biogenic (human) otoconia. *Eur. J. Inorg. Chem.* **2011**, 5370-5377 (2011).

318. E. G. Ignatova, I. Thalmann, B. Xu, D. M. Ornitz, R. Thalmann, Molecular mechanisms underlying ectopic otoconia-like particles in the endolymphatic sac of embryonic mice. *Hear. Res.* **194**, 65-72 (2004).